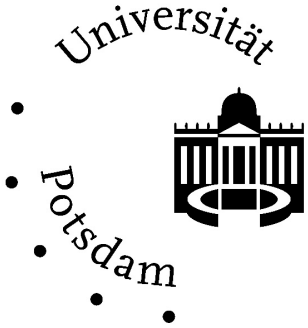

Evolutionary scatter of magnetic activity in cool star twins

Evolutionäre Streuung der magnetischen Aktivität in kühlen Sternzwillingen

Master thesis | Masterarbeit

Desmond Dsouza

26.October 2023

Evolutionary scatter of magnetic activity in cool star twins

Evolutionäre Streuung der magnetischen Aktivität in kühlen Sternzwillingen

Master thesis | **Masterarbeit**

For the acquirement of the scientific degree
Master of Science (M.Sc.)
in the discipline of Astrophysics

Verfasser:	Desmond Dsouza
Studiengang:	am Institut für Physik und Astronomie
Matrikelnummer:	808491
Erstgutachter:	Prof. Dr. Katja Poppenhäger
Zweitgutachter:	Prof. Dr. Dr. Stephan Geier
Direkter Vorgesetzter:	Dr. Nikoleta Ilić

STATEMENT OF ORIGINALITY

I hereby declare that the submitted Master's thesis is my work and that, to the best of my knowledge, it contains no sources or resources other than the ones mentioned and acknowledged. During the wring the writing of the thesis, I indicated all quotes, citations, and references that were taken from published or unpublished publications, such as books, journals, academic articles, newspapers, reports, etc. Furthermore, the research described in this thesis is based on work conducted at the Leibniz-Institut für Astrophysik Potsdam (AIP) and no part of this thesis has been submitted elsewhere for any other degree or qualification.

Desmond Dsouza

Abstract

Magnetic activity is a phenomenon associated with a star's time temporal and spatial magnetic fields. Stellar magnetic activity decreases as the stars age. This is because activity leads to magnetised winds that cause mass loss. This loss takes away the angular momentum of the star and slows it down. This phenomenon is called magnetic braking or a spindown. A slowly rotating star provides less differential rotation, a key ingredient in the stellar dynamo. The weakened dynamo produces less magnetic activity. However, it is still an open question how deterministic this spindown is in quantitative terms; populations of stars with similar ages can display quite some scatter in their rotation and activity levels. Additionally, studies of co-eval stars older than 700Myr is not feasible because older stars are more than 250 pc away from the Sun and outside the detection limits of current X-ray telescopes.

In this master thesis project, We look at co-eval F, G, K and M spectral-type binaries located in the solar neighbourhood, filtered from co-moving binaries from Gaia data release 2. We use archival X-ray data from Chandra X-ray Observatory and XMM-Newton Space Observatory for our study and use X-ray luminosity as an indicator of stellar activity. Our sample consists of 62 observations of 34 wide binary stars of the same spectral type. The majority of our analysed systems belong to spectral type K or M. We then find the associated scatter ($\Delta \log L_X = \left|\log L_{X,\text{star 1}} - \log L_{X,\text{star 2}}\right|$) in activity between the binary pairs.

Our results show that the activity scatter within the same-age, same-spectral type binary pairs is significantly smaller than the observed scatter of same-mass stars in the solar neighbourhood. We find a mean scatter in co-eval stars as $\mu_{\text{co-eval}}$ 0.30, 0.35 and 0.44 dex in F/G, K and M type stars respectively with standard deviation $\sigma_{\text{co-eval}}$ of 0.15, 0.22 and 0.28 respectively. This varies significantly from solar neighbourhood stars. Our randomised pair generator pairs up random field stars observed by the NEXXUS database and find the average scatter μ_{NEXXUS} as 0.79, 0.75 and 0.96 for F/G, K and M type stars. As Gyrochronology gets calibrated for field stars, our binary sample will improve our understanding of not only the scatter but also the age dependence of the scatter. We also observe a discontinuity in the distribution of our coeval M dwarf sample with no M dwarf pairs observed with a $\Delta \log L_X \sim 0.5$. A future study using a survey mission can help fill the discontinuity in the data.

Zusammenfassung

Magnetische Aktivität ist ein Phänomen, das mit den zeitlichen und räumlichen Magnetfeldern eines Sterns zusammenhängt. Die magnetische Aktivität eines Sterns nimmt mit zunehmendem Alter der Sterne ab. Dies liegt daran, dass die Aktivität zu magnetisierten Winden führt, die einen Massenverlust verursachen. Dieser Verlust nimmt dem Stern den Drehimpuls und verlangsamt ihn. Dieses Phänomen wird als magnetische Bremsung oder Spindown bezeichnet. Ein langsamer rotierender Stern erzeugt eine geringere differentielle Rotation, die eine Schlüsselrolle im Sterndynamo spielt. Der geschwächte Dynamo erzeugt weniger magnetische Aktivität. Es ist jedoch immer noch eine offene Frage, wie deterministisch dieser Spindown in quantitativer Hinsicht ist: Populationen von Sternen mit ähnlichem Alter können ziemliche Streuungen in ihrer Rotation und ihrem Aktivitätsniveau aufweisen. Darüber hinaus ist die Untersuchung gleichaltriger Sterne, die älter als 700 Myr sind, nicht möglich, da ältere Sterne mehr als 250 pc von der Sonne entfernt sind und außerhalb der Erfassungsgrenzen aktueller Röntgenteleskope liegen.

In dieser Masterarbeit untersuchen wir gleichaltrige Doppelsterne vom F, G, K und M-Spektraltyp, die sich in der Sonnenumgebung befinden, gefiltert aus gleichaltrigen Doppelsternen der Gaia Data release 2. Dafur verwenden wir archivierte Röntgendaten des Chandra-Röntgenobservatoriums und des XMM-Newton-Weltraumobservatoriums für unsere Studie und nutzen die Röntgenleuchtkraft als Indikator für stellare Aktivität. Unsere Stichprobe besteht aus 62 Beobachtungen von 34 weit entfernten Doppelsternen des gleichen Spektraltyps. Die Mehrheit der von uns analysierten Systeme gehört zum Spektraltyp K oder M. Wir finden dadurch die zugehörigen Streuungen ($\Delta \log L_X = \left|\log L_{X,\text{stern 1}} - \log L_{X,\text{stern 2}}\right|$) in der Aktivität zwischen den binären Paaren.

Unsere Ergebnisse zeigen, dass die Aktivitätsstreuung innerhalb der Binärpaare gleichen Alters und gleichen Spektraltyps deutlich geringer sind als die beobachtete Streuung von Sternen gleicher Masse in der Sonnenumgebung. Wir finden eine mittlere Streuung in gleichaltrigen Sternen von $\mu_{\text{co-eval}}$ 0,30; 0,35 und 0,44 dex in Sternen vom Typ F/G, K und M mit einer Standardabweichung $\sigma_{\text{co-eval}}$ von 0,15; 0,22 bzw. 0,28. Dies unterscheidet sich erheblich von Sternen in der Sonnenumgebung. Unser Generator für Zufallspaare paart zufällige Feldsterne, die von der NEXXUS-Datenbank beobachtet werden, und findet die durchschnittliche Streuung μ_{NEXXUS} von 0,79; 0,75 und 0,96 für Sterne vom Typ F/G, K und M. Da die Gyrochronologie für Feldsterne kalibriert wird, verbessert unsere binäre Stichprobe unser Verständnis nicht nur der Streuung, sondern auch der Altersabhängigkeit der Streuung. Wir beobachten auch eine Diskontinuität in der Verteilung unserer gleichaltrigen M-Zwerg-Stichprobe, weil keine M-Zwerg-Paare mit einem $\Delta \log L_X \sim 0,5$ beobachtet werden. In eine zukünftigen Studie, die aus einer Durchmusterungsmission besteht, kann diese Diskontinuität in den Daten überbrücken werden.

Contents

CHAPTER 1

Introduction

1.1 Stellar formation

In the beginning ... there were clouds of gases that spanned the interstellar medium. Denser regions of gas clouds clumped together due to gravity and eventually due to gravitational instability formed stars (Kippenhahn et al., 2013). These birthplaces of stars consist of turbulent clouds of gas and dust. Every time a new star is born in these clouds, it imparts mechanical energy (by its relative motion and gravitational interaction) and radiative energy into its surroundings (Guarcello et al., 2010). These feedback mechanisms generate a net angular momentum in these clouds and therefore when stars are formed in these turbulent regions, the angular momentum is imbibed into the new stars. This momentum in the consequent stars shows up as relative motion to each other (circular, elliptical or escape trajectories) and in their rotation along a rotational axis, i.e. stellar rotation.

Figure 1.1: "Pillars of creation" part of M16 nebula captured with the Hubble Space Telescope, HST. Filter: f657n. Data source: Hubble legacy archive.

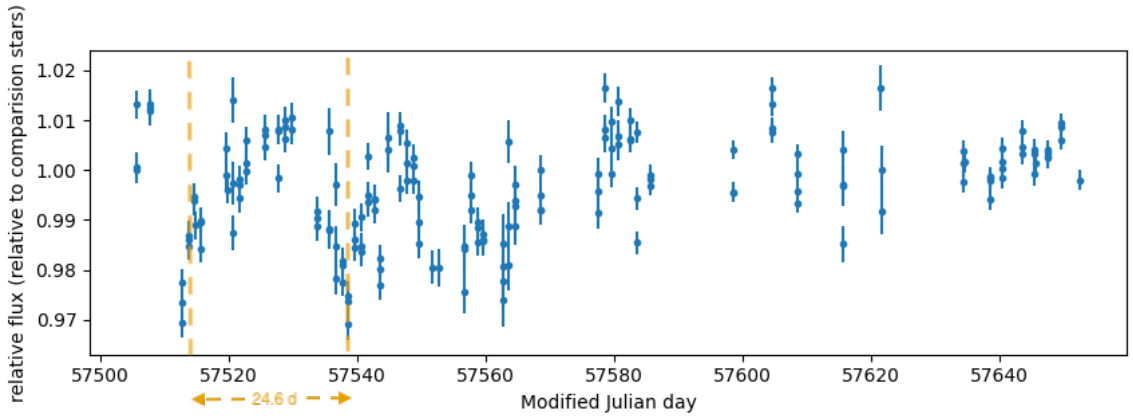

Figure 1.2: Photometric lightcurve of WASP-69 in the B band shows a sinusoidal modulation with a period of ≈ 24.6 days.

Stellar rotation, especially fast rotation is easily observed in young stars through the modulation of photometric lightcurves. Fig.3.1 shows a photometric time series of the star WASP-69 obtained through continuous monitoring (Khalafinejad et al., 2021). Since a time series with underlying periodicity can be disentangled into sinusoidal and cosine waves, a periodogram can be used to find the underlying frequency of the modulation. A Lomb Scargle periodogram applied on the WASP-69 curve tells us that the star rotates with a period of ≈24.6 days.

The periodic modulations on the photometric stellar light curve (LC) are caused due to various stellar features that rotate in and out of view of the observer (here, the telescope) as the star rotates. Features such as starspots and faculae have different brightness when compared to the photosphere. A starspot is darker while a facula is brighter when compared to the photosphere.

Studies on stars in young clusters show that they consist of fast-rotating stars. Fig. 1.3 shows the rotation of stars in young clusters ranging in age from 30-200 Myr. These stars are fast rotating in contrast to our sun, which is 4.5 Gyr old and rotates with an average period of ≈ 27 days. The Sun would therefore be on the top edge of fig.1.3.

The Sun, however, does not rotate as a solid object. Helioseismic studies tell us that its rotation period is a function of latitude and depth (Duvall et al., 1984 and Howe et al., 2000). Fig.1.4 shows one such helioseismic study. Here, r is the distance from the centre of the Sun and R is the radius of the Sun. It can be seen that when we move outwards from the centre of the Sun to r/R= 0.6, the rotation is almost like a solid sphere with a rotational frequency of $\sim$ 430 nHz. However, as we move toward the surface of the Sun, there are vast deviations from this rotational frequency. The region around the equator (0°) is rotating at a frequency of $\sim$ 445 nHz or $\sim$ 26 days. Meanwhile at a latitude of 60° it is $\sim$ 370 nHz or $\sim$ 31.28 days. This phenomenon is called differential rotation[1].

[1]We mentioned single rotation rates for the stars in the open clusters and the sun above. For the sun we refer to an average of rotational velocity, in the case of stars, we cannot resolve the surface of the star. They appear like a point source to the telescope. Therefore any variations in the rotation on the surface of the star are part of the photometric LC and are superimposed in the signal.

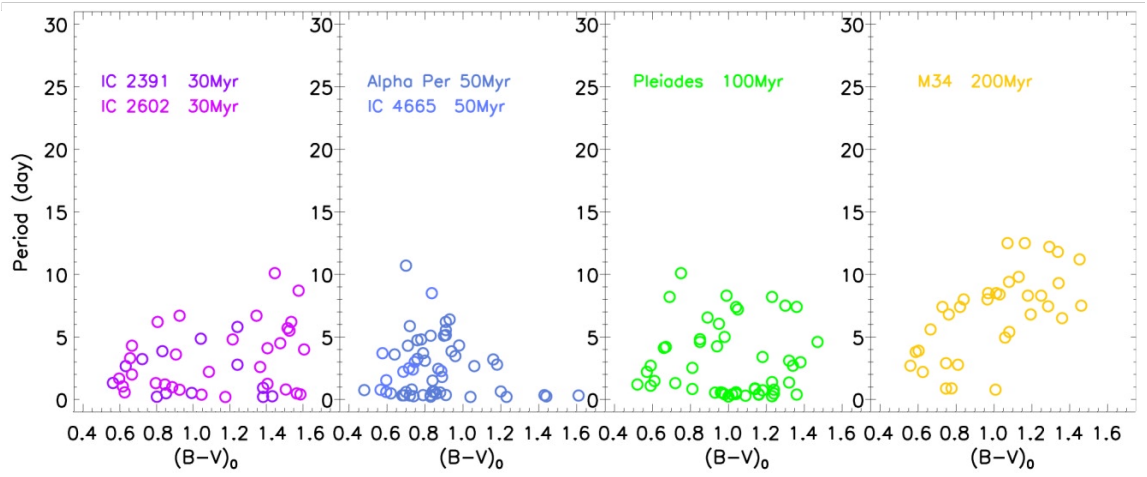

Figure 1.3: Rotation rates of stars in stellar clusters of 30-200 Myr old (Barnes, 2003).

The differential rotation causes shearing in the convective layers of the sun and is considered to be the source of a stellar dynamo that generates magnetic fields (Wilson, 1966, Kraft, 1967, Güdel, 2004). The dynamo efficiency depends on the differential rotation and the convective layer.

However, not all stars have an outer convective zone. M-type stars that have a mass lesser than $0.3M_{\odot}$ are fully convective. Meanwhile, stars of spectral type ∼F5 to M3 have a convective shell and a radiative core. This collection of stars (F, G, K and M)are known as the cool main sequence (MS) stars. They are similar to the Sun in many ways and are believed to have a similar magnetic dynamo. As we move towards the more massive stars ($\geq 1.3M_{\odot}$) in the Hertzsprung–Russell diagram, the convective shell becomes thinner and thinner until there is none. Although there is no convective envelope, a convective zone still exists in the core of the star (Kippenhahn et al., 2013). The convective core is surrounded by a radiative envelope for massive stars. Due to this configuration, most massive stars do not have a magnetic field. Surveys show that $\approx 7\%$ of O-type stars have a detectable magnetic field (Grunhut et al., 2017). However, the origin of this magnetic field is varied and attributed to stellar mergers or a fossil dynamo (Hubrig et al., 2023).

The magnetic fields of stars can be detected using Zeeman Doppler imaging (L. Rosen et al., 2013, Vidotto et al., 2014, L. Rosen et al., 2015 and Strassmeier et al., 2023), but this can be challenging as magnetic fields are complex and the signal can be very weak (L. Rosen et al., 2015). However, the existence of magnetic fields gives rise to observable spatial and temporal phenomena called magnetic activity. This phenomenon includes stellar spots, flares, coronal mass ejections, chromospheric emission, and X-ray emission due to the hot corona. These observables are indirect detections of the stellar magnetic field.

Stellar dynamo models such as the $\alpha\Omega$ dynamo attempt to describe the origin of the magnetic fields for cool MS stars with a convective and a radiative zone (Stix, 1976). Meanwhile, the magnetic field of fully convective M dwarfs is an active field of research but is believed to be fueled by α^2 dynamo(Chabrier and Küker, 2006) among other dynamo models. Regardless of the origin of the magnetic field, all cool

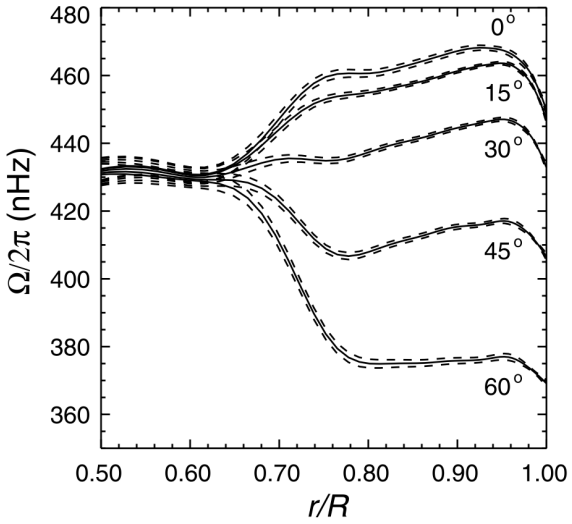

Figure 1.4: Differential rotation observed on the sun using helioseismic study (Howe et al., 2000).

MS stars show similar properties in terms of magnetic activity (Wright et al., 2011).

1.2 Aging in stars

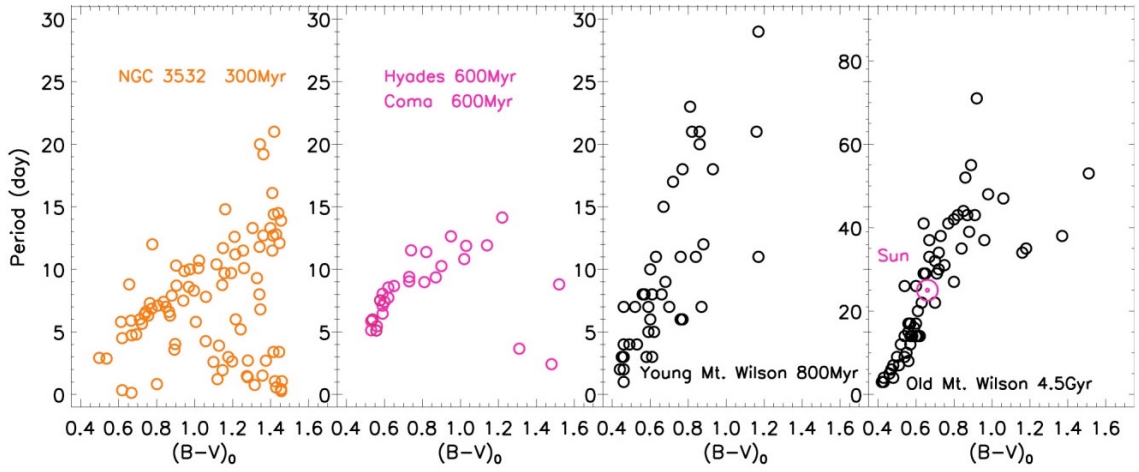

Figure 1.5: Rotation rates of stars in stellar clusters of 300 - 4500 Myr old(Barnes, 2003).

As stars age, their rotation period is observed to increase. Fig. 1.5 shows the observed rotation periods of stars in old open clusters. It was shown by Skumanich, 1972 that there is a correlation between magnetic activity (chromospheric Ca II emission decay) and the rotation periods of a star. More specifically, magnetic activity is high in young fast rotating stars and gets reduced significantly as stars become older and lose angular momentum. The loss of angular momentum was proposed to be due to magnetised winds (Schatzman, 1962). The magnetic fields of stars through magnetised winds drive matter away from the star to large distances. This matter co-rotates with the star and it can escape the gravitational field of the star, thereby taking the angular momentum of the star with it.

Skumanich's observations were later modelled with magnetised stellar wind loss (Kawaler, 1988). Through mass loss models Matt et al., 2015 showed that the mass of the star is a factor in the mass loss and therefore the spindown of the stars. This means that mass loss affects more massive cool stars differently than smaller ones. The loss of angular momentum consequently reduces the differential rotation of the star, thereby directly affecting the magnetic fields and reducing the magnetic activity. Therefore, magnetic activity is directly proportional to the rotation rates. The higher the rotational rates, the more the activity and vice versa.

These magnetised winds are caused by the magnetic fields of the star, however, the origin of the same magnetic field comes from its differential rotation. This feedback loop is called 'magnetic braking'.

The proportionality of magnetic activity with rotation rates of the star is well documented using different activity indicators such as chromospheric emission lines (Douglas et al., 2014, Newton et al., 2017 and Chahal et al., 2023), hot thermal X-ray from the corona (Jeffries et al., 2011, Wright et al., 2011, Stelzer et al., 2016 and Magaudda et al., 2022), photometric variability (Hosey et al., 2015 and Buzasi et al., 2016) and frequency of flares (Davenport et al., 2019).

However, this correlation does not exist for fast-rotating stars when observed in X-rays. It has been observed that Zero Age Main Sequence stars (ZAMS) first go through a 'saturation' regime during the fast rotation phase (Wright et al., 2011). In this saturation state, there is no correlation between the rotation period and the X-ray luminosity. In this phase, stars spin down without affecting L_X. As stars age, they come out of the saturation regime and enter a phase when rotation and activity are correlated.

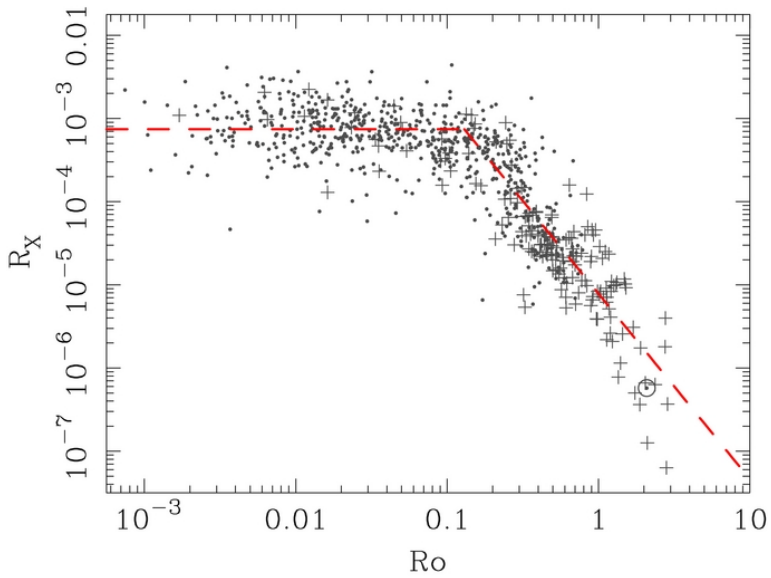

Figure 1.6: Ratio of X-ray Luminosity with bolometric luminosity ($R_X = L_X/L_{bol}$) plotted against Rossby number $R_O = P_{rot}/\tau$ for stars of stellar type G2-M4 (Wright et al., 2011).

The ratio of X-ray luminosity with bolometric luminosity ($R_X = L_X/L_{bol}$) can be characterised by the two-part function Eq. 1.1. Where R_O is the Rossby number defined as the ratio of the period and the convective turnover time ($R_O = P_{rot}/\tau$) and $R_{O\,sat}$ is the Rossby number in the saturation regime. Fig.

1.6 shows the saturation regime lies below 0.1 R_O.

$$R_X = \begin{cases} R_{X\,sat}, & \text{if } R_O \leq R_{O\,sat} \\ C\,R_O^{\beta}, & \text{if } R_O > R_{O\,sat} \end{cases} \tag{1.1}$$

where β in eq 1.1 is a the slop of the power law in the unsaturated regime. It is a value determined by observation (Wright et al., 2011) as $\beta = -2.18 \pm 0.16$. C is a proportionality constant. $R_{X\,sat}$ for G2-M4 stars is -3.13±0.08 (Wright et al., 2011) and $R_{X\,sat}$= -3.13±0.12 for fully convective M-dwarfs (Wright et al., 2018).

Why does the corona saturate for fast rotators? This is an open question in stellar astrophysics. Many different research directions are working towards understanding this further. One section suggests that this could be due to the saturation of the magnetic dynamo (Gilman, 1983, Vilhu and Walter, 1987) while another suggests that it could be due to a saturation of the filling factor of active regions on the star's surface (Vilhu, 1984). Another hypothesis suggests that this saturation is due to centrifugal stripping caused due to fast rotation (Jardine and Unruh, 1999). While we still do not know why this saturation happens, we do know that it happens and what are the R_X values expected from a star in the saturation regime.

1.3 Evolutionary scatter of activity

When we look at the scatter of X-ray luminosity expected for a particular Rossby number in fig: 1.6, we can see that there is quite some scatter in the saturated and the unsaturated regime even though it follows the trend of Eq. 1.1. Could this scatter in values of R_X (for the respective R_O) be an artefact of intrinsic scatter that is part of stellar evolution? This thesis will attempt to constrain the natural scatter of activity in cool stars. However, before that, we shall take a look at the scatter of $\log L_X$ in the solar neighbourhood.

The database for Nearby X-ray and extreme UV emitting Stars (NEXXUS[2]) (Schmitt and Liefke, 2004) is a collection of all cool star detections from the Röntgensatellit (ROSAT) space telescope in the solar neighbourhood. It provides us with a perfect sample to characterise this scatter. Fig 1.7a shows stellar activity range in solar neighbourhood F, G, K and M spectral type stars obtained from the NEXXUS database. Fig. 1.7b shows a more recent study by Caramazza et al., 2023 on M dwarfs in 10 pc solar neighbourhood.

The F/G sample shows a scatter of 3 orders of magnitudes, spanning a range of $\log L_X[\text{erg/s}] \approx 27-30$, while the K types have $\log L_X[\text{erg/s}] \approx 27 - 29$ and the M dwarf have a scatter $\log L_X[\text{erg/s}] \approx 26 - 29$.

However, solar neighbourhood stars are not coeval. They are field stars that were most probably formed at different times. To study the intrinsic scatter in the solar neighbourhood we need to remove the age dependence in our sample and find coeval stars. This brings us back to clusters. Stars in open clusters are coeval. Freund et al., 2020 studied magnetic activity in the Hydes cluster using X-ray luminosity. The X-ray luminosity of type M stars, K and G spans ≈ 3dex, ≈ 2 dex, and ≈ 2 respectively.

[2]https://hsweb.hs.uni-hamburg.de/projects/nexxus/nexxus_old.html

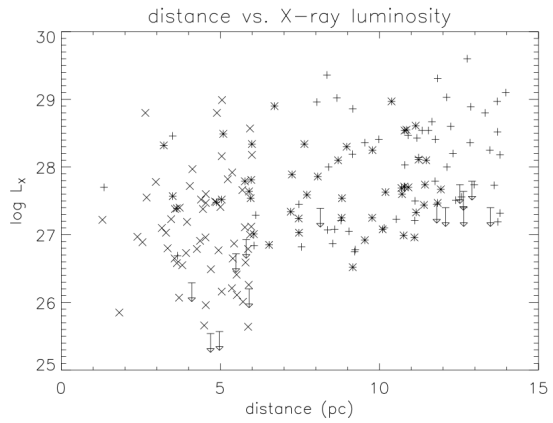

(a) NEXXUS study of L_X in F, G, K and M type stars in the solar neighbourhood (Liefke and Schmitt, 2005). F/G type, K type and M type stars are represented as plusses, asterisks and crosses respectively.

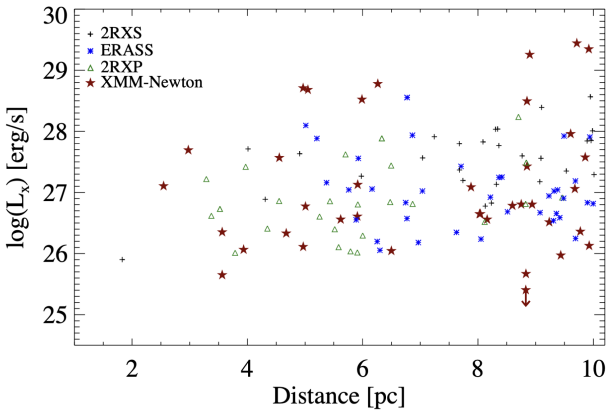

(b) M type stars in the solar neighbourhood (Caramazza et al., 2023).

Figure 1.7

A similar study was done recently on the Praesepe and the Hydes cluster (Núñez et al., 2022). Fig. 1.8 shows us the magnetic activity in the clusters and their respective scatter. We can see that R_X values in both of the clusters are more constrained than $\log L_X$. Fig. 1.9 shows us how much scatter is seen within each stellar type overplotted with Eq. 1.1. It is clear that F and G-type stars have constrained activity (R_X) and do not scatter more than one order of magnitude meanwhile K and M dwarfs have much more scatter. Since both the clusters are $\approx$ 700 Myr old only M3.5-M7 are still in the saturated regime, with M0-M3.5 exiting the saturation regime [3].

A look at coeval stars of the same type shows us that they too have a scatter in activity it is, however, more constrained compared to field stars. We would like to expand our understanding of the scatter in cool stars for various ages (i.e. evolutionary scatter) and not be restricted only to 700 Myr. Multiple studies of clusters spanning different ages would therefore be required to constrain this evolutionary scatter. A study like this would require a much more sensitive X-ray telescope as open clusters older than 700Myrs are not present within 250pc of the Sun. Distances greater than 250 pc are very far for the instrumental sensitivities of current-day x-ray telescopes. Additionally, older stars have lower X-ray emissions when compared to their younger counterpart, which makes it even more challenging.

We however have another way to study the intrinsic activity scatter in coeval stars. We can study the smallest possible co-eval 'cluster', i.e.: The binary system. Stellar binaries help us expand our understanding of scatter without waiting for the launch of a more sensitive telescope. It will allow us to study the activity scatter of coeval stars in different stellar ages as we have a multitude of stellar binaries in the solar neighbourhood at distances close enough for existing X-ray telescopes to receive a detectable signal. However, a drawback would be that the ages, although varied, would be unknown. Spectroscopic studies of T Tauri stars tell us that components of binary systems have an age uncertainty of less than 1Myr (Hartigan and Kenyon, 2003). It is however not improbable that lone stars could be captured gravitationally

[3] In section 1.1 we discussed that spin-down is dependent on the initial mass of the star. This is why we see some stars in the saturation regime while others like F and G are having lower activity and spinning down. This phenomenon has also been observed through Gyrochronology studies. The spindown time scales in increasing order based on spectral type are F, G, K and M i.e F type stars spin down very early on, while M dwarfs can stay fast rotating for a long time.

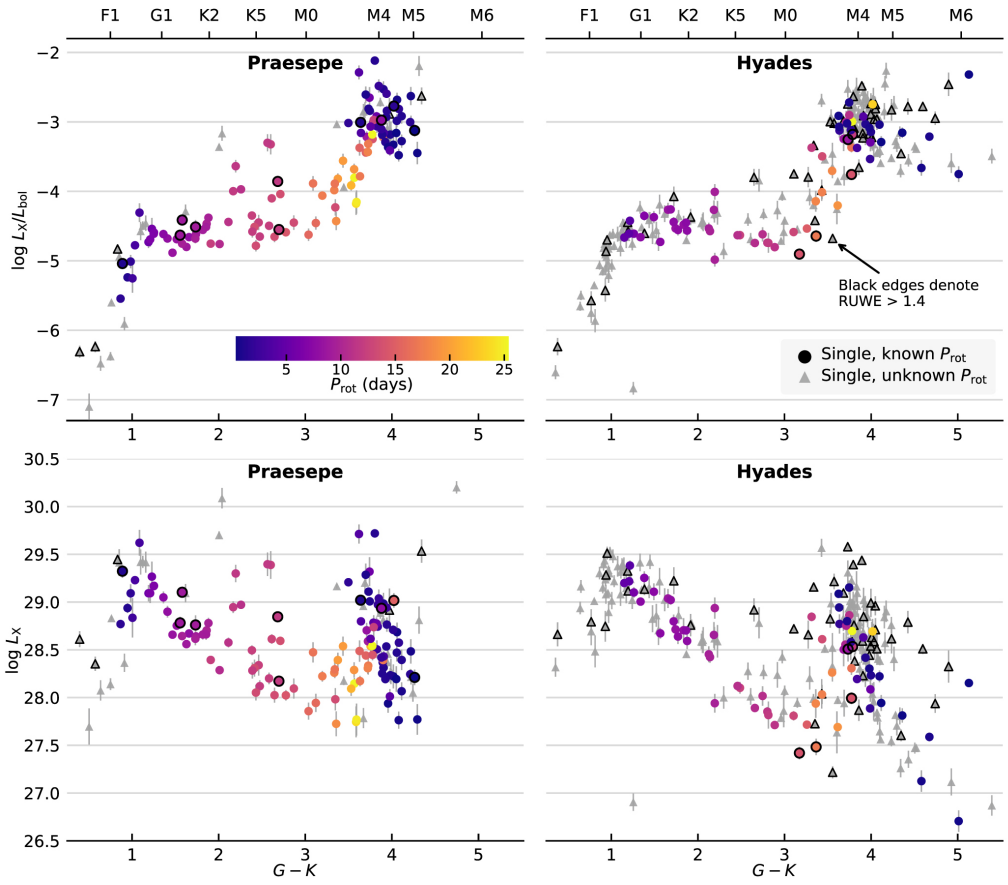

Figure 1.8: Scatter of X-ray activity in Praesepe and the Hydes cluster (Núñez et al., 2022).

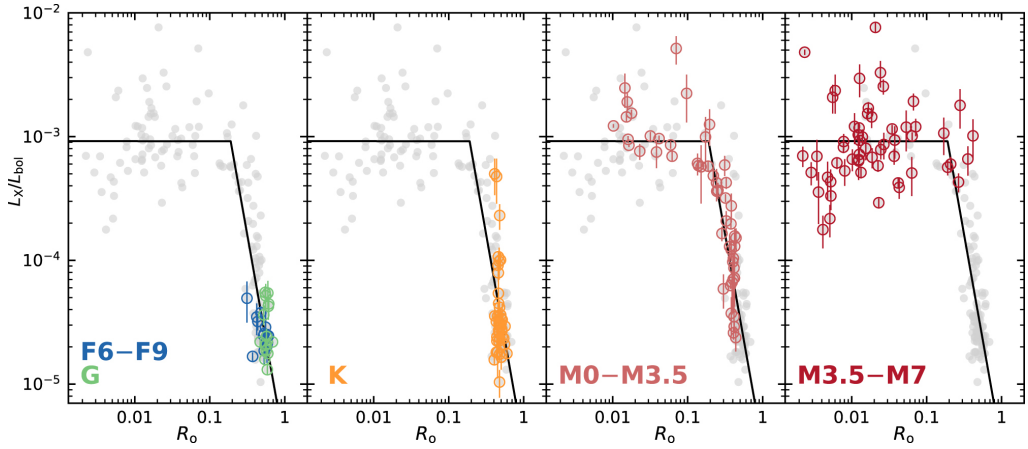

Figure 1.9: Scatter of X-ray activity in Praesepe and the Hydes cluster (Núñez et al., 2022).

and form a binary system, however, recent gyrochronology studies show us that binary stars are mainly coeval with rare exceptions (Gruner et al., 2023).

We use X-ray archival data in this study to look at the corona of the stars. The magnetic activity of a star can heat the corona to UV- X-ray emitting temperatures. This is also of particular interest in exoplanet-hosting stars as the evolution of exoplanets depends on the properties of the host star. Stellar emission in the UV and X-ray bands can directly cause the evaporation of exoplanetary atmospheres. This slow and steady evaporation has been observed in many systems and has been estimated to be highly significant in the evolution of exoplanet atmospheres (Sanz-Forcada et al., 2011). Mass loss rate estimation of planets is based on assumptions about X-ray and UV emission from host stars. A constrained understanding of the scatter in activity especially in the unsaturated regime can help better estimate the role of stellar magnetic activity in the evolution of the exoplanetary atmosphere.

Exoplanets, specifically hot Jupiters can also be found in very close orbits around their host stars. So close, that it is predicted to magnetically or tidally affect the host star (Cuntz et al., 2000). The phenomenon of exoplanets interacting with their host star is known as star-planet interaction (SPI)(Poppenhaeger, 2022). There is evidence that shows increased activity in host stars of hot Jupiters when compared to other stars without an exoplanet (Poppenhaeger and Wolk, 2014). Our study of natural scatter in activity in the same spectral type cool stars can be used as a baseline to prove the existence of tidal SPI.

In the next sections, we describe other stellar activity tracers and the study of stellar corona using X-rays for this study.

1.4 Observing magnetic activity in cool stars

As mentioned in section 1.2, there are multiple ways to estimate magnetic activity. This includes photometric variability, stellar spots, frequency of flares, chromospheric emission lines and thermal X-ray. We describe the method used in each of these processes and why X-ray was selected for this study.

Photometric variability is defined as the standard deviation of a star's brightness when compared to comparison stars. Photometry uses comparison stars in the field of view (FOV) of the CCD that are relatively "not variable" to calibrate the signal of the object of interest. Variations of brightness on the surface of a star can occur due to stellar features that enter and exit the line of sight of the telescope. Stellar features such as star spots and faculae cause variability on the surface of the star. These features are an outcome of magnetic fields on the star, therefore, magnetically active stars show high photometric variability. These variations are measured in mmag. Since young stars are more magnetically active, they show higher variability than older stars (Hosey et al., 2015).

We do not use photometric variability as long-term monitoring is required to study the mmag changes occurring in the lightcurve. This variability is subject to the sample of comparison stars chosen from the FOV. Additionally monitoring binaries is complicated as they are in orbit with each other. Given that we want to analyse the same spectral type of binaries, both stars would be indistinguishable for an automated pipeline and risk the contamination of the lightcurve with the other binary component's signal.

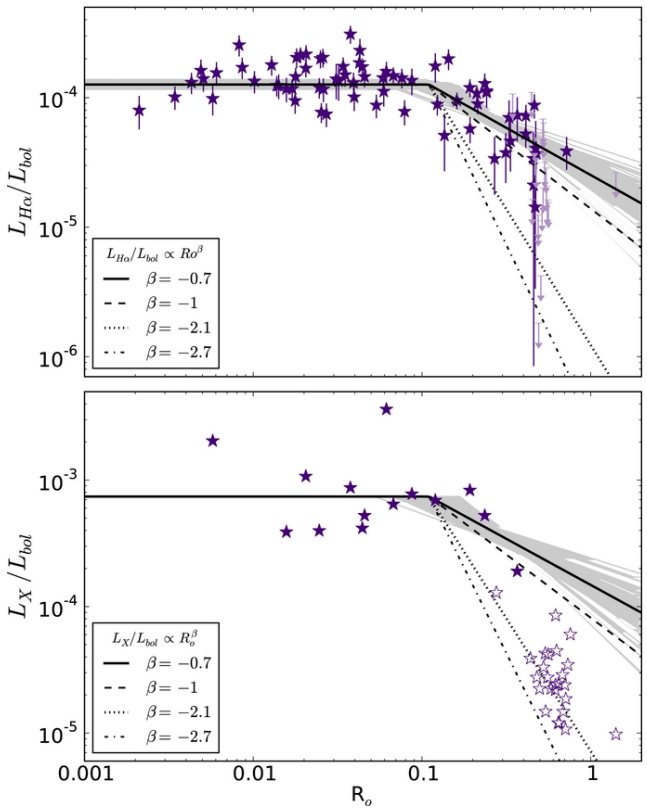

Figure 1.10: X-ray indicator of R_X is more sensitive than chromospheric Hα/L_{bol} to study activity-rotation(Douglas et al., 2014)

This therefore would require individual hand selection of the star of interest through each CCD image (out of hundreds of images). Additionally, mmag changes of brightness can be challenging to trace for very slow-rotating stars as the signal-to-noise ratio would be very low.

The chromospheric index R'_{HK} is more accurate than photospheric measurements for stellar activity, this is because bright faculae can dilute photospheric indicators of activity (Chahal et al., 2023). The line core of H (λ3968 Å) & K (λ3933 Å) and Ca II can be used to calculate R'_{HK} indices (Mamajek and Hillenbrand, 2008). This index is calculated using the strength of band ratio measurement of the emission lines. This is then subtracted by an underlying photometric contribution to give us the R'_{HK}. Alternatively for the chromosphere, the Mount Wilson index (S_{MW}) or the equivalent widths of Hα (λ6550 Å) can also be used to determine the activity (Douglas et al., 2014). R'_{HK} for the Sun is $\approx$ -4.91.

Chromospheric flux depends non-linearly on photospheric magnetic flux density. This has been observed on entire stars and on solar features. However, this nonlinearity is not seen with X-ray surface flux measurements. There is a linear relation between the photospheric magnetic flux density and X-ray surface flux. The diversion that makes the flux-to-flux conversion non-linear comes from the fact that the chromosphere experiences radiative losses (Güdel, 2004).

Chromospheric measurement is also subject to noise from stellar events such as starspots. This noise is known as the radial velocity (RV) jitter and is observed in all ages of cool stars. Chromospheric emission lines also have a basal emission that contaminates it. Each line has a different basal contribution that has

to be subtracted to get an accurate measurement of magnetic activity.

Although these other tracers can be used to estimate the magnetic activity, X-ray emission is most sensitive to magnetic fields, since the coronal emission of the star is due to heating caused directly by the magnetic field (Güdel, 2004 and Drake and Stelzer, 2023). It is also very sensitive to the turning point between saturation and the unsaturation regime (Douglas et al., 2014) as can be seen in fig. 1.10. X-ray measurements also need a few ksec of time and therefore it accessible using survey missions such as Rosat or eROSITA.

In the next section, we shall discuss the characteristics of the stellar corona and observations using X-ray.

1.5 The stellar corona

The outermost layer of the stellar atmosphere consists of confined plasma that is as hot as a T_{corona} = 1-10MK. This layer is called the corona. One of the big open questions in Stellar Astrophysics is "What makes the corona so hot?". Although the exact mechanism of heating is unknown, it is widely believed that this plasma is heated by the conversion of magnetic flux energy to heat energy in F, G, K and M-type stars. Since the plasma is confined due to magnetic pressure, there is an equilibrium between the magnetic pressure and the gas pressure. Using this, it can be estimated that the magnetic fields are of the order of a few Gauss (Drake and Stelzer, 2023).

The plasma has an electron density of $n_e \sim 10^8 - 10^{10}\text{cm}^{-3}$, it is therefore considered to be optically

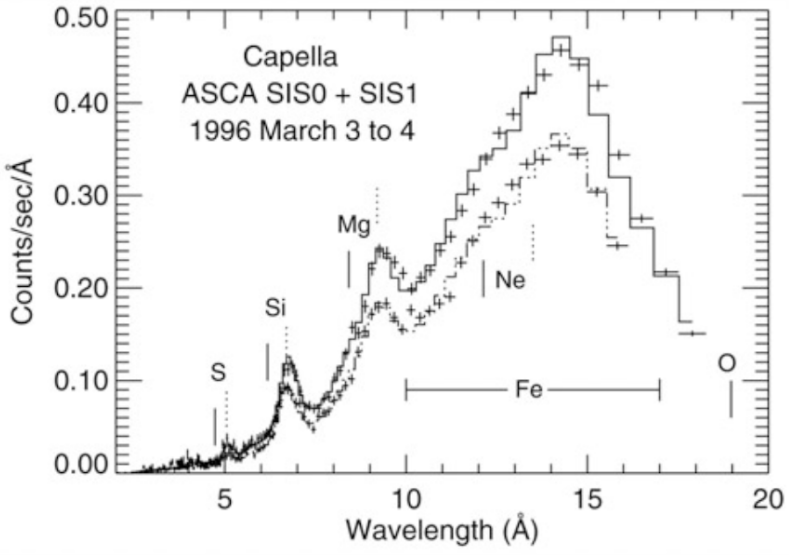

Figure 1.11: Spectrum of Capella (G3) constituting C, N, O, Ne, Mg, Si, S, Ar, Ca, Fe, Ni and He emission (Drake and Stelzer, 2023).

thin. Since the corona is heated steadily, it stays in thermal equilibrium. The coronal plasma emission is dependent on the temperature, chemical composition and the density of the plasma. However, The density of the plasma affects only a minority of the emission spectra and these lines are only visible in

high-resolution X-ray spectrum. Therefore studies involving low-resolution spectra need not account for the density of the corona. Fig. 1.11 shows the X-ray spectrum of Capella captured in 1996 by the Advanced Satellite for Cosmology and Astrophysics (ASCA). The lines obtained from a best-fit optically thin plasma emission model are superimposed on the data. Strong He-like transitions are denoted by dotted lines while H-like Lyα in O, Ne, Mg, Si and S are denoted by solid lines. A big part of the spectral range is denoted by the n=2 transition shown by Fe ions.(Drake and Stelzer, 2023)

Fig. 1.12 shows high-resolution spectra of Capella using the Chandra space observatory (Brinkman et al., 2000). All the Fe lines that contribute to the rise in emission in Fig. 1.11 can be seen here. It should be noted that most of the strong emission lines (higher counts) observed in Capella that are characteristic of the temperature of the corona are present in the band gap of 6Å-60Å (2.0- 0.20 keV). We shall therefore use this energy band for our study.

Studies of the Sun tell us that there are multiple regions of X-ray emission from the corona. Assuming the same effects observed on the sun also occur on other cool stars, we can say that the surface flux of the star consists of coronal holes (CH), background corona (BKC), cores of active regions (AR) and active regions (AC) (Orlando et al., 2001). This is best summarised in the "Sun as a Star" series of papers. For our study of stars, there is no spatial resolution available for a stellar corona and what we observe is just a point source. We therefore observe an integration of the complex structures of the Corona as a single signal. The intensity of a spectral line $u \rightarrow l$ where u is the upper excitation level and l is the lower level from the stellar corona as a function of temperature is written as the volume integral Eq. 1.2. The quantity $n_e^2(T)V(T)$ is known as the volume emission measure (VEM). $G_{ul}(T)$ is the radiative decay rate per unit electron density. A is the total abundance of an element with respect to the hydrogen number density (Drake and Stelzer, 2023).

$$I_{ul} = AK_{ul} \int_{\Delta T_{ul}} G_{ul}(T) n_e^2(T) dV(T) \tag{1.2}$$

$$\mathrm{DEM}(T) = n_e^2(T) \frac{dV(T)}{dlogT} \tag{1.3}$$

VEM can be described in a logarithmic differential form as the differential emission measure (DEM) Eq. 1.3. Using the DEM, the entire spectra of the EUV/X-ray can be modelled for a given temperature this helps us find the temperature of the corona for a given hardness ratio as done in Chapter 3. We describe the Hardness ratio in more detail therein.

1.6 X-ray Observatories

X-ray Astrophysics cannot be conducted using Earth-based telescopes as Earth's atmosphere absorbs X-rays. Space-based telescopes are therefore needed for our study of stellar corona. X-ray telescopes are not designed like optical refractor or reflector telescopes. Electromagnetic waves in the X-ray regime are challenging to focus at a point using optical lenses or mirrors. This is because X-rays don't reflect or refract through mirrors or lenses, but rather go through them. To solve this problem specialised parabolic and hyperbolic mirrors are placed at glancing angles to reflect the X-rays to a focal point (Gondoin et al.,

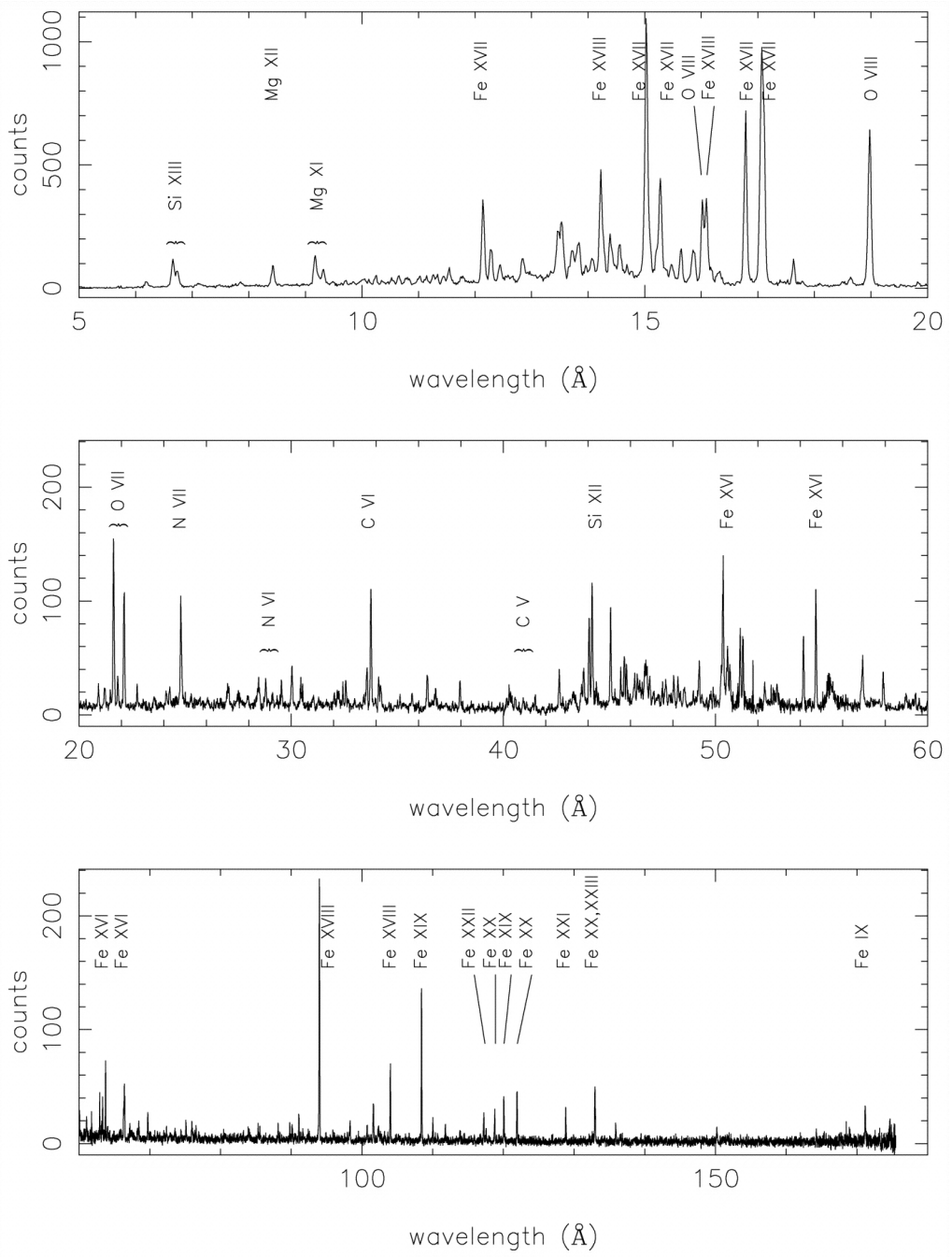

Figure 1.12: High-resolution spectrum of Capella observed with Chandra X-ray Observatory using the HETG grating with superimposed emission lines predicted by a simple emission model. (Brinkman et al., 2000)

1998). However, these mirrors should be placed concentric and very close to each other to capture the maximum amount of photons. Due to this concentric mirror design, the mirrors look like shells of an onion when looked head-on (fig:1.14). A specialised X-ray detector can then be placed at the focus to detect the photons.

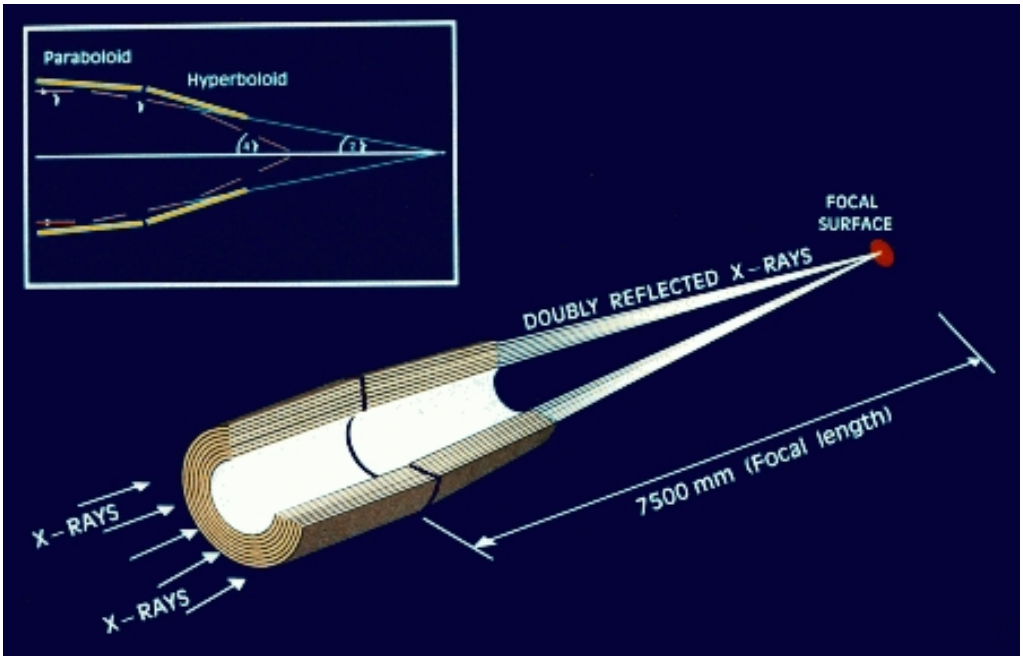

Figure 1.13: Cross section of XMM-Newton telescope lens. Image credits: Gondoin et al., 1998

X-ray emission from astrophysical sources is so scarce that the telescope detects individual photons and can isolate individual photon detections. Some detectors can provide the energy of the photons that are incident on them. Therefore, the information that can be obtained about that photon is the X and Y position of the photon on the CCD, the time the photon hit the CCD and the approximate energy of the photon (based on the accuracy of the detector). The coordinates of the incident photon on the CCD can help us construct an image that tells us which star/source the photon came from. The time of detection can be used to create a time vs. intensity plot (time series). This light curve can help identify flares or other features present in the X-ray signal. Meanwhile, the energy resolution can be used to create an energy vs intensity plot (spectrum). Since energy directly relates to the wavelength and frequency of radiation, this data can be used to create an X-ray spectrum.

In our study, we decided to use X-ray telescopes specifically designed for pointed observations. These observations are normally conducted with long exposure times when compared to survey missions. The longer exposure times are specifically useful for our study as the stars have a higher chance of getting detected.

1.6.1 XMM-Newton Space Observatory

The XMM-Newton telescope was launched by the European Space Agency (ESA) in December 1999. It is the successor to the EXOSAT telescope. We summarise relevant technical specifications for the tele-

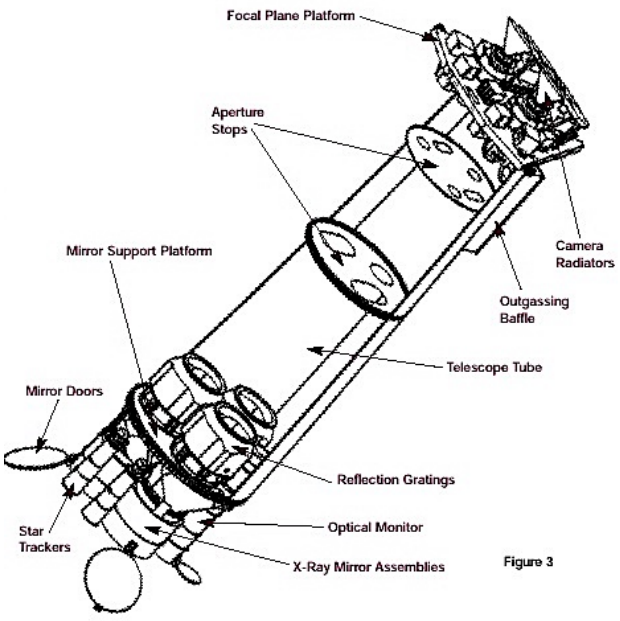

Figure 1.14: The XMM-Newton space telescope. Source: ESA

scope using the XMM-Newton observatory paper by Jansen et al., 2001.

The telescope has a wide field of view (FOV) of 30 arcmin and the telescope consists of four major parts i.e. The Focal Plane Assembly (FPA), Telescope tube, mirror support platform and the service module. The Focal Plane Assembly (FPA) is the most important part of the telescope that concerns observers. In Fig: 1.9, the FPA lies on the Focal Plane Platform. It consists of the following parts:

1. European Photon Imaging Cameras (EPIC): The 3 EPIC instruments can observe with an energy range of 0.15 to 15keV with a spectral resolution of $E/\Delta E \sim 20 - 50$ and angular resolution of 6 arcsec full width half Maximum (FWHM). One out of the three EPIC instruments uses a PN detector which is illuminated from the rear side and is extremely efficient in detecting X-rays homogeneously for the wavelengths between 0.5 to 10keV. The other two EPIC components use a metal oxide semiconductor (MOS) detector. This detector is sensitive to the soft X-rays (below 5keV)

2. Reflection grating spectrometer (RGS) readout cameras: The 2 RGS instruments can be used for X-ray spectroscopy in the energy range of 0.33-2.5keV. This energy range has various X-ray emission lines that can be used as diagnostic tools to understand the physical conditions of the emitting source. In stellar astrophysics, the X-ray spectrum can help us classify the temperature of the Corona by fitting the observed spectra to that of a model spectrum as described in Sec. 1.5. However, the source to be studied should be bright as we need enough photons in the energy range to construct a spectrum.

3. Optical Monitor (OM): The OM is a coaligned telescope sensitive to the 180-600nm (0.0068 - 0.002 keV) range i.e. optical and UV range. It has three optical and three UV filters. The OM is a very sensitive telescope and counts the photons incident on it, this is why it cannot observe very

bright objects as it can permanently damage the telescope.

1.6.2 Chandra X-ray Observatory

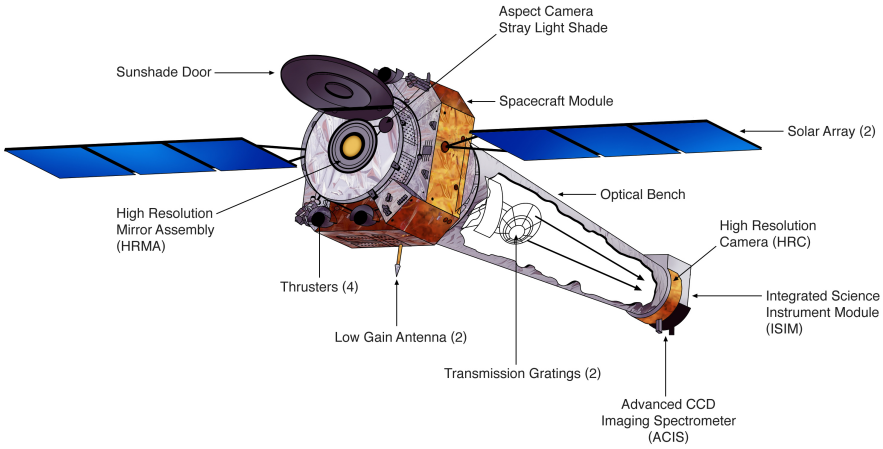

Figure 1.15: The Chandra space telescope. Source: NGST & NASA/CXC

The Chandra X-ray Observatory was launched by the National Aeronautics and Space Administration (NASA) in July 1999. It has a much higher resolution than the XMM-Newton telescope. We summarise important technical specifications from the Chandra X-ray observatory overview paper below. (Weisskopf et al., 2000).

The telescope has two instruments at the focal point. A High Resolution Camera (HRC) and the Advanced CCD Imaging Spectrometer (ACIS). It also has two gratings for spectroscopy. The High Energy Transmission Grating (HETG) and the Low Energy Transmission Grating (LETG).

1. High Resolution Camera (HRC): The HRC as the name suggests can take very high-resolution images of the targets. The angular resolution of the HRC sensor is 0.5 arcsec. HRC-I is a sensor optimised for imaging and has a large effective FoV of 31x31 arc mins. Meanwhile, HRC-S is optimised for spectroscopy and works in conjunction with the LETG to read the spectrum. The HRC however, does not have any energy resolution and only lists the time of detection of individual photons.

2. Advanced CCD Imaging Spectrometer (ACIS): The ACIS consist of CCD arrays that provide us with the image of the target and the energy resolution of the incident photons. It consists of 2 arrays of CCDs that is ACIS-I and ACIS-S. ACIS-I is designed to capture wide-field images of 16x16 arcmin, while the ACIS-S is used in conjunction with the LETG grating. ACIS-S has a FoV of 8x8 arcmin and provides the best energy resolution.

The HETG has a varying resolving power of $(E/\Delta E)$= 800 - 200 for 1.5keV to 200keV respectively. However, it is optimized for bright sources. For lower energies of 0.07 - 0.2keV, LETG can be used as it provides a spectral resolving power of $(E/\Delta E)$ = 1000.

CHAPTER 2

Sample selection

We begin with the publicly available binary catalogue from El-Badry and Rix, 2018. This catalogue is selected because it has an estimated purity [1] of $\approx 99.8\%$ and classifies Main-sequence pairs (MS), White dwarf (WD) pairs and MS-WD pairs within 200 pc of the Sun. The binaries have a projected separation of 50 to 50,000 AU and were found using the Gaia Data release 2 catalogue (Gaia Collaboration et al., 2016, Gaia Collaboration et al., 2018). The catalogue contains 51,916 pairs of MS binary stars. We aim to classify these stars into spectral types F, G, K and M using the absolute magnitude and photometric colour.

To estimate the absolute magnitude (M_G), we use the publicly available geometric distance (d) estimates for Gaia stars (Bailer-Jones et al., 2018). The absolute magnitude is then estimated using the distance modulus relation (Eq. 2.1) assuming no interstellar extinction.

$$M_G = m - 5 * log_{10}(d_{\text{parsec}}) + 5 \tag{2.1}$$

Type	$G - G_{\text{rp}}$	M_G
F	0.218 - 0.435	2.44 - 4.26
G	0.435 - 0.542	4.26 - 5.446
K	0.542 - 0.91	5.446 - 8.095
M	0.91 - 1.645	8.095 - 16.5

Figure 2.1: Photometry table for spectral type classification. Source: Pecaut and Mamajek, 2013.

We then classify the stars into spectral types by referring to the photometry table[2] made publicly available by Pecaut and Mamajek, 2013. $G - G_{\text{rp}}$ and M_G is used for the classification of colour and absolute magnitude respectively. We classify our stars with the spectral types F, G, K and M by taking the mean of the upper and the lower limit of the spectral type boundary to create an interval for our analysis (fig. 2.1). This spectral type classification is done for both components of the binary. Only systems with the same spectral type companions are saved. We now have a collection of coeval same spectral type cool stars. Fig. 2.2 shows these stars on a colour-magnitude diagram with the MS binary catalogue.

[1] 0.2 % estimated contamination from other possible sources.

[2] https://www.pas.rochester.edu/∼emamajek/EEM_dwarf_UBVIJHK_colors_Teff.txt

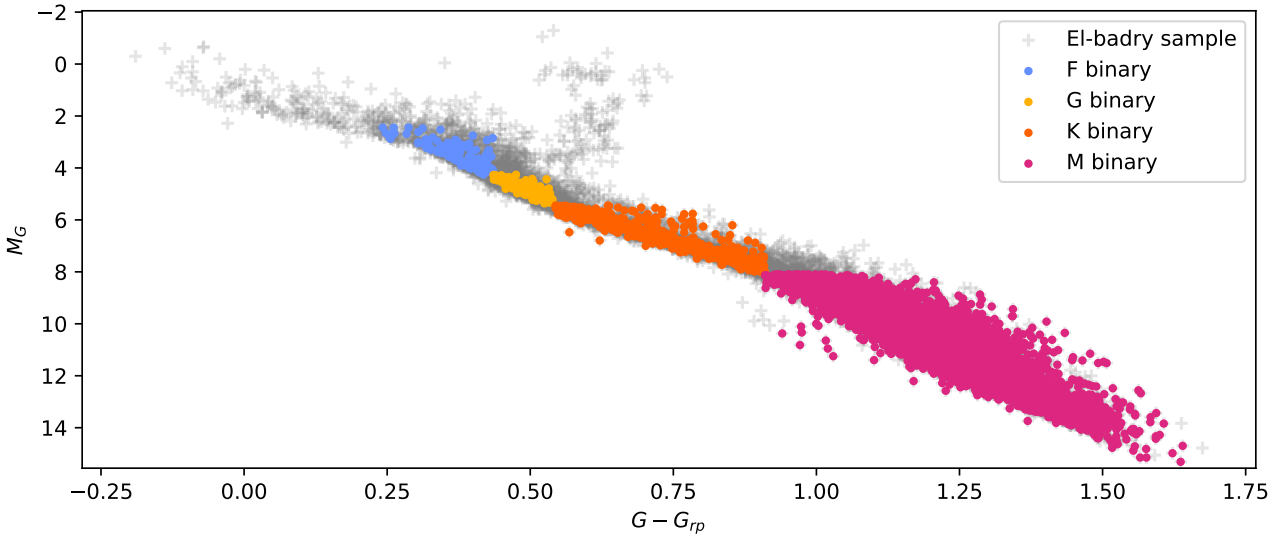

Figure 2.2: All MS binaries plotted alongside the same colour MS binaries.

We then filter the binary stars based on the angular resolution of the X-ray telescopes. We do this as the point spread function (PSF) of the two telescopes are different. The XMM-Newton sample consists of systems with a separation of more than 15" while that of Chandra is more than 2". We arrive at this number by doubling the instrumental FWHM of the respective telescope. This is required as this filters non-resolvable binaries out of our sample.

All systems with one star at a distance of less than 100pc are considered for further analysis. The 100pc distance cut represents the solar neighbourhood stars. A subset of this sample is also created with a 50pc distance cut for the Chandra X-ray observatory. The spatial resolution of the Chandra X-ray observatory is higher than that of XMM-Newton, however, higher resolution means lower sensitivity, therefore a 50pc distance cut is chosen for Chandra. The distance cut allows us to have stars with higher chances of detectability. This then gives us an XMM sample consisting of 18 F, 18 G, 131 K and 1512 M type systems and the Chandra sample with 50 6 F, 15 G, 74 K and 840 M type systems (fig. 2.3).

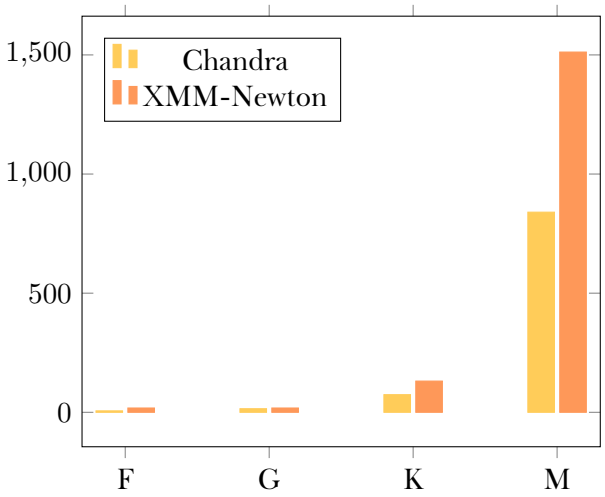

Figure 2.3: Sample comparison between the two telescopes before data retrieval.

We now have a sample of systems to look for in the XMM-Newton and Chandra archive. However, we cannot use the stellar Gaia coordinates to look for the data in the archives. The Gaia coordinates are derived for a reference year of J2015.5 in the International Celestial Reference System (ICRS) (Gaia Collaboration et al., 2016). The Chandra and XMM-Newton missions on the other hand have been ongoing since July 1999 and September 1999 respectively. We compensate for this by evolving the coordinates of our sample by using the proper motion of the stars. We set the date for our evolved coordinates to J2010. This is approximately the mid-observation period from 1999 to 2022. This preliminary selection allows us to better match our sample to the X-ray observations. The evolved coordinates can then be used to retrieve the data for our observation.

CHAPTER 3

Data Analysis

3.1 XMM-Newton Space Observatory

The XMM-Newton catalogue DR-11 (Webb et al., 2020) is a serendipitous survey of the data observed by the XMM-Newton space telescope. It consists of 895,415 detections found in 12,210 XMM-Newton EPIC observations. Using our evolved coordinates from Chapter 2, we conduct catalogue matching by looking for sources first in the 30" cone and then a fine matching with the 5" cone. Stars with proper motion of greater than 10 mas yr^{-1} are searched with a 10" cone to account for higher uncertainty in position. This method of catalogue matching is similar to that used by Foster et al., 2022. Systems with only one star detected in the catalogue were filtered out. This can happen due to two causes:

- The PSF of the stars overlapped and was classified as one source. Since the PSF can significantly change based on where the counts fell on the CCD, there is a possibility that the source counts of the two binary components were merged into one and were detected by the catalogue pipeline as one source.
- The other component is too faint to be detected.

Regardless of the cause, we would like to have stars with both components detected. The XMM-Newton DR-11 catalogue comes with automated flags that encode the reliability of the detection. detections that have a sum flag less than or equal to 1 are kept for analysis. There is only one system with a sum flag of 3. This flag tells us that a source is detected at a CCD position where spurious detection can occur (Webb et al., 2020). Since we do not look at the individual event files for XMM-Newton, we decided to remove this system from further analysis. A detailed description of the catalogue flags can be found in the catalogue paper.

The flux values in the XMM catalogue DR-11 are based on the assumption that the underlying spectra are a power law with index 1.7 and a neutral hydrogen column density of $N_H = 3 \times 10^{20}$ (S. R. Rosen et al., 2016). (N_H accounts for absorption due to neutral hydrogen in line of sight of the object of interest and the CCD). A power law, however, is not the characteristic shape of the coronal spectra. The coronal spectra consist of emission lines from an optically thin plasma in a collisional ionisation equilibrium as discussed in section 1.5. This emission can be described using the Astrophysical Plasma Emission Code, APEC (Smith et al., 2001).

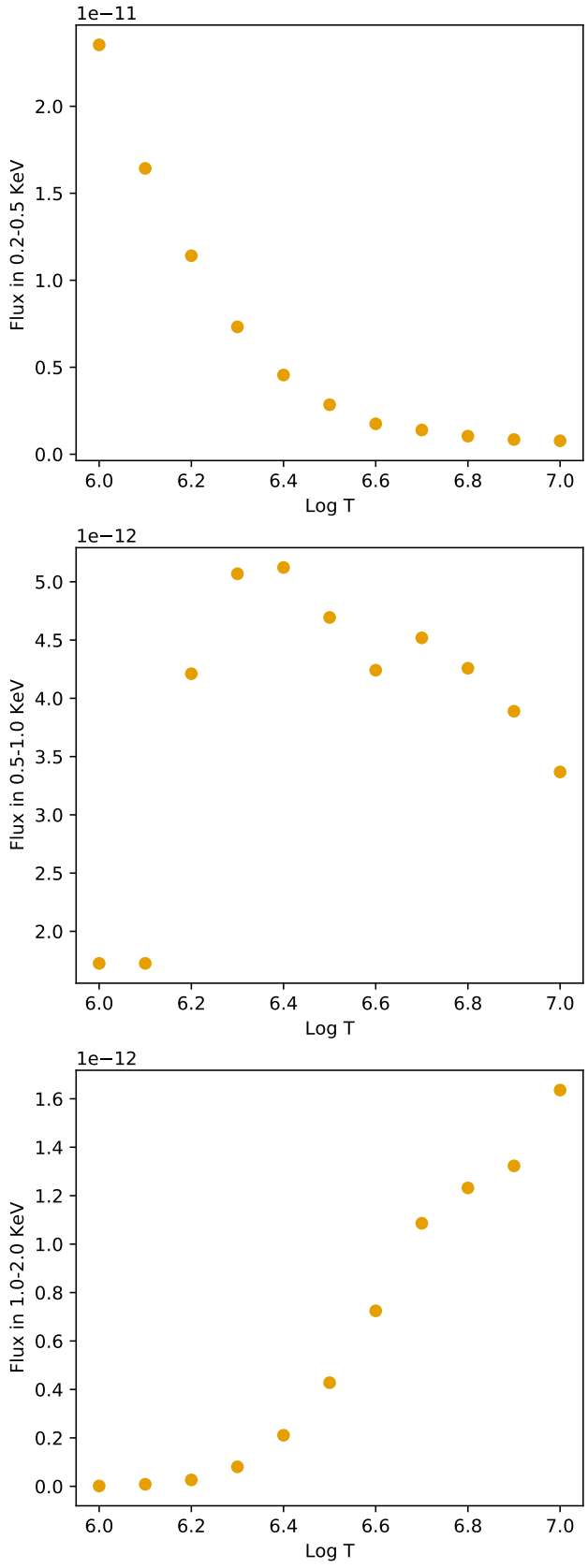

Figure 3.1: Characteristic flux curves for various coronal temperatures for the three energy bands assuming a count rate of 1ct/s.

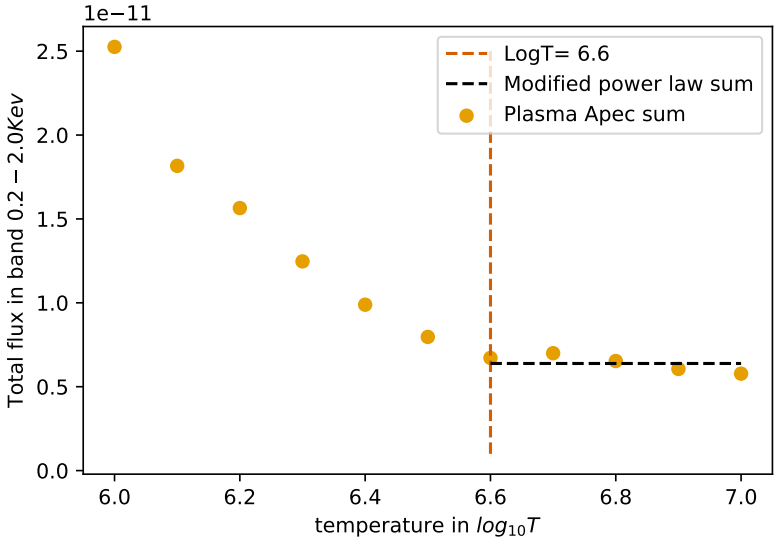

Figure 3.2: Area of linearity represented as a dotted line.

To be able to use the flux values from the catalogue, we need to convert the power law fluxes to plasma APEC fluxes. The plasma APEC flux is based on an integration of emission lines from plasma in equilibrium, meanwhile, a power law assumes a source to be emitting synchrotron radiation at a certain temperature due to electrons moving at relativistic velocities (for example accreting matter around a massive object). Since emission lines are temperature-dependent some lines can be more intense than others at specific temperatures. This relation therefore cannot just be one conversion factor K, but rather a set of conversion factors, K_{T} based on the temperature of the stellar corona.

For the study of stellar activity, we would like to have the flux in the energy band of 0.2-2.0 keV as this is where most of the coronal X-ray emission lies (check section 1.5 for a detailed description of the stellar corona). The three catalogue bands that cover this energy range are SC-EP-1, SC-EP-2, and SC-EP-3 with bandwidths of 0.2-0.5 keV, 0.5-1.0 keV and 1.0 to 2.0 keV respectively. To find a conversion factor between the two fluxes, we need to study how the fluxes change for different coronal temperatures.

We conduct a count-to-flux conversion on the Portable, Interactive Multi-Mission Simulator (`PIMMS`). We use the Chandra X-ray Center (CXC) web interface called `WebPIMMS` v4.12a as per the recommendation of the High Energy Astrophysics Science Archive Research Center (HEASARC) division of the National Aeronautics and Space Administration (NASA). We create a hypothetical source with 1 count per second, a photon index of 1.7 and Galactic $N_H = 3 \times 10^{20}$. This is in line to the power law assumption of the catalogue as mentioned above. We also assume a detection on the MOS camera with a Medium filter. The artificial source can be used to check how the two different flux models will react at different temperatures of the Corona. We then do a similar exercise with plasma APEC. We create a set of temperatures and find the corresponding flux in each band (Fig. 3.1).

We can see that stars with coronal temperature of logT= 6.6 and above (marked as an orange line in fig. 3.2) do not show temperature dependence and can be accounted for by using a single multiplier factor (represented in grey). This 'linear fit' is the average of the flux values above logT=6.6.

$$K_{\text{Temp}} F_{\text{power}} = F_{\text{APEC}}(\text{Temp}) \tag{3.1}$$

$$F_{\text{power}} = F_{EC1} + F_{EC2} + F_{EC3} \tag{3.2}$$

$$K_{\text{Temp}}(F_{EC1} + F_{EC2} + F_{EC3}) = F_{\text{APEC}}(\text{Temp}) \tag{3.3}$$

For stellar coronal temperatures of logT 6.0-6.6 we can see an increasing trend in flux for lower coronal temperatures. For stars lying in this range, we have to multiply a factor that is dependent on the temperature to get the plasma APEC values. To calculate this factor, We need to take into account the coronal temperature of the star. A closer look at the fig. 3.1 shows that the fluxes for the stars lying in the range of logT 6.0-6.6 have higher flux in EC1 and EC2 band. We can therefore create a count ratio, CR (similar to hardness ratio) that can be used to identify stars at these temperatures.

$$\text{CR} = \frac{\text{counts in 0.2-0.5 KeV}}{\text{counts in 0.5-1.0 KeV}}. \tag{3.4}$$

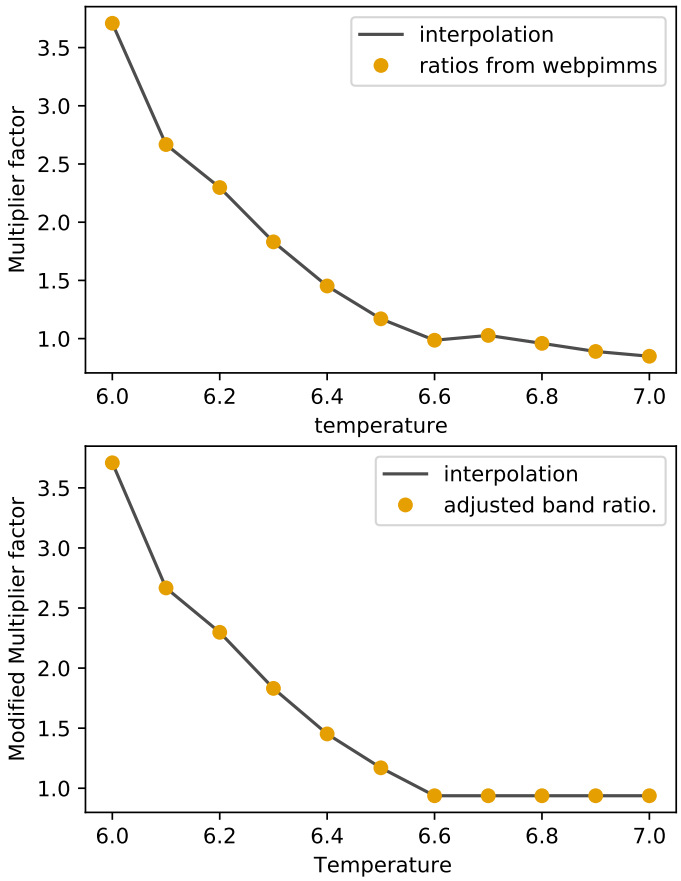

Figure 3.3: Comparison of modified multiplier factor vs orignal `WebPIMMS`

$$F(\text{CR}) \rightarrow T_{\text{estimated}} \tag{3.5}$$

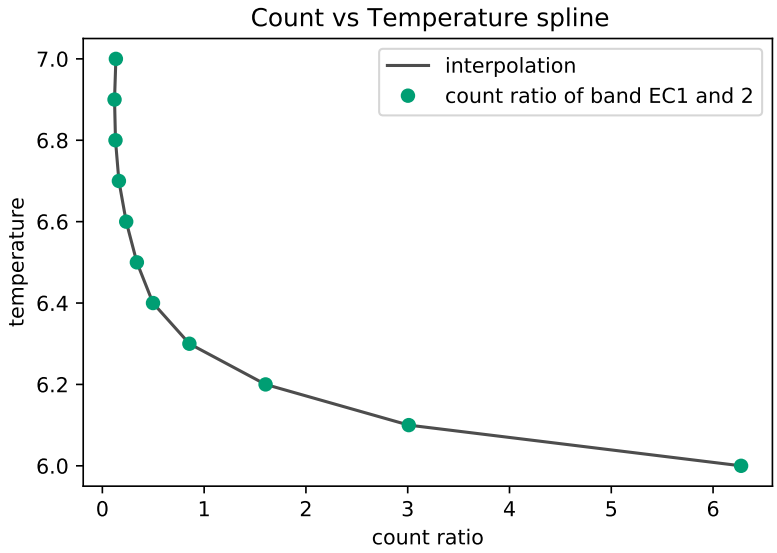

Figure 3.4: Count ratio to estimated temperature (log T)

$$G(T_{\text{estimated}}) \rightarrow \text{MMF} \tag{3.6}$$

A CR value corresponds to a specific temperature in the logT 6.0-7.0 range. A spline function $F(\text{CR})$ between CR and temperature is created to estimate the coronal temperature. A second spline function $G(T_{\text{estimated}})$ can then be used to find an MMF from the coronal temperature (Refer Eq. 3.5 and Eq. 3.6). The MMF is then multiplied to the flux values from the catalogue giving us plasma APEC fluxes. Refer Fig:3.4 and Fig:3.2 for spline functions $F(\text{CR})$ and $G(T_{\text{estimated}})$ respectively.

3.2 Chandra X-ray Observatory

3.2.1 ACIS

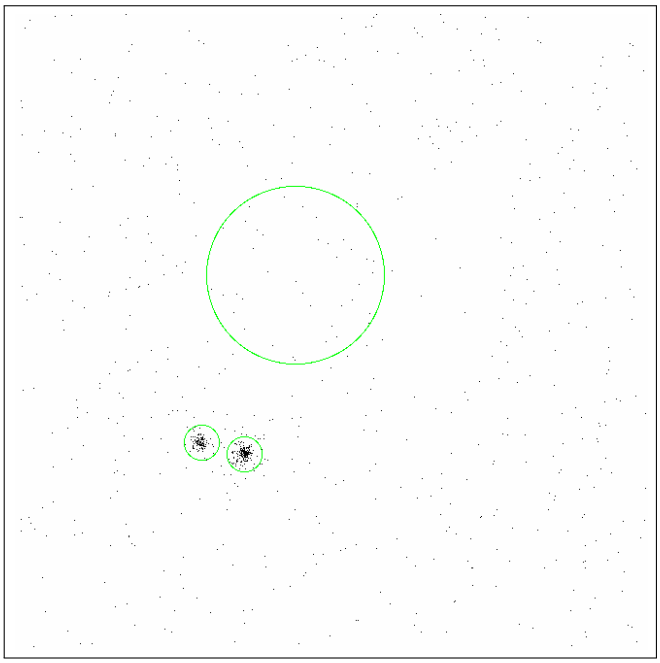

Figure 3.5: Extraction regions for system HD48766 and HD48767 on SAO-DS9(Obs. ID: 23353).

Chandra Search and Retrieval (ChaSeR) an online tool provided by CXC is used to search the Chandra Data Archive. We use evolved coordinates of our stars as obtained in Chapter 2. The extraction region for the photons is marked using the region tool in SAO-DS9 (Joye and Mandel, 2003) in the events file. We create extraction regions for the source and the background (fig. 3.5). The radius of the background is selected to be 5 times bigger than that of the source regions. The size of the region depends on where the star is located on the CCD, this is because the outer edge of the CCD is affected by PSF elongation. This is an instrumental effect and can be accounted for by using bigger extraction regions. If the star is significantly off-axis, the source extraction region could be as high as 5". However, most stars were in the range of 1-2". We reject bright sources in which the PSF are visually merged or lie on the border of the CCD as this indicates loss of signal.

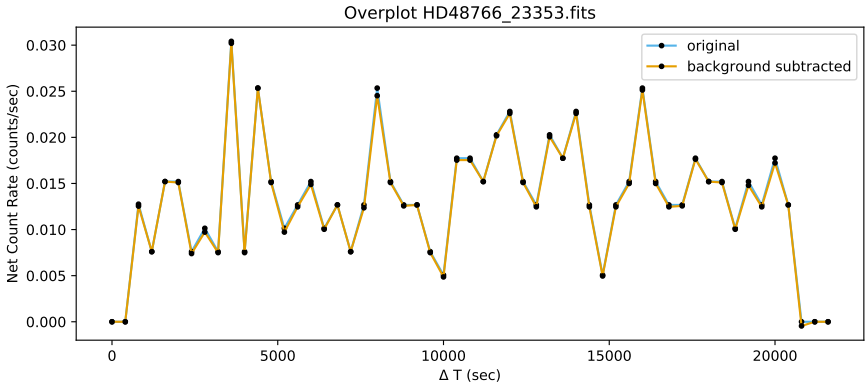

Figure 3.6: Lightcurve of HD48766 to check for erroneous background.

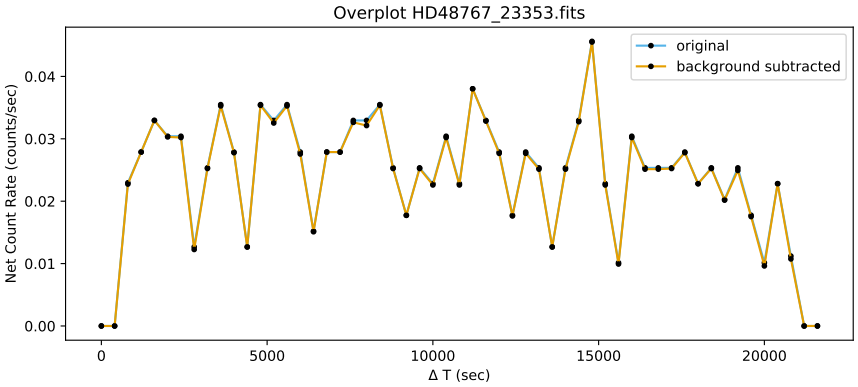

Figure 3.7: Lightcurve of HD48767 to check for erroneous background.

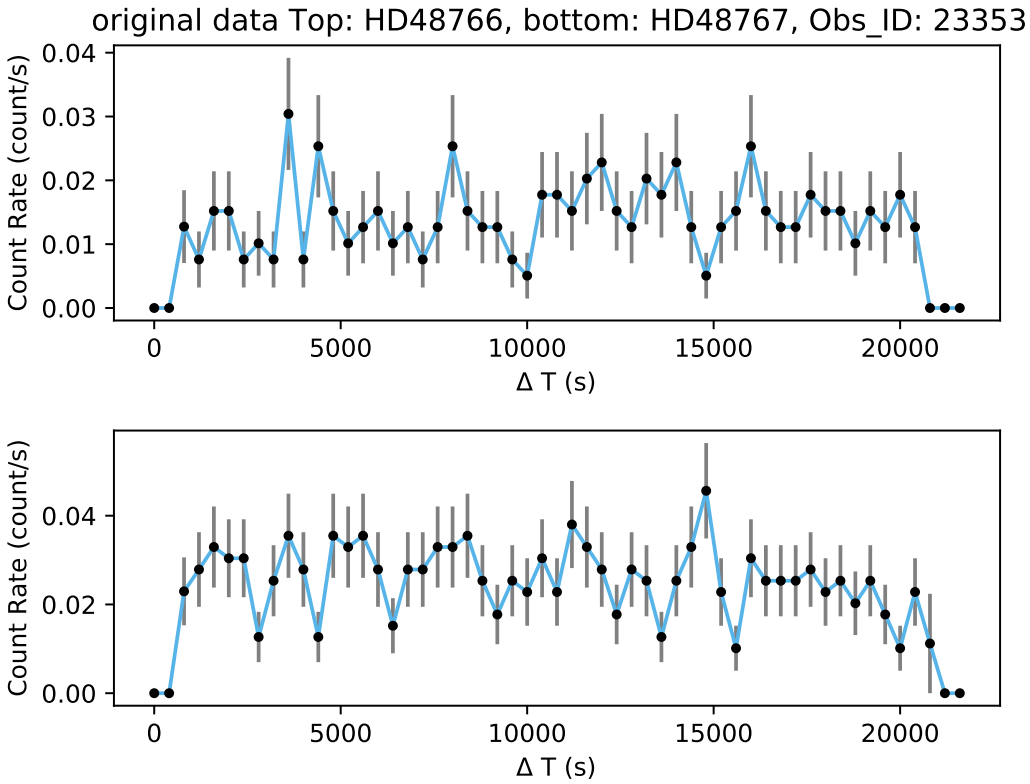

Figure 3.8: Non background subtracted lightcurve of binary components to check for variability.

Faint sources that were not distinguishable by the eye were marked based on the proper motion-evolved coordinates. For evolved coordinates that are very close to each other, we created smaller regions that do not overlap.

The photons are then extracted and lightcurves (LC) are generated using Chandra analysis software, CIAO-4.14 (Fruscione et al., 2006). We follow the guidelines as per the CIAO online documentation. The `dmextract` and `dmcopy` functions were used for photon extraction. Each LC was then examined individually. We looked particularly for flares, instrumental artefacts and erroneous background. Background subtracted LC is used to identify erroneous background (fig. 3.6- 3.7). LC in which both the components of the stars have a peak at the same time could have an erroneous background that contaminated the

observation, we do not find any cases like these. Non-subtracted LC of both stars are plotted together to look for correlation of variability in the stars (fig. 3.8). We do not find any correlation visually in our plots.

We additionally identify and remove stellar flares from our dataset as it can over-estimate the flux of a quiescent corona. A summary of this is presented in Appendix D: "Flare Removal". Flares cannot be identified for faint sources due to fewer photons, however, we still provide the pipeline with information about the flares in case the flares are visually significant on the LC even though it is a faint source. The faint source pipeline is described in section 3.2.3.

Once we have a flare-less LC, we can characterise the temperature of the stellar corona. We start by first subtracting the normalised background from the source photons to get the net X-ray photons from the star (eq. 3.7). Using these net counts, we calculate the hardness ratio (HR) of the star. As seen in fig. 3.1 the coronal emission lines lying between the range 0.2-0.5 keV have higher flux contribution in stars with coronal temperatures logT$<$ 6.5 (first plot) and similarly lines within 1.0-2.0 keV contribute more in flux for stars above logT$>$ 6.5 (third plot). We therefore define our hard band (H) as 0.2-0.7 keV and soft band (S) as 0.7-2.0 keV (Eq: 3.8) for the estimation of the HR.

The X-ray flux F_X is then estimated through the count rate (f_X) and a conversion factor C_X (Eq. 3.10). We use the same method as used by Ilic et al., 2022 to estimate the flux. We describe this below.

$$\text{net counts} = \text{source counts} - \left(\text{background counts} \times \frac{\text{area of source}}{\text{area of background}}\right) \tag{3.7}$$

$$\text{Hardness ratio} = \frac{H - S}{H + S} \tag{3.8}$$

$$f_X \text{ (cts/s)} = \frac{\text{net counts}}{\text{exposure time}} \tag{3.9}$$

$$F_X = C_X f_X \tag{3.10}$$

Since our sample spans various observation cycles, it cannot be assumed that the CCD efficiencies stayed the same through 22 years of operation. We therefore require observation cycle specific C_X to calculate F_X. Our sample contains data from observation cycles 1 to 22. The observations are also in different instruments of Chandra including ACIS-I and ACIS-S.

To estimate F_X, We conduct a count rate to flux conversion on `WebPIMMS`. We assume a source with F_X of 1e-14 in the band gap of 0.2 - 2.0 keV. The count rate at varying steps of logT is then tabulated for this hypothetical source. We also calculate the count rates in the H and the S bands with the same steps of logT to estimate the associated HR values. Eq. 3.10 is then rearranged to find the temperature-specific conversion factors for specific HR values obtained from our stars.

A linear spline interpolation is then created to bridge the gap in data points. Since `WebPIMMS` provides us only with discrete values of logT, a spline interpolation is needed to estimate the C_X[1]. Ilic et al., 2022

[1]The HR values are essential to estimate the logT and C_X, however not all stars have enough photons for an accurate HR estimation. This can happen when there are no photons in one of the band. In this case, we assume a logT= 6.477 and then find

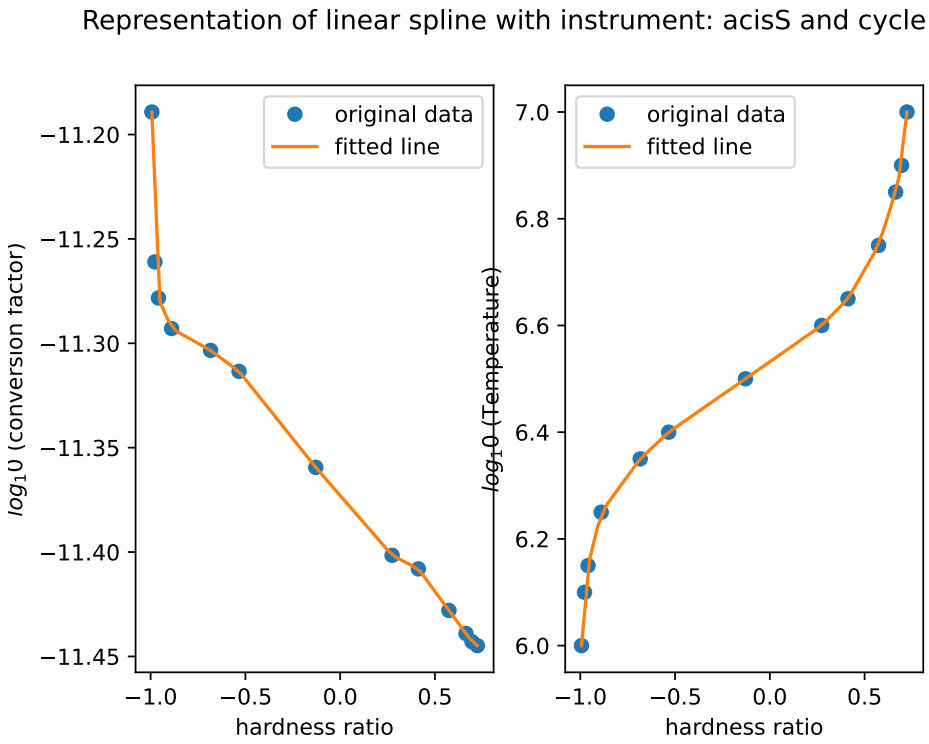

Figure 3.9: HR to conversion factor interpolation in observation cycle 7.

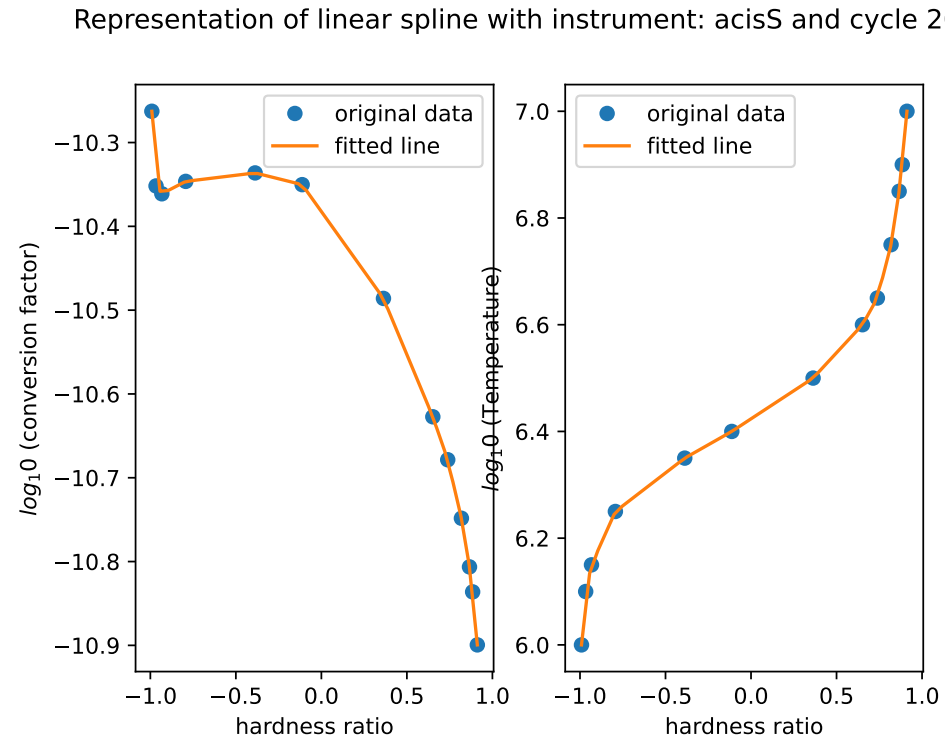

Figure 3.10: HR to conversion factor interpolation in observation cycle 20.

uses a linear spline between C_X and HR. However, we use the logarithmic values of C_X with the HR for the spline interpolation as it fits a linear curve better. Fig. 3.9 and 3.10 show the variation of the conversion factors for different observation cycles.

3.2.2 HRC

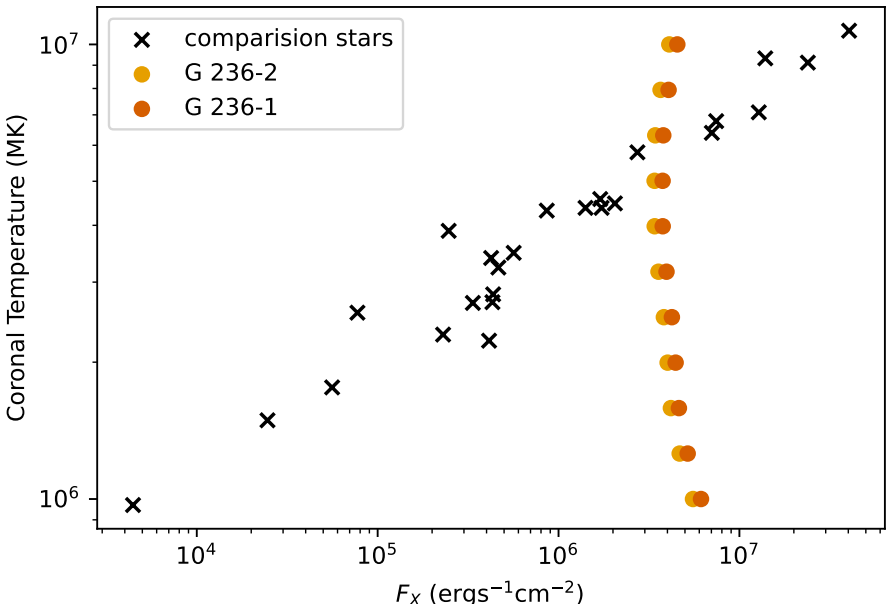

Figure 3.11: Johnstone and Güdel, 2015 sample used as comparision stars to estimate L_X in G 236-1 and G 236-2 system (Obs ID: 6655).

The Chandra High Resolution Camera (HRC) offers high-resolution X-ray data of the stars, however, it does not have energy resolution. The HRC camera is however sensitive to the 0.08-10.0 keV range of photons. We use a method described by (Ilić et al., 2023) to estimate the Luminosity and temperature of the stars. We use the observationally constrained relation obtained by (Johnstone and Güdel, 2015) for surface flux and coronal temperature. we refer to the stars in this bu Johnstone and Güdel as JG stars.

The HRC data consisted of HRC-S LETG (Obs ID 13651, 1880, 22344, 22876) and HRC-I with no filter (obs ID: 6655). We convert the flare subtracted count rate of the stars to the X-ray flux for a grid of temperatures between logT 6.0 to 7.0 in steps of 0.1dex using the `WebPIMMS` online tool. We specify the appropriate instrument and filter during this process. For the spectroscope, we only use the zeroth order as this is where most of the flux is concentrated. The other part of the flux is diffracted into a spectrum across the CCD. `WebPIMMS` accounts for the diffracted photons by the spectrograph.

The point of intersection of the JG stars and the grid of temperatures from the Chandra sample is assumed to be the X-ray surface flux of the star. We only use the fluxes nearest to the point of intersection on the grid and do not interpolate the values (fig. 3.11). The surface fluxes obtained after subtracting the

the C_X for the specific observation cycle.

flares (Appendix B: Flare removal) are used. The fluxes obtained are then converted to Luminosity using the steps described below. There were no faint sources in the HRC data. The lowest count was ≈ 550.

3.2.3 Faint sources

Our sample of stars contains a few faint sources. We categorise all sources with less than 100 photon counts as a faint source. The photon counts in a faint source are so low that the probability distribution of the PSF is no longer in the Gaussian regime, but rather in the Poisson statistics regime. There are two ways to find a detection for a weak X-ray source. We make use of a Bayesian method instead of a classical method to study the faint sources. The benefits of using a Bayesian method over the classical method are described by Kraft et al., 1991. We use the same method for our study to estimate the photons and to classify non-detections.

$$P(N) = \frac{e^{-\lambda}\lambda^{N}}{N!} \tag{3.11}$$

A Poissonian distribution is described by a probability function P(N). λ is the mean number of events (in our case photon counts) detected in time t, while N is the total number of events. Assuming the apriori knowledge that the source counts will have a background contribution, we get a probability function of $f_{N,B}(S)$ (Eq. 3.12). The probability that the source lies between a given range of $S_{\rm min}$ and $S_{\rm max}$ (upper and lower limits) is given by the confidence level (Eq. 3.13), CL. We use a 3 σ confidence interval to categorise our detection.

$$f_{N,B}(S) = C\frac{e^{(S+B)}(S+B)^{N}}{N!} \tag{3.12}$$

$$CL = \int_{S_{\rm min}}^{S_{\rm max}} f_{N,B}(S)dS \tag{3.13}$$

The normalisation constant C in Eq. 3.12 is:

$$C = \Big[\int_{0}^{\infty} \frac{e^{-(S+B)}(S+B)^{N}}{N!}dS\Big]^{-1} = \Big(\sum_{n=0}^{N}\frac{e^{-B}B^{n}}{n!}\Big)^{-1} \tag{3.14}$$

3.3 Flux to Luminosity

The fluxes and the upper limits can now be converted to X-ray luminosity[2] (L_X) using the canonical equation 3.15. We use distance estimates (Bailer-Jones et al., 2018) to estimate the X-ray luminosity of the star. Here r is the distance to the system. The difference in L_X of the two components of the binary indicates the natural scatter of magnetic activity of the system (Eq. 3.16).

[2]For stars that were not detected, we have calculated the Luminosity using the upper limits

The errors of bright sources are found by propagating the errors from the number of counts. Errors in the Chandra bright source pipeline are estimated by assuming a Gaussian error with 1σ or 68% confidence interval (CI). We calculate the CI for bright sources by Eq. 3.17. Here n is the net source photon counts and N is the observed counts. Bright sources in general have symmetric Gaussian errors, but faint sources do not. This is because the faint source pipeline estimates the error by using a Poissonian distribution that is skewed. This skewness is therefore propagated to the errors in L_X. The XMM-newton sample, meanwhile, uses the errors described in the catalogue.

$$L_X = 4\pi C_X f_X r^2 = 4\pi F_X r^2 \tag{3.15}$$

$$\Delta \log_{10} L_X = |\log_{10}(L_{X,star1}) - \log_{10}(L_{X,star2})| \tag{3.16}$$

$$CI = (n - \sqrt{N}, n + \sqrt{N}) \tag{3.17}$$

CHAPTER 4

Results

Our study of natural scatter in activity of cool stars began with a catalogue of wide binaries in the solar neighbourhood of 200pc (El-Badry and Rix, 2018). Both the components of the binary were filtered based on their spectral type into F, G, K and M-type stars based on their colour (Pecaut and Mamajek, 2013). This process provided us with co-eval similar mass stars. We then filtered our sample into XMM-Newton and Chandra based on angular resolution and the possibility of getting a detectable signal from the respective telescopes. X-ray data for the stars were found in the XMM Newton DR11 catalogue and the Chandra archive. A detailed description of this process has been provided in the previous sections of this thesis.

Our data set consists of a mix of pointed and serendipitous observations. X-ray luminosity (L_X) and respective upper limits were found for the components of the binary. Our goal is to isolate the natural scatter of activity in the binary components. Since L_X is an indicator of activity, we define scatter of activity as $\Delta \log_{10} L_X = |\log_{10}(L_{X,star1}) - \log_{10}(L_{X,star2})|$.

Table. 4.1-4.4 shows the list of analysed systems obtained from the archives and analysed through our pipeline. In Appendix B: 'Analysis caveats', we mention in brief the observations that were obtained from the archive but were rejected during the analysis due to various reasons. The reasons are summarised therein.

Preliminary studies on hot Jupiters (Jupiter-sized or bigger planets in close-in orbits to their host star with orbital period of P $\leq$ 10 days) or companion brown dwarf hosting stars show increased stellar activity due to tidal interactions (Poppenhaeger, 2022,Ilić et al., 2023). We therefore highlight host stars in the table for context. These stars could have been spun up due to tidal interaction. We mention a few details about these stars as obtained from the NASA Exoplanet Archive below.

GJ 15 A hosts two exoplanets 'GJ 15A b' and 'GJ 15A c' at an orbital distance a= $\approx$ 0.072 AU and a= $\approx$ 5.4 with masses $\approx 0.00953 M_{\rm Jup}$ and $\approx 0.11 M_{\rm Jup}$ (Pinamonti et al., 2018).

BD+61 195 has a confirmed exoplanet 'GI 49 b' with a=0.0905 ± 0.0011 and $\approx 0.0177 M_{\rm Jup}$ (Perger et al., 2019).

A few stars were also found to be hosting exoplanets, however, they were too small or too far away from the host star to be tidally interacting at a relevant level with their host star. These stars are not highlighted

Table 4.1: X-ray Luminosity obtained from the XMM-Newton catalogue DR-11

SpT	component	$\log_{10}$(T) ($\pm$0.1)[K]	L_X ($\times 10^{+27}$)	$\log_{10}(\frac{L_{X1}}{L_{X2}})$ dex	R_X [dex]
F	30 Ari A	6.5	208.867 ± 1.1664	-0.395	-4.863
	30 Ari B	6.6	519.074 ± 1.5459		-4.154
K	TIC 386958859	6.5	4.289 ± 0.7384	-0.568	-4.881
	Gaia DR2 6265476305474324480	6.4	15.852 ± 1.5747		-4.538
K	CD-39 1993	6.4	8.926 ± 0.7369	-0.635	-4.744
	HD 36223	6.4	38.488 ± 1.8281		-4.559
K	61 Cyg A	6.4	1.7 ± 0.0129	0.344	-5.687
	61 Cyg B	6.4	0.77 ± 0.0061		-5.773
K	TIC 407726879	6.5	38.138 ± 6.9579	-0.09	-4.719
	TIC 407726881	6.3	46.895 ± 10.0618		-4.148
K	HD 222863	6.5	2.522 ± 0.6038	0.251	-5.901
	WT 1017	6.9	1.416 ± 0.4365		-5.503
K	G 70-50	6.4	6.942 ± 0.4664	0.299	-4.67
	HD 7895	6.3	3.486 ± 0.4043		-5.674
M	Ross 868	6.4	11.396 ± 0.216	-0.708	-3.603
	Ross 867	6.4	58.167 ± 0.3427		-2.469
M	TIC 436632332	6.2	89.194 ± 4.3308	0.384	-2.253
	TIC 436632331	6.4	36.852 ± 2.4501		-2.543
M	TIC 293303829	6.4	1.716 ± 0.2591	0.127	-4.934
	TIC 293303832	6.5	1.281 ± 0.2712		-5.126
M	GJ 15 B	6.3	0.07 ± 0.0051	-0.777	-5.697
	GJ 15 A	6.3	0.42 ± 0.0109		-5.508
M	Wolf 47	6.4	32.701 ± 0.1821	0.766	-2.597
	BD+61 195	6.4	5.601 ± 0.1247		-4.391
M	Gaia DR2 1608710752684301312	6.4	72.864 ± 4.4282	0.949	-2.313
	Gaia DR2 1608710791338814208	6.4	8.191 ± 1.5035		-3.271
M	Gaia DR2 3074577322667614976	6.4	89.38 ± 1.5477	0.453	-2.605
	Gaia DR2 3074630580262065536	6.4	31.464 ± 1.0764		-2.927
M	Gaia DR2 3507497759677598208	6.4	1.014 ± 0.2392	0.095	-3.696
	Gaia DR2 3507497686662478080	6.5	0.814 ± 0.2024		-5.268
M	Gaia DR2 1212501604470775168	6.3	14.656 ± 3.5668	0.273	-3.865
	Gaia DR 1212501535751298176	6.6	7.812 ± 1.6326		-3.294

Table 4.2: X-ray Luminosity obtained from the Chandra X-ray observatory

SpT	component	instrument	obs no.	detect	$\log_{10}$(T)($\pm$ 0.1)[K]	L_X ($\times 10^{+27}$[erg/s]	$\log_{10}(\frac{L_{X1}}{L_{X2}})$ dex	R_X [dex]
F	HD 48767	acisS	23353	yes	6.9	69.506 ± 3.1047	0.342	-5.184
	HD 48766			yes	7.0	31.65 ± 0.6827		-5.324
G	49 Ser A	acisS	21190	yes	6.4	$2.546^{+3.7711}_{-1.6406}$	0.477	-5.948
	49 Ser B			yes	6.4	$0.85^{+1.6364}_{-0.3666}$		-6.404
G	HD 103431	acisS	21192	yes	6.7	$1.935^{+2.8025}_{-1.2626}$	-0.247	-6.114
	HD 103432			yes	6.4	$3.41^{+5.1012}_{-2.1388}$		-5.929
G	HD 201796A	acisS	21193	yes	6.7	80.201 ± 4.8563	-0.037	-4.628
	HD 201796B			yes	6.7	87.33 ± 2.5298		-4.631
K	HD 7895	acisS	4963	yes	6.7	1.311 ± 0.1197	0.123	-5.394
	G 70-50			yes	6.7	0.99 ± 0.0763		-6.222
K	CD 39 1993	acisI	15177	yes	6.7	$3.928^{+4.5765}_{-3.3435}$	-0.784	-5.1
	HD 36223			yes	6.6	23.86 ± 0.7007		-4.766
K	CD 39 1993	acisI	15658	yes	6.6	7.585 ± 0.4376	-0.489	-4.814
	HD 36223			yes	6.6	23.37 ± 0.3634		-4.775
K	HD 154712	acisS	21189	yes	6.4	$1.809^{+2.7916}_{-1.0661}$	-0.249	-5.774
	HD 154712B			yes	6.4	$3.21^{+4.4401}_{-2.2165}$		-5.026
K	HD 146413B	acisS	21191	yes	6.8	$6.532^{+7.5977}_{-5.571}$	0.31	-5.07
	HD 146413A			yes	6.4	$3.2^{+4.5113}_{-2.1806}$		-5.275
K	Cyg 61A	HRC	13651	yes	6.4	1.07 ± 0.02348	-0.03	-5.629
	Cyg 61B			yes	6.4	1.16 ± 0.02363		-5.855

Table 4.3: Continued table 4.2

SpT	component	instrument	obs no.	detect	$\log_{10}$(T)($\pm$0.1)[K]	L$_X$ ($\times 10^{+27}$[erg/s])	$\log_{10}(\frac{L_{X1}}{L_{X2}})$ dex	R$_X$ [dex]
M	Ross 868	acisI	1453	yes	6.7	22.859 ± 0.4956	0.148	-3.3
	Ross 867			yes	6.6	16.27 ± 0.2621		-3.023
M	Ross 868	acisI	3224	yes	6.7	21.174 ± 0.2671	0.269	-3.333
	Ross 867			yes	6.7	11.39 ± 0.1076		-3.178
M	Ross 868	acisI	4361	yes	6.7	10.821 ± 0.1935	-0.003	-3.625
	Ross 867			yes	6.7	10.9 ± 0.1055		-3.196
M	VB 8	acisS	615	yes	6.5	0.157 ± 0.0151	0.737	-5.376
	Wolf 629			yes	6.6	$0.03^{+0.036}_{-0.0224}$		-4.97
M	BD 19 5116B	acisS	8453	yes	6.6	$7.591^{+0.2859}_{-0.2859}$	-0.649	-3.348
	BD +19 5116A			yes	6.6	33.8 ± 0.3676		-3.129
M	BD +19 5116B	acisS	8484	yes	6.6	5.865 ± 0.4128	-0.86	-3.46
	BD +19 5116A			yes	6.7	42.47 ± 0.6303		-3.029
M	BD +19 5116B	acisS	8485	yes	6.6	12.63 ± 0.351	-0.436	-3.127
	BD +19 5116A			yes	6.6	34.5 ± 0.3716		-3.12
M	BD +19 5116B	acisS	8486	yes	6.6	6.609 ± 0.2774	-0.763	-3.409
	BD +19 5116A			yes	6.6	38.33 ± 0.4129		-3.074
M	G 104 35	acisS	17729	yes	6.6	$0.294^{+0.4228}_{-0.1948}$	-0.34	-5.723
	G 104 36			yes	6.5	$0.64^{+0.8518}_{-0.4706}$		-5.196
M	GJ 15B	acisS	20617	yes	6.6	0.097 ± 0.0102	-0.258	-5.558
	GJ 15A			yes	6.6	0.17 ± 0.0093		-5.889
M	LP415-19	acisS	23406	yes	7.0	23.842 ± 2.0594	0.68	-2.171
	TIC 17294130			no	(6.4)	≤ 4.98		≤ -2.715
M	LP415-19	acisS	24385	yes	6.6	$3.351^{+4.5072}_{-2.4589}$	0.171	-3.024
	TIC 17294130			no	(6.4)	≤ 2.26		≤ -3.059
M	LP415-19	acisS	24386	yes	7.0	$2.627^{+3.3208}_{-2.08}$	0.038	-3.129
	TIC 17294130			no	(6.4)	≤ 2.41		≤ -3.031
M	LP415-19	acisS	24387	yes	6.6	$3.42^{+4.7724}_{-2.3992}$	0.039	-3.015
	TIC 17294130			no	(6.4)	≤ 3.13		≤ -2.918
M	LP415-19	acisS	24388	yes	6.5	$14.152^{+17.1383}_{-11.587}$	0.655	-2.398
	TIC 17294130			no	(6.4)	≤ 3.13		≤ -2.918
M	LP415-19	acisS	24389	yes	6.5	$9.983^{+12.9633}_{-7.5127}$	0.371	-2.55
	TIC 17294130			no	(6.4)	≤ 4.25		≤ -2.785
M	LP415-19	acisS	24390	yes	6.5	$5.265^{+6.9622}_{-3.5596}$	0.014	-2.827
	TIC 17294130			no	(6.4)	≤ 5.1		≤ -2.705
M	LP415-19	acisS	24868	yes	7.0	$1.612^{+2.3062}_{-1.0861}$	-0.663	-3.341
	TIC 17294130			no	(6.4)	≤ 7.43		≤ -2.542
M	LP415-19	acisS	24871	yes	6.5	$8.328^{+10.9663}_{-6.0168}$	0.301	-2.628
	TIC 17294130			no	(6.4)	≤ 4.16		≤ -2.794
M	LP415-19	acisS	24878	yes	6.6	$5.961^{+7.5428}_{-4.7132}$	0.129	-2.774
	TIC 17294130			no	(6.4)	≤ 4.43		≤ -2.766
M	LP415-19	acisS	24879	yes	6.8	$4.318^{+6.1608}_{-2.9425}$	-0.16	-2.914
	TIC 17294130			no	(6.4)	≤ 6.24		≤ -2.618
M	LP415-19	acisS	24880	yes	6.7	$4.432^{+5.8937}_{-3.2992}$	0.098	-2.902
	TIC 17294130			no	(6.4)	≤ 3.54		≤ -2.865
M	TIC 149506100	acisS	24991	yes	7.0	$4.945^{+5.6339}_{-4.4093}$	-0.845	-3.914
	TIC 149506101			yes	6.9	$34.63^{+0.6603}_{-0.6603}$		-3.124
M	TIC 149506100	acisS	24503	yes	7.0	$2.739^{+0.3303}_{-0.3303}$	-0.845	-4.171
	TIC 149506101			yes	7.0	$19.18^{+0.251}_{-0.251}$		-3.38
M	GJ 1183A	acisS	24504	yes	6.9	$17.335^{+0.837}_{-0.837}$	0.245	-2.959
	GJ 1183B			yes	7.0	$9.85^{+0.1681}_{-0.1681}$		-3.196
M	GJ 1183A	acisS	24899	yes	6.8	$16.658^{+0.9187}_{-0.9187}$	0.285	-2.976
	GJ 1183B			yes	6.8	$8.63^{+0.2387}_{-0.2387}$		-3.254
M	G 162-44	acisS	24677	yes	(6.4)	$1.021^{+2.5541}_{-0.2736}$	-1.188	-4.575
	LP 729 55			no	(6.4)	≤ 15.75		≤ -2.765
M	TIC 422692635	acisS	23394	yes	6.9	$180.966^{+7.6921}_{-7.6921}$	-0.411	-2.424
	TIC 422692632			yes	7.0	$465.91^{+3.5435}_{-3.5435}$		-2.053
M	LP920 61 A	acisI	13585	no	(6.4)	≤ 2.178	0.0	≤ -4.308
	LP920 61 B			no	(6.4)	≤ 2.18		≤ -4.223
M	LP920 61 A	acisI	13588	no	(6.4)	≤ 2.178	0.0	≤ -4.308
	LP920 61 B			no	(6.4)	≤ 2.18		≤ -4.223
M	SCR J0602-3952B	acisI	3450	no	(6.4)	≤ 0.637	0.0	≤ -4.679
	SCR J0602-3952A			no	(6.4)	≤ 0.64		≤ -4.822
M	SCR J0602-3952B	acisI	3202	no	(6.4)	≤ 0.286	-0.0	≤ -5.027
	SCR J0602-3952A			no	(6.4)	≤ 0.29		≤ -5.171

Table 4.4: Continued table 4.3

SpT	component	instrument	obs no.	detect	$\log_{10}$(T)($\pm$0.1) [K]	L_X ($\times 10^{+27}$[erg/s])	$\log_{10}(\frac{L_{X1}}{L_{X2}})$ dex	R_X [dex]
M	G272 61B	HRC	1880	yes	6.6	4.181 ± 0.0963	0.35	-2.945
	G272 61A			yes	6.6	1.89 ± 0.3379		-3.525
M	G272 61B	HRC	22344	yes	6.7	2.186 ± 0.3338	0.14	-3.227
	G272 61A			yes	6.6	1.58 ± 0.0429		-3.602
M	G272 61B	HRC	22876	yes	6.7	2.438 ± 0.0915	0.11	-3.179
	G272 61A			yes	6.6	1.89 ± 0.0930		-3.523
M	G 236-2	HRC	6655	yes	6.8	9.235 ± 0.3225	-0.09	-3.812
	G 236-1			yes	6.8	11.48 ± 0.3591		-3.923

in the table but are mentioned below.

30 Ari B has a confirmed Jupiter-sized exoplanet or a Brown dwarf "30 Ari B b" with 9 $M_{\rm Jup}$ and a= 0.995$\pm$0.012 AU (Guenther et al., 2009)

G 162-44 has two exoplanets b and c. b is a super-earth with $\approx 0.0077 M_{\rm Jup}$ and c is a super Neptune with $\approx 0.022 M_{\rm Jup}$ (Luque and Pallé, 2022).

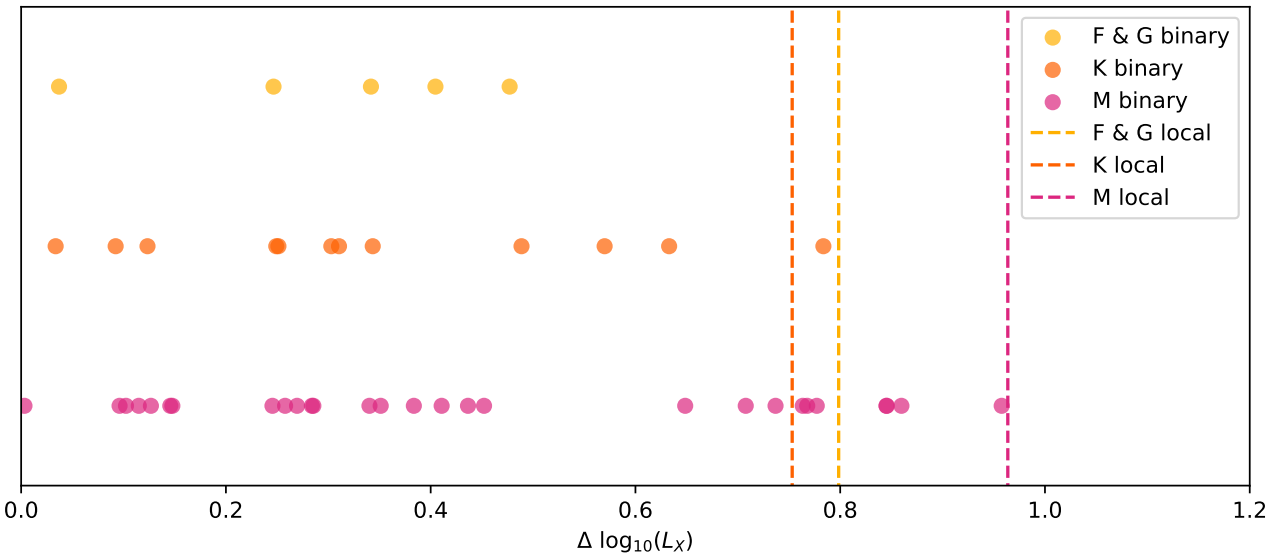

Figure 4.1: Scatter of X-ray luminosity in solar local neighbourhood (NEXXUS) vs co-eval neighbourhood stars.

Fig. 4.1 shows us the spread of $\Delta \log L_X$ between coeval binaries based on their spectral type. We merged our F and G stars into one group "F & G" as there were not enough stars in this spectral type to make a strong inference. However, F-type stars were paired only with other F stars and likewise for G stars. The plot consists of only binary pairs with both stars detected by the bright and the faint source pipeline.

Initial inspection shows us that there is more scatter in magnetic activity between M dwarfs when compared to K-type stars. A comparison sample from the NEXXUS database (Schmitt and Liefke, 2004) is generated by using a random pair generator that selects two stars in a pseudo-random fashion and pairs them up. We pretend that these pairs of stars are a binary and find the $\Delta \log L_X$. Since the NEXXUS

database consists of volume-limited field stars within $\sim$ 10pc of the Sun, it can be assumed that they were formed around the same time and therefore would be a few Gyrs old, but not drastically young or old compared to the Sun. $\Delta \log L_X$ of the NEXXUS pairs would therefore represent the scatter of activity in the solar neighbourhood. The scatter calculated from this sample is represented as a dashed line in fig. 4.1

Table 4.5: Mean and standard deviation of the scatter in coeval

SpT	$\mu_{\text{co-eval}}$ [dex]	$\sigma_{\text{co-eval}}$ [dex]	μ_{NEXXUS} [dex]
F&G	0.30	0.15	0.79
K	0.35	0.22	0.75
M	0.44	0.28	0.96

Table. 4.5 shows us how much scatter we observe in the coeval sample vs that of the NEXXUS database. We can see that the NEXXUS stars have a very high scatter compared to that of co-eval stars, in all cases it lies outside the 1σ cut-off. This confirms that although these stars lie in the solar neighbourhood, they do not represent co-eval stars accurately. Any study therefore using the solar neighbourhood stars would have to take into account that these stars are not a good representation of co-eval stars.

CHAPTER 5

Discussion

To study the natural scatter of magnetic activity in cool stars, it is essential to look for coeval stars. Coeval stars in binary systems show us the evolutionary scatter of activity, i.e. the range of scatter in activity observed as a star evolves through the Main sequence. However, it is crucial to compare similar mass stars to each other. This is because more massive stars such as F-type stars have completely different spin-down timescales when compared to M dwarfs which stay in the saturated regime for a very long time.

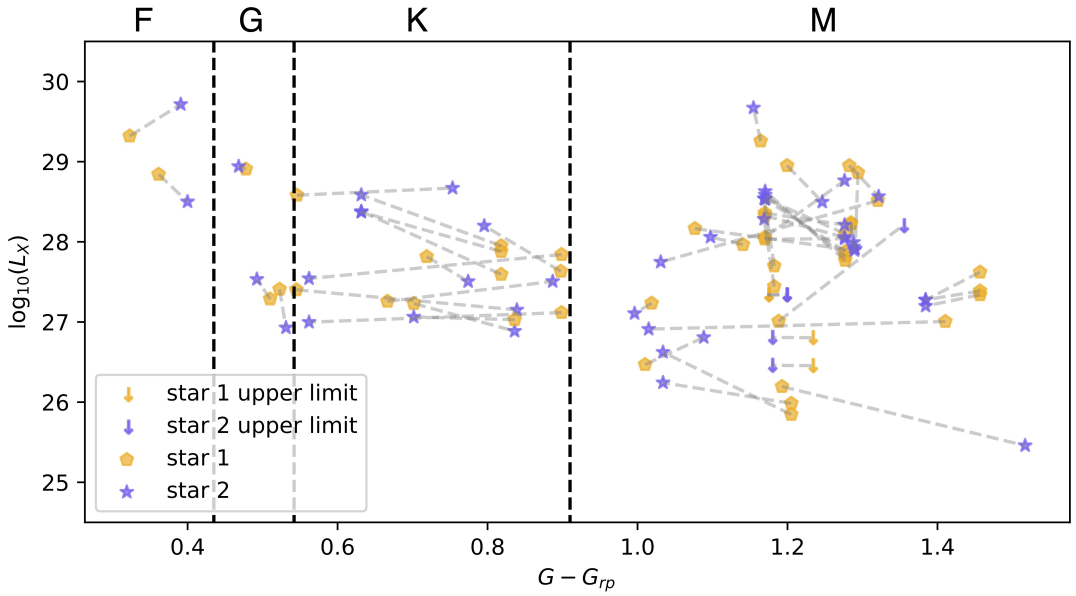

Figure 5.1: $\log_{10} L_X$ vs G-G_{rp} X-ray luminosity with binary pairs

In our study, we do not explicitly label the binary components as primary or secondary as other studies of binary stars do. We do this as we have a few systems with the same spectral subtypes (almost the same mass), making it impossible to distinguish one star as heavier from the other. By avoiding this nomenclature we avoid the conflict of choosing a primary and a secondary in similar mass systems, however, we also introduce a problem. Since the range of masses between the biggest and the smallest G star (1.06-0.90 $M_\odot$)[1] is very different from the biggest and smallest M dwarfs (0.57-0.078 $M_\odot$), we do have M dwarf binaries in our sample with very different masses even though they are from the same spectral type. We

[1] Estimates from https://www.pas.rochester.edu/~emamajek/EEM_dwarf_UBVIJHK_colors_Teff.txt

solve this issue by using the colour G-G_{rp} as an indicator of the difference in mass. Stars which have very similar colour G-G_{rp} will have a very small value for ΔG-G_{rp}

Fig. 5.1 shows the individual components of the binaries connected to their counterparts with a dashed line. In this plot, we have also indicated pairs that were not detected by our faint source pipeline with an upper limit. Since the pairs are coeval and of the same spectral type, we would expect the grey lines to be either very short with a high gradient or longer but parallel to the x-axis. A short line with a high gradient would indicate a very similar colour but with slightly different x-ray luminosities. We expect this as stars have temporal variations in their stellar activity which fluctuates their X-ray emission. A longer line parallel to the x-axis would indicate different colour, but similar activity. We can see this in the bluer stars (left of the plot), but we do see a lot of scatter in $\log_{10}L_X$ in the redder regime dominated by M dwarfs. i.e. Long dashed lines with high gradients.

This scatter observed specifically in M dwarfs is peculiar as it indicates stars which are similar in colour, but have very different X-ray emissions.

Fig: 5.2 uses R_X instead of x-ray luminosity. In Chapter 1 we discussed the benefits of R_X to study x-ray emission of the corona. In our study, we can see that M dwarf pairs with high scatter are most likely to be in or near the saturation regime ($R_X = -3.13 \pm 0.12$ (Wright et al., 2018)). This scatter is stronger when compared to that seen in F, G and K-type stars. Unfortunately, due to a lack of data (5 systems), we cannot conclude that this is the general case of F and G-type stars. However it can be seen that all K-type stars behave similarly to their co-eval counterpart.

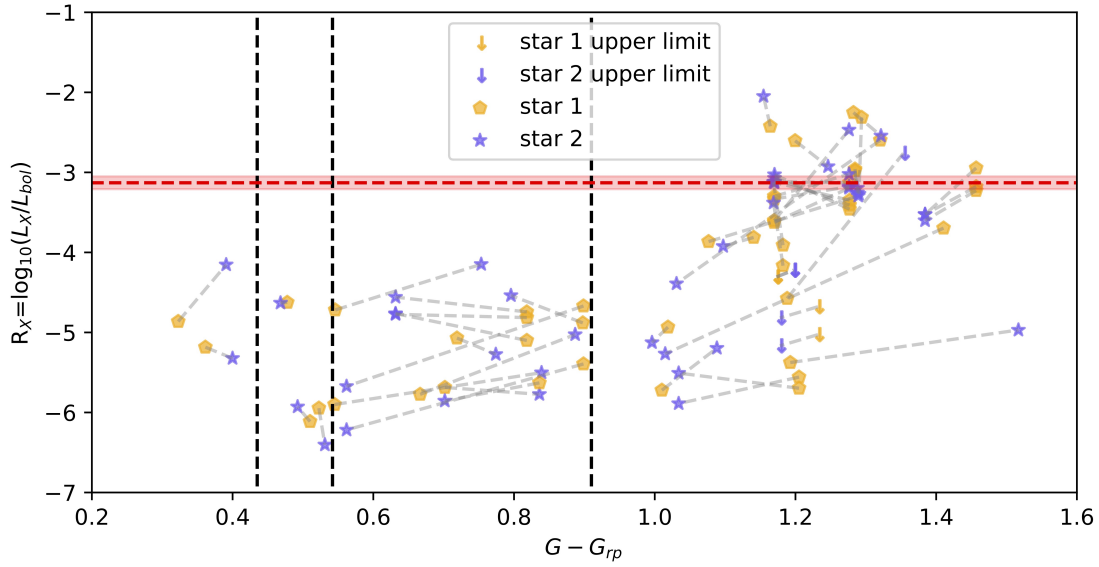

Figure 5.2: R_X vs G-G_{rp} shows us that the F, G and K type stars are in the unsaturated regime, while many M-dwarf stars are still in the saturation regime of $R_X = \sim -3.13$.

Fig 5.3 shows us the difference in colour between the pairs vs the difference in activity. It can be seen that the difference in colour between the same spectral type sample affects the difference in luminosity

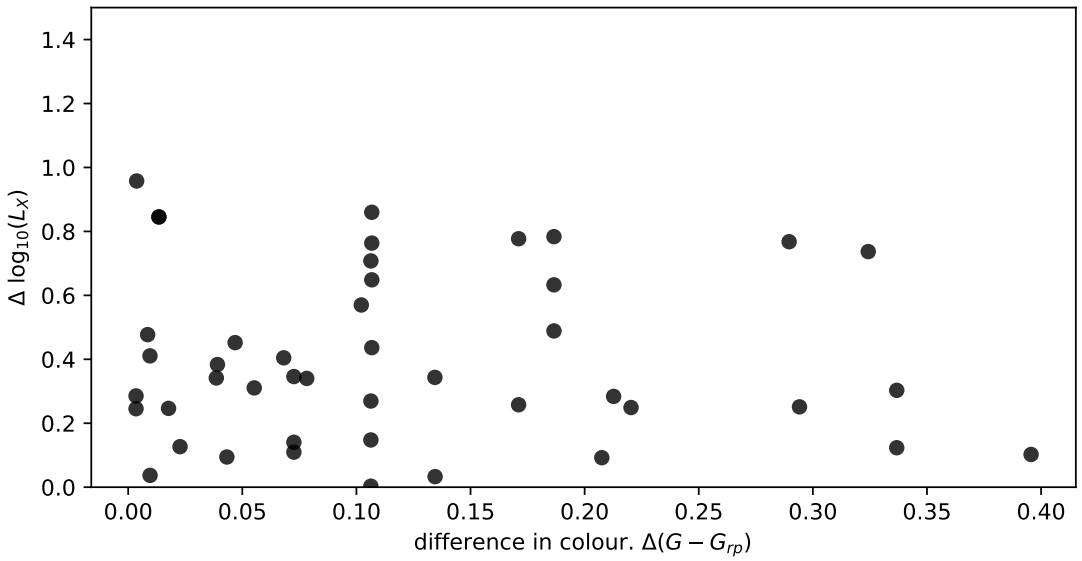

Figure 5.3: Difference in colour between the components vs difference in x-ray luminosity shows us the stellar subtype dependence on x-ray luminosity. The plot however shows us that this dependence does not exist.

negligibly we do not see any correlation in this data. This tells us that although there are major observable differences when comparing F-type stars to K or M-type stars, we should not expect to see these differences when we observe a K1V vs K8V as any intrinsic differences caused by the subspectral type differences are most likely to be overrun by the natural intrinsic scatter in the activity of the star.

Although we see no correlation between the scatter in activity vs the colour difference, we do see that the difference in activity is constrained to be below $\Delta \log_{10} L_X \approx 1.0$ in all the systems, with a mean μ = 0.426 dex and standard deviation σ= 0.31. This result is significant as this quantifies the expected absolute scatter of activity to be below 1.0 dex. This result can be used for studies that model the stellar dynamo. Specifically studies that attempt to solve the open question of the mechanism that heats the corona. The result can also be used to study exoplanet atmospheric evaporation caused due to stellar activity as this sets the upper and lower limits in the evolution of X-ray and UV emission.

Converting fig. 4.1 into a histogram (fig. 5.4) shows us that there is a gap in the scatter of M dwarf activity that is not observed in K-type systems. This gap represents a lack of stars with scatter of $|\log_{10} L_{X,star1} - \log L_{X,star2}| \sim 0.4$ - 0.5 dex. Fig: 5.2 shows our comparison sample of randomly selected NEXXUS pairs. Here we do not see the gap in scatter. A similar gap is seen in F and G-type stars in our sample, but again, this subset consists of only 5 systems and therefore could be an outcome of small number statistics.

One reason for the gap could be the difference in mission requirements of the space telescopes. Our sample consists of a mix of pointed and serendipitous observations, while the NEXXUS database is mainly a collection of survey observations from the survey class telescope ROSAT. Pointed observations have very different observation goals than a survey mission. The stars observed in pointed observations could

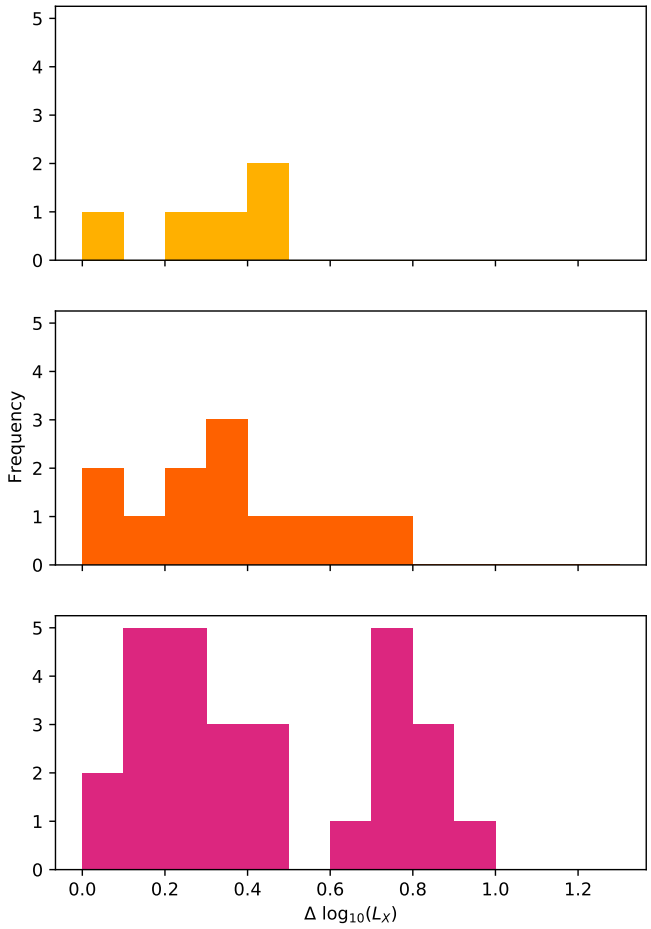

Figure 5.4: Scatter of x-ray luminosity in the solar neighbourhood represented as a histogram. F/G pairs in yellow, K pairs in orange and M pairs in pink

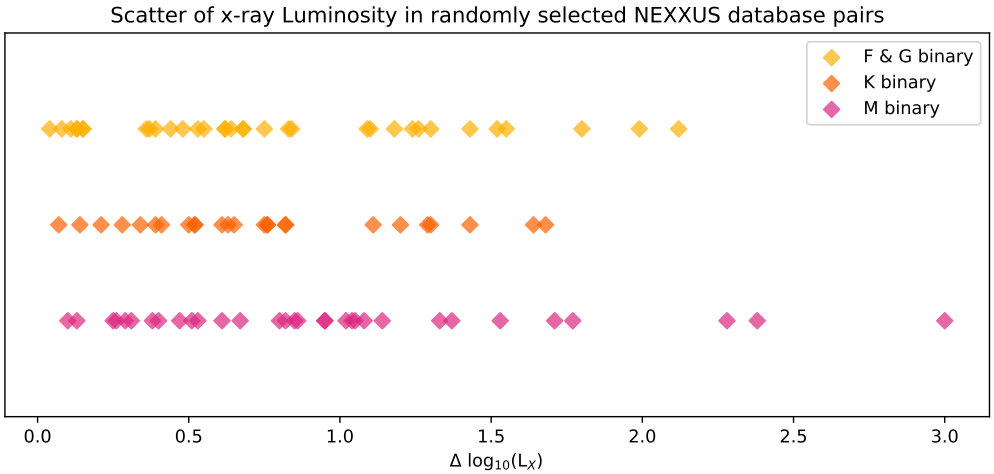

Figure 5.5: Scatter observed in randomised NEXXUS star pairs

have had certain unique characteristics that made them interesting for a study and therefore were accepted by the committees that assigned observing times for proposals. Two very similar M dwarfs for example would be a good test case to study the predictability of stellar activity, while two very similar stars with very different activity go against predicted evolutionary behaviour. Both cases could therefore attract more observation time, causing a bias in our data set. Pointed observations also have much larger exposure times, meanwhile, survey-class telescopes scan the sky in short exposure times and therefore represent a short snapshot of stellar activity.

Another reason could be that there is a bimodality in X-ray luminosity where the difference of ∼0.5 dex is a 'step'. This bimodality in luminosity seen in M dwarfs could be a signature of natural scatter in activity, where the X-ray emission of a star follows a "two-mode" phase of high and low activity. Since coronal emission is caused due to magnetic activity, the cause of this observed step should be directly related to the stellar dynamo of M dwarfs.

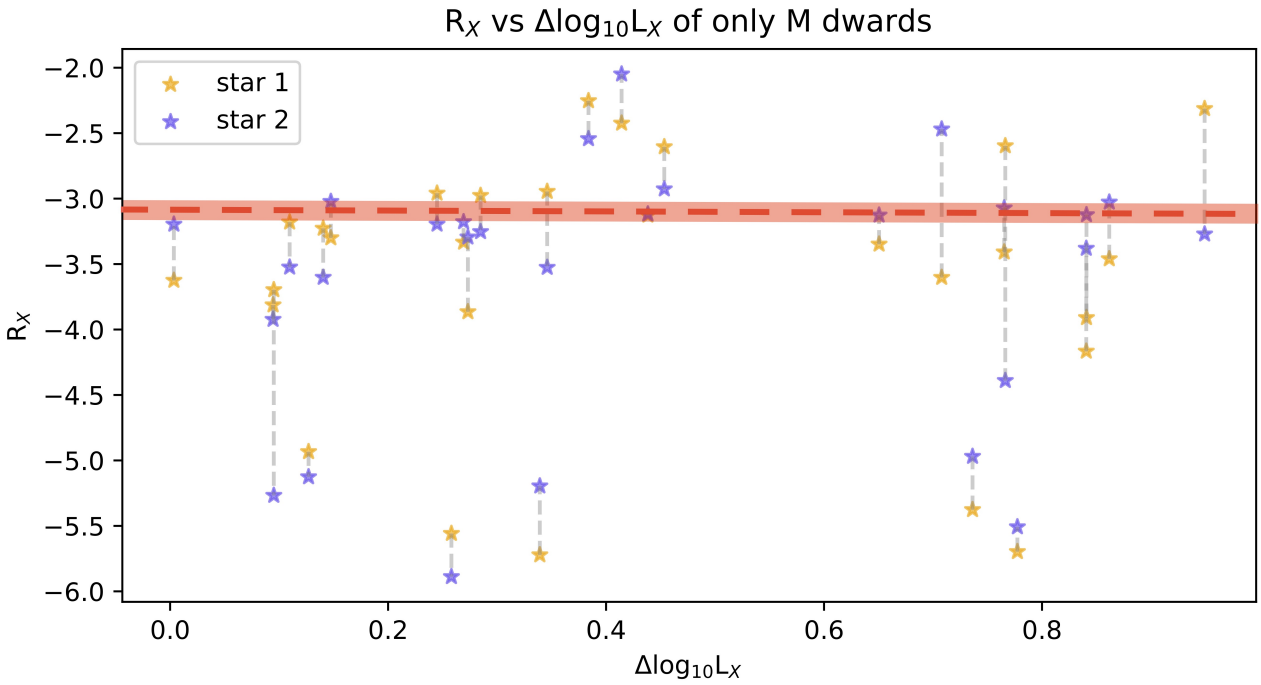

Figure 5.6: Scatter observed in M dwarf pairs vs R_X values. We use the same $\Delta\log_{10}L_X$ for both stars. Saturation regime lies above the red dashed line.

Fig. 5.6 shows the scatter observed only in M dwarf pairs vs the R_X values. We can see the discontinuity between $\sim 0.5-0.65$ dex, However, we can also see that most stars are in the saturation regime with $\Delta\log_{10}$ L_X $\sim$ 0.0 - 0.5 dex and between 0.65 - 1.0 dex. Only two M dwarf pairs have high scatter and lie in the unsaturation regime ($R_X \leq -5.0$). Since the saturation regime has multiple stars, the observed discontinuity is a feature that appears to exist in M dwarf coeval stars in the saturation regime.

Activity-rotation study of the NGC 6811 (Curtis et al., 2019) suggests that K dwarfs could go through a temporary phase of stalled breaking. This stalled breaking causes older K dwarfs (1Gyr) to stay at higher rotation periods for a longer time than K dwarfs in younger clusters. Indicative studies (Magaudda et al., 2020) on fully convective M dwarfs in the saturation and non-saturation regime show a similar phe-

nomenon where there are two sparsely occupied L_X zones $\sim$ 28.2 erg/s and $\sim$ 27.2 erg/s termed as the "X-ray gap" (fig. 5.7). However, 'step' is not observed in our randomised NEXXUS M dwarfs. Additionally, the observation of the "x-ray gap" was initially observed in K dwarfs, we also see no indication of this gap in our K dwarf sample. More observations of stars in this regime could help shed some light on the legitimacy of this discontinuity.

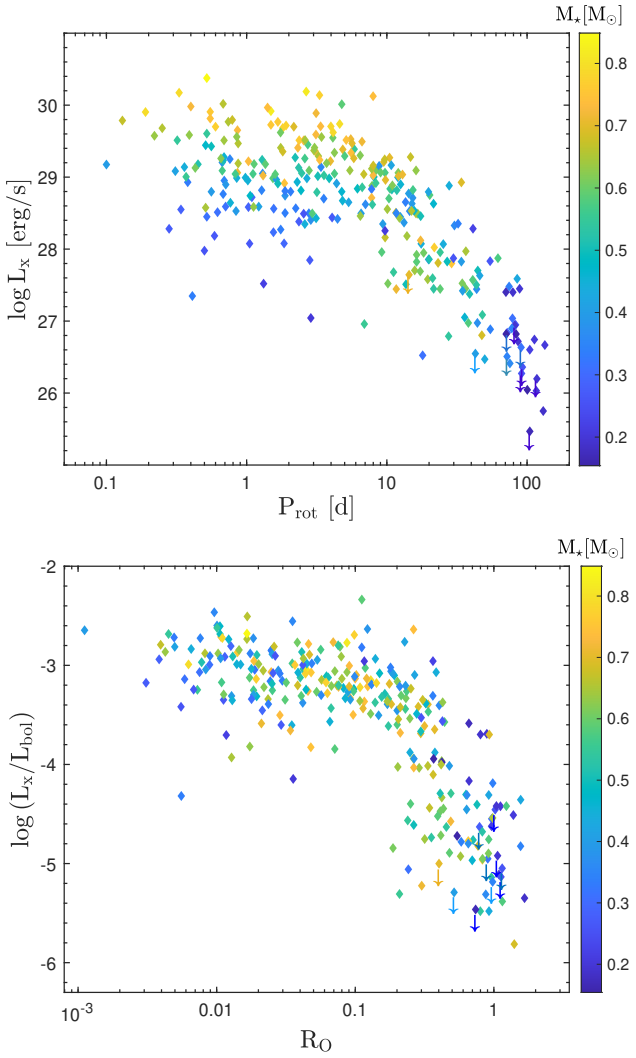

Figure 5.7: X-ray gap observed in fully convective M dwarfs using Chandra and XMM-Newton. Image source: Magaudda et al., 2020

5.1 Star-planet interaction

Our study is specifically also useful for identifying star-planet interaction (SPI). Studies that attempt to prove SPI face a glaring issue, that is how do we know that the activity of a host star is "increased" due to an exoplanet or due to its intrinsic temporal variations? Additionally, how do we separate the natural coeval evolution from that of SPI caused increase or decrease in activity? A solution proposed for this is to use a binary system (Poppenhaeger and Wolk, 2014). This ensures the co-eval nature of the stars and therefore the other component (non-hosting component) of the system can be used as a control. This

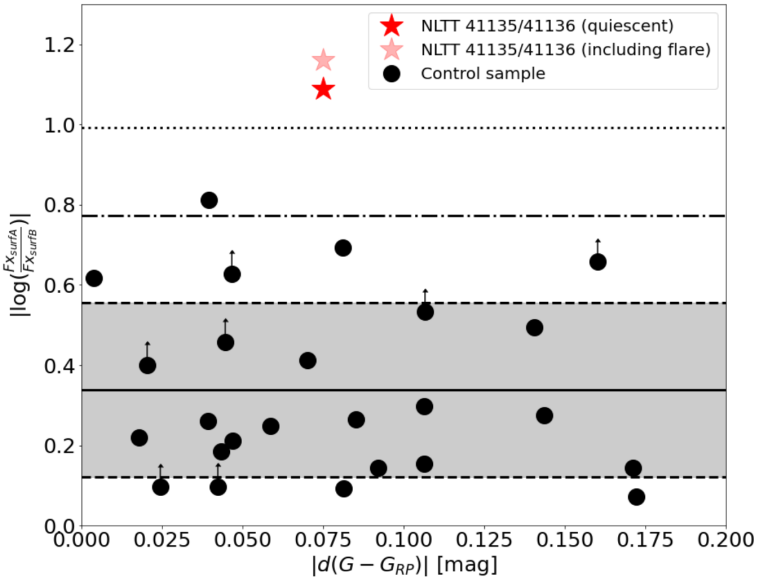

Figure 5.8: Difference in surface flux plotted against difference in colour shows NLTT 41135 with increased surface flux of more than 3σ due to a tidally interacting brown dwarf. Upper limits have been denoted by an arrow. Image source: Ilić et al., 2023

control helps identify the additional SPI induced increase of activity over the evolutionary intrinsic scatter.

In the previous section, we described how we found no visible correlation in subtypes with the scatter of activity. We see a μ = 0.426 dex with a σ= 0.31 dex in the scatter of activity. This constrained scatter was used to find the first evidence of tidally induced activity in an M dwarf star by a brown dwarf. I contributed to this study by analysing the M-dwarf stars in the control sample that were observed using the Chandra ACIS-I and ACIS-S instruments. This was done using the pipeline we described for bright and weak sources.

The NLTT 41135/41136 M dwarf system has a brown dwarf orbiting NLTT 41135 in a close orbit. This proximity to the host star leads to tidal interaction between the brown dwarf and the star. The X-ray emission was then benchmarked with its companion M dwarf NLTT 41136. The difference of surface flux of activity between the pairs was $\left|\log(\mathrm{F}_{X,A}/\mathrm{F}_{X,B})\right| = 1.1 \pm 0.2$, which is more than the comparison sample of 25 wide M-dwarf binaries with $\left|\log(\mathrm{F}_{X,A}/\mathrm{F}_{X,B})\right| = 0.34 \pm 0.22$(fig. 5.8) , this is more than 3σ detection of tidal SPI (Ilić et al., 2023).

5.2 Variability in stars with multiple observations

Two systems LP 415-19/TIC17294130 and BD +19 5116B/ A were observed more than 3 times. In fig: 5.9 and 5.10, we plot them with their time of observation. This shows us how the stars vary in time with respect to each other.

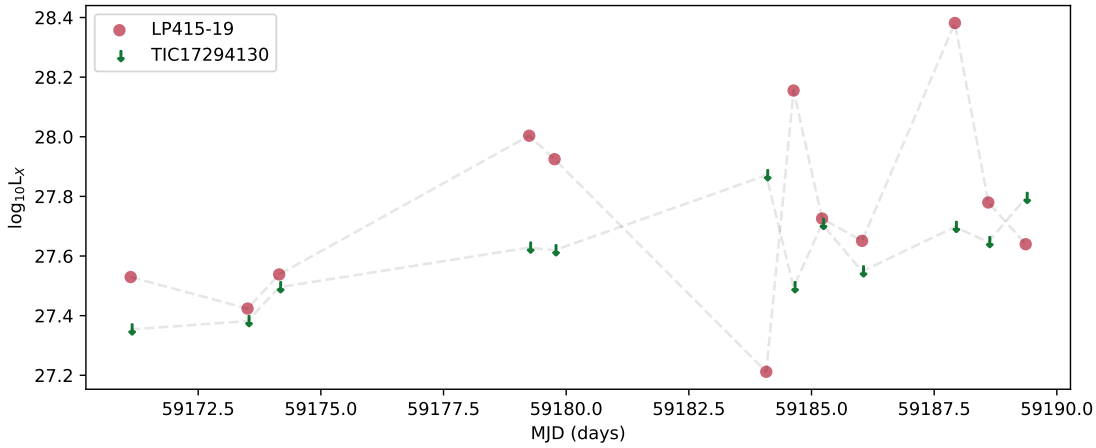

Figure 5.9: Variability observed in LP415-19 and TIC17294130 through multiple observations.

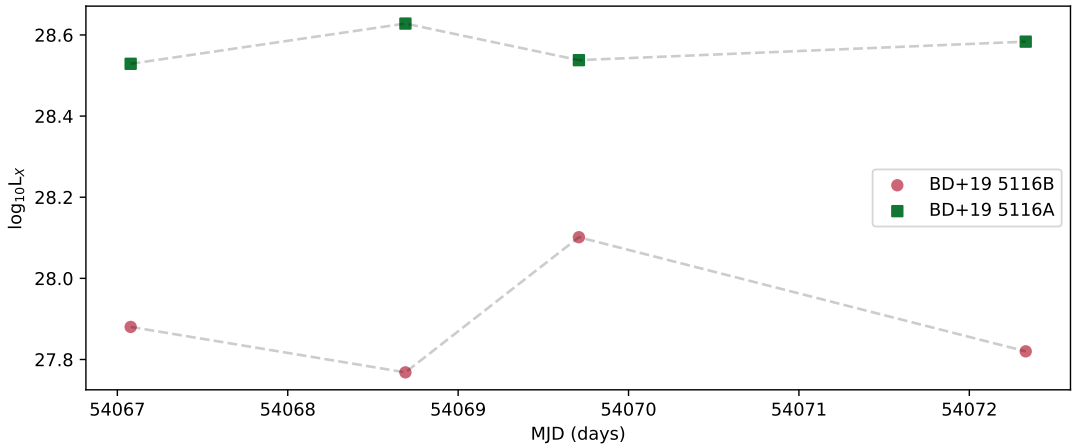

Figure 5.10: Variability observed in BD +19 5116B and A

LP 415-19/TIC17294130 (star 1/star 2) has no detection of star 2, however, we do see that the upper limit in two observations, the 6th ($\sim$ 59184 MJD) and the last ($\sim$ 59189 MJD) are more than that of the detected component. This happens because, there are two detections of star 1, which have a high hardness ratio and $\log_{10}$T=7.0. Meanwhile, star 2 remains undetected in all observations and has an upper limit of 4 counts, with a median count of 0. Since the faint source pipeline estimates the upper limits and assumes a $\log_{10}$T of 6.47, we get high estimated luminosity values for an undetected source. In fig.5.11a, we can see how the conversion factor is strongly dependent on the

estimated temperature of the star.

BD +19 5116B/ A shows a scatter of $\sim$ 0.677 dex consistently. The A and B component was found to have a luminosity of the order of $\sim$ 28.56 erg/s and $\sim$ 27.89 erg/s. This is very close to the previously published value of $\sim$ 28.71 erg/s and $\sim$ 27.89 erg/s (Liefke et al., 2008) from the same instrument. Small differences in the luminosity values come from the different methods of calculating the luminosity. We use the hardness ratio to determine the estimated flux while their approach was based on using the spectra to estimate the temperature. While the spectra-based approach can give us more reliable temperature estimates, it is time-consuming and requires a considerably higher proportion of photons. The hardness ratio measurements do not depend on the usage of the spectrograph and also work for observations with lesser counts. This is why we use the hardness ratio-based approach in our study.

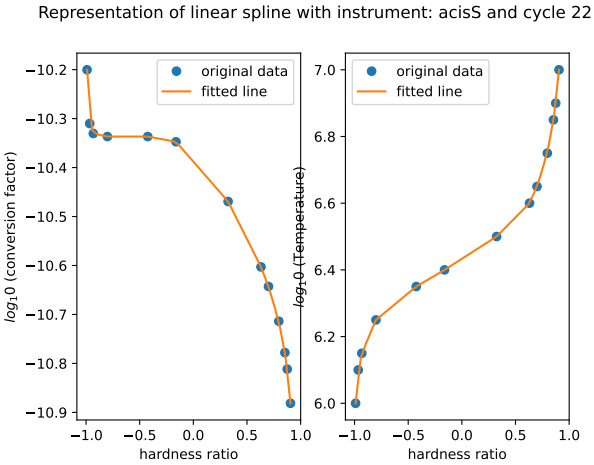

(a) Conversion factor for LP 415-19/TIC17294130

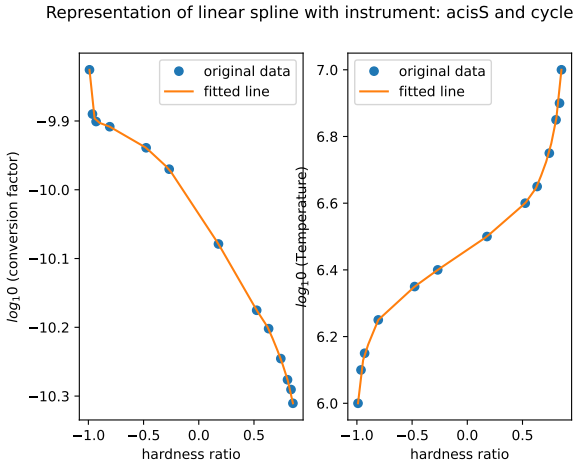

(b) Conversion factor for BD +19 5116B/A.

Figure 5.11

CHAPTER 6

Future prospects

Studies of binaries give us snapshots of the evolutionary scatter in activity, they however do not tell us in which phase of evolution this scatter occurs. i.e.: We do not know the ages of the stars, we only know that they are coeval. This problem will however be solved in the near future by a few additional steps. As gyrochronology continues to be calibrated for field stars, its usage in binary systems will become increasingly prominent. A recent study (Gruner et al., 2023) with 236 cool Main sequence wide binary systems shows that gyrochronology is still effective in estimating the age of these systems. The study also concludes that metallicity has very little effect on age estimation using gyrochronology. This step is essential as we can now start calibrating the X-ray emission of wide binaries to their respective ages, therefore future studies of age vs activity for X-ray targets will no longer be restricted only to nearby clusters.

As shown in Chapter 2, Fig. 2.3, there are up to 10^3 binary systems of the same spectral type from the solar neighbourhood that can be studied in future studies. Our sample consisted of only 34 unique systems. A survey-class X-ray space mission such as the eROSITA could offer us a plethora of stars to study. A survey telescope has low exposure times for each image. This means that bright active sources would be easily detected. Therefore, it would be ideal to shed some light to explain the X-ray discontinuity. A survey would also offer a statistically significant sample to study.

We would also like to do this study in terms of mixed binary systems since our study showed that subspectral type differences are saturated due to the intrinsic scatter, we would like to also see if F and G-type stars can be clubbed together. Due to the lack of observable F and G pairs ($\sim$ 18 F and $\sim$ 18 G), a combination of F and G type stars as a binary could offer us a bigger sample, while not being very different in terms of mass. It would also remove the artificial binning that we introduce in the sample by considering the same spectral type stars. A binary system with K9 and M1 spectral subtypes would be very close in mass but would have been rejected in our study since they are technically different spectral types. A future study could implement only differences in colour as criteria for binary selection.

Bibliography

Bailer-Jones, C. A. L., Rybizki, J., Fouesneau, M., Mantelet, G., & Andrae, R. (2018). Estimating distance from parallaxes. IV. distances to 1.33 billion stars in igaia/i data release 2. *The Astronomical Journal*, *156*(2), 58. https://doi.org/10.3847/1538-3881/aacb21

Barnes, S. A. (2003). On the Rotational Evolution of Solar- and Late-Type Stars, Its Magnetic Origins, and the Possibility of Stellar Gyrochronology., *586*(1), 464–479. https://doi.org/10.1086/367639

Brinkman, A. C., Gunsing, C. J. T., Kaastra, J. S., van der Meer, R. L. J., Mewe, R., Paerels, F., Raassen, A. J. J., van Rooijen, J. J., Bräuninger, H., Burkert, W., Burwitz, V., Hartner, G., Predehl, P., Ness, J. .-., Schmitt, J. H. M. M., Drake, J. J., Johnson, O., Juda, M., Kashyap, V., … Wargelin, B. J. (2000). First Light Measurements of Capella with the Low-Energy Transmission Grating Spectrometer aboard the Chandra X-Ray Observatory., *530*(2), L111–L114. https://doi.org/10.1086/312504

Buzasi, D., Lezcano, A., & Preston, H. L. (2016). Rotation, activity, and stellar obliquities in a large uniform sample of Kepler solar analogs. *Journal of Space Weather and Space Climate*, *6*, Article A38, A38. https://doi.org/10.1051/swsc/2016033

Caramazza, M., Stelzer, B., Magaudda, E., Raetz, S., Güdel, M., Orlando, S., & Poppenhäger, K. (2023). Complete X-ray census of M dwarfs in the solar neighborhood. I. GJ 745 AB: Coronal-hole stars in the 10 pc sample., *676*, Article A14, A14. https://doi.org/10.1051/0004-6361/202346470

Chabrier, G., & Küker, M. (2006). Large-scale $\alpha\hat{2}$-dynamo in low-mass stars and brown dwarfs., *446*(3), 1027–1037. https://doi.org/10.1051/0004-6361:20042475

Chahal, D., Kamath, D., de Grijs, R., Ventura, P., & Chen, X. (2023). Unravelling the period gap using LAMOST chromospheric activity indices., *525*(3), 4026–4041. https://doi.org/10.1093/mnras/stad2521

Cuntz, M., Saar, S. H., & Musielak, Z. E. (2000). On Stellar Activity Enhancement Due to Interactions with Extrasolar Giant Planets., *533*(2), L151–L154. https://doi.org/10.1086/312609

Curtis, J. L., Agüeros, M. A., Douglas, S. T., & Meibom, S. (2019). A Temporary Epoch of Stalled Spin-down for Low-mass Stars: Insights from NGC 6811 with Gaia and Kepler., *879*(1), Article 49, 49. https://doi.org/10.3847/1538-4357/ab2393

Davenport, J. R. A., Covey, K. R., Clarke, R. W., Boeck, A. C., Cornet, J., & Hawley, S. L. (2019). The Evolution of Flare Activity with Stellar Age., *871*(2), Article 241, 241. https://doi.org/10.3847/1538-4357/aafb76

Douglas, S. T., Agüeros, M. A., Covey, K. R., Bowsher, E. C., Bochanski, J. J., Cargile, P. A., Kraus, A., Law, N. M., Lemonias, J. J., Arce, H. G., Fierroz, D. F., & Kundert, A. (2014). The Factory and the Beehive. II. Activity and Rotation in Praesepe and the Hyades., *795*(2), Article 161, 161. https://doi.org/10.1088/0004-637X/795/2/161

Drake, J. J., & Stelzer, B. (2023). Stellar Coronae. In *Handbook of x-ray and gamma-ray astrophysics. edited by cosimo bambi and andrea santangelo* (p. 132). https://doi.org/10.1007/978-981-16-4544-0_78-1

Duvall, J., T. L., Dziembowski, W. A., Goode, P. R., Gough, D. O., Harvey, J. W., & Leibacher, J. W. (1984). Internal rotation of the Sun., *310*(5972), 22–25. https://doi.org/10.1038/310022a0

El-Badry, K., & Rix, H.-W. (2018). Imprints of white dwarf recoil in the separation distribution of Gaia wide binaries. *Monthly Notices of the Royal Astronomical Society*, *480*(4), 4884–4902. https://doi.org/10.1093/mnras/sty2186

Foster, G., Poppenhaeger, K., Ilic, N., & Schwope, A. (2022). Exoplanet X-ray irradiation and evaporation rates with eROSITA., *661*, Article A23, A23. https://doi.org/10.1051/0004-6361/202141097

Freund, S., Robrade, J., Schneider, P. C., & Schmitt, J. H. M. M. (2020). Updated X-ray view of the Hyades cluster., *640*, Article A66, A66. https://doi.org/10.1051/0004-6361/201937304

Fruscione, A., McDowell, J. C., Allen, G. E., Brickhouse, N. S., Burke, D. J., Davis, J. E., Durham, N., Elvis, M., Galle, E. C., Harris, D. E., Huenemoerder, D. P., Houck, J. C., Ishibashi, B., Karovska, M., Nicastro, F., Noble, M. S., Nowak, M. A., Primini, F. A., Siemiginowska, A., … Wise, M. (2006, June). CIAO: Chandra's data analysis system. In D. R. Silva & R. E. Doxsey (Eds.), *Society of photo-optical instrumentation engineers (spie) conference series* (p. 62701V, Vol. 6270). https://doi.org/10.1117/12.671760

Gaia Collaboration, Brown, A. G. A., Vallenari, A., Prusti, T., de Bruijne, J. H. J., Babusiaux, C., Bailer-Jones, C. A. L., Biermann, M., Evans, D. W., Eyer, L., Jansen, F., Jordi, C., Klioner, S. A., Lammers, U., Lindegren, L., Luri, X., Mignard, F., Panem, C., Pourbaix, D., … Zwitter, T. (2018). Gaia Data Release 2. Summary of the contents and survey properties., *616*, Article A1, A1. https://doi.org/10.1051/0004-6361/201833051

Gaia Collaboration, Prusti, T., de Bruijne, J. H. J., Brown, A. G. A., Vallenari, A., Babusiaux, C., Bailer-Jones, C. A. L., Bastian, U., Biermann, M., Evans, D. W., Eyer, L., Jansen, F., Jordi, C., Klioner, S. A., Lammers, U., Lindegren, L., Luri, X., Mignard, F., Milligan, D. J., … Zschocke, S. (2016). The Gaia mission., *595*, Article A1, A1. https://doi.org/10.1051/0004-6361/201629272

Gilman, P. A. (1983). Dynamically consistent nonlinear dynamos driven by convection in a rotating spherical shell. II - Dynamos with cycles and strong feedbacks., *53*, 243–268. https://doi.org/10.1086/190891

Gondoin, P., Aschenbach, B. R., Beijersbergen, M. W., Egger, R., Jansen, F. A., Stockman, Y., & Tock, J.-P. (1998, November). Calibration of the first XMM flight mirror module: I. Image quality. In R. B. Hoover & A. B. Walker (Eds.), *X-ray optics, instruments, and missions* (pp. 278–289, Vol. 3444). https://doi.org/10.1117/12.331243

Gruner, D., Barnes, S. A., & Janes, K. A. (2023). Wide binaries demonstrate the consistency of rotational evolution between open cluster and field stars., *675*, Article A180, A180. https://doi.org/10.1051/0004-6361/202346590

Grunhut, J. H., Wade, G. A., Neiner, C., Oksala, M. E., Petit, V., Alecian, E., Bohlender, D. A., Bouret, J. .-., Henrichs, H. F., Hussain, G. A. J., Kochukhov, O., & MiMeS Collaboration. (2017). The MiMeS survey of Magnetism in Massive Stars: magnetic analysis of the O-type stars., *465*(2), 2432–2470. https://doi.org/10.1093/mnras/stw2743

Guarcello, M. G., Micela, G., Peres, G., Prisinzano, L., & Sciortino, S. (2010). Chronology of star formation and disk evolution in the Eagle Nebula., *521*, Article A61, A61. https://doi.org/10.1051/0004-6361/201014351

Güdel, M. (2004). X-ray astronomy of stellar coronae., *12*(2-3), 71–237. https://doi.org/10.1007/s00159-004-0023-2

Guenther, E. W., Hartmann, M., Esposito, M., Hatzes, A. P., Cusano, F., & Gandolfi, D. (2009). A substellar component orbiting the F-star 30 Arietis B., *507*(3), 1659–1665. https://doi.org/10.1051/0004-6361/200912112

Hartigan, P., & Kenyon, S. J. (2003). A Spectroscopic Survey of Subarcsecond Binaries in the Taurus-Auriga Dark Cloud with the Hubble Space Telescope., *583*(1), 334–357. https://doi.org/10.1086/345293

Hosey, A. D., Henry, T. J., Jao, W.-C., Dieterich, S. B., Winters, J. G., Lurie, J. C., Riedel, A. R., & Subasavage, J. P. (2015). The Solar Neighborhood. XXXVI. The Long-term Photometric Variability of Nearby Red Dwarfs in the VRI Optical Bands., *150*(1), Article 6, 6. https://doi.org/10.1088/0004-6256/150/1/6

Howe, R., Christensen-Dalsgaard, J., Hill, F., Komm, R. W., Larsen, R. M., Schou, J., Thompson, M. J., & Toomre, J. (2000). Dynamic Variations at the Base of the Solar Convection Zone. *Science*, *287*(5462), 2456–2460. https://doi.org/10.1126/science.287.5462.2456

Hubrig, S., Järvinen, S. P., Ilyin, I., Schöller, M., & Jayaraman, R. (2023). Are magnetic fields universal in O-type multiple systems?, *521*(4), 6228–6246. https://doi.org/10.1093/mnras/stad730

Ilic, N., Poppenhaeger, K., & Hosseini, S. M. (2022). Tidal star-planet interaction and its observed impact on stellar activity in planet-hosting wide binary systems., *513*(3), 4380–4404. https://doi.org/10.1093/mnras/stac861

Ilić, N., Poppenhaeger, K., Dsouza, D., Wolk, S. J., Agüeros, M. A., & Stelzer, B. (2023). The first evidence of tidally induced activity in a brown dwarf-M dwarf pair: a Chandra study of the NLTT 41135/41136 system., *524*(4), 5954–5970. https://doi.org/10.1093/mnras/stad2277

Jansen, F., Lumb, D., Altieri, B., Clavel, J., Ehle, M., Erd, C., Gabriel, C., Guainazzi, M., Gondoin, P., Much, R., Munoz, R., Santos, M., Schartel, N., Texier, D., & Vacanti, G. (2001). XMM-Newton observatory. I. The spacecraft and operations., *365*, L1–L6. https://doi.org/10.1051/0004-6361:20000036

Jardine, M., & Unruh, Y. C. (1999). Coronal emission and dynamo saturation., *346*, 883–891.

Jeffries, R. D., Jackson, R. J., Briggs, K. R., Evans, P. A., & Pye, J. P. (2011). Investigating coronal saturation and supersaturation in fast-rotating M-dwarf stars., *411*(3), 2099–2112. https://doi.org/10.1111/j.1365-2966.2010.17848.x

Johnstone, C. P., & Güdel, M. (2015). The coronal temperatures of low-mass main-sequence stars., *578*, Article A129, A129. https://doi.org/10.1051/0004-6361/201425283

Joye, W. A., & Mandel, E. (2003, January). New Features of SAOImage DS9. In H. E. Payne, R. I. Jedrzejewski, & R. N. Hook (Eds.), *Astronomical data analysis software and systems xii* (p. 489, Vol. 295).

Kawaler, S. D. (1988). Angular Momentum Loss in Low-Mass Stars., *333*, 236. https://doi.org/10.1086/166740

Khalafinejad, S., Molaverdikhani, K., Blecic, J., Mallonn, M., Nortmann, L., Caballero, J. A., Rahmati, H., Kaminski, A., Sadegi, S., Nagel, E., Carone, L., Amado, P. J., Azzaro, M., Bauer, F. F., Casasayas-Barris, N., Czesla, S., von Essen, C., Fossati, L., Güdel, M., … Zechmeister, M. (2021). Probing the atmosphere of WASP-69 b with low- and high-resolution transmission spectroscopy., *656*, Article A142, A142. https://doi.org/10.1051/0004-6361/202141191

Kippenhahn, R., Weigert, A., & Weiss, A. (2013). *Stellar Structure and Evolution*. https://doi.org/10.1007/978-3-642-30304-3

Kraft, R. P., Burrows, D. N., & Nousek, J. A. (1991). Determination of Confidence Limits for Experiments with Low Numbers of Counts., *374*, 344. https://doi.org/10.1086/170124

Kraft, R. P. (1967). Studies of Stellar Rotation. V. The Dependence of Rotation on Age among Solar-Type Stars., *150*, 551. https://doi.org/10.1086/149359

Liefke, C., Ness, J. .-., Schmitt, J. H. M. M., & Maggio, A. (2008). Coronal properties of the EQ Pegasi binary system., *491*(3), 859–872. https://doi.org/10.1051/0004-6361:200810054

Liefke, C., & Schmitt, J. H. M. M. (2005, March). The NEXXUS database - X-ray properties of nearby stars. In F. Favata, G. A. J. Hussain, & B. Battrick (Eds.), *13th cambridge workshop on cool stars, stellar systems and the sun* (p. 755, Vol. 560).

Luque, R., & Pallé, E. (2022). Density, not radius, separates rocky and water-rich small planets orbiting M dwarf stars. *Science*, *377*(6611), 1211–1214. https://doi.org/10.1126/science.abl7164

Magaudda, E., Stelzer, B., Covey, K. R., Raetz, S., Matt, S. P., & Scholz, A. (2020). Relation of X-ray activity and rotation in M dwarfs and predicted time-evolution of the X-ray luminosity., *638*, Article A20, A20. https://doi.org/10.1051/0004-6361/201937408

Magaudda, E., Stelzer, B., & Raetz, S. (2022). First eROSITA-TESS results for M dwarfs: Mass dependence of the X-ray activity rotation relation and an assessment of sensitivity limits. *Astronomische Nachrichten*, *343*(8), Article e20220049, e20220049. https://doi.org/10.1002/asna.20220049

Mamajek, E. E., & Hillenbrand, L. A. (2008). Improved Age Estimation for Solar-Type Dwarfs Using Activity-Rotation Diagnostics., *687*(2), 1264–1293. https://doi.org/10.1086/591785

Matt, S. P., Brun, A. S., Baraffe, I., Bouvier, J., & Chabrier, G. (2015). The Mass-dependence of Angular Momentum Evolution in Sun-like Stars., *799*(2), Article L23, L23. https://doi.org/10.1088/2041-8205/799/2/L23

Newton, E. R., Irwin, J., Charbonneau, D., Berlind, P., Calkins, M. L., & Mink, J. (2017). The Hα Emission of Nearby M Dwarfs and its Relation to Stellar Rotation., *834*(1), Article 85, 85. https://doi.org/10.3847/1538-4357/834/1/85

Núñez, A., Agüeros, M. A., Covey, K. R., Douglas, S. T., Drake, J. J., Rampalli, R., Bowsher, E. C., Cargile, P. A., Kraus, A. L., & Law, N. M. (2022). The Factory and the Beehive. IV. A Comprehensive Study of the Rotation X-Ray Activity Relation in Praesepe and the Hyades., *931*(1), Article 45, 45. https://doi.org/10.3847/1538-4357/ac6517

Orlando, S., Peres, G., & Reale, F. (2001). The Sun as an X-Ray Star. IV. The Contribution of Different Regions of the Corona to Its X-Ray Spectrum., *560*(1), 499–513. https://doi.org/10.1086/322333

Pecaut, M. J., & Mamajek, E. E. (2013). Intrinsic Colors, Temperatures, and Bolometric Corrections of Pre-main-sequence Stars., *208*(1), Article 9, 9. https://doi.org/10.1088/0067-0049/208/1/9

Perger, M., Scandariato, G., Ribas, I., Morales, J. C., Affer, L., Azzaro, M., Amado, P. J., Anglada-Escudé, G., Baroch, D., Barrado, D., Bauer, F. F., Béjar, V. J. S., Caballero, J. A., Cortés-Contreras, M., Damasso, M., Dreizler, S., González-Cuesta, L., González Hernández, J. I., Guenther, E. W., … Zechmeister, M. (2019). Gliese 49: activity evolution and detection of a super-Earth. A HADES and CARMENES collaboration., *624*, Article A123, A123. https://doi.org/10.1051/0004-6361/201935192

Pinamonti, M., Damasso, M., Marzari, F., Sozzetti, A., Desidera, S., Maldonado, J., Scandariato, G., Affer, L., Lanza, A. F., Bignamini, A., Bonomo, A. S., Borsa, F., Claudi, R., Cosentino, R., Giacobbe, P., González-Álvarez, E., González Hernández, J. I., Gratton, R., Leto, G., … Toledo-Padrón, B. (2018). The HADES RV Programme with HARPS-N at TNG. VIII. GJ15A: a multiple wide planetary system sculpted by binary interaction., *617*, Article A104, A104. https://doi.org/10.1051/0004-6361/201732535

Poppenhaeger, K., & Wolk, S. J. (2014). Indications for an influence of hot Jupiters on the rotation and activity of their host stars., *565*, Article L1, L1. https://doi.org/10.1051/0004-6361/201423454

Poppenhaeger, K. (2022). Extrasolar Planets and Star-Planet Interaction. In *Handbook of x-ray and gamma-ray astrophysics. edited by cosimo bambi and andrea santangelo* (p. 26). https://doi.org/10.1007/978-981-16-4544-0_84-1

Rosen, L., Kochukhov, O., & Wade, G. A. (2013). Strong variable linear polarization in the cool active star II Peg., *436*, L10–L14. https://doi.org/10.1093/mnrasl/slt102

Rosen, L., Kochukhov, O., & Wade, G. A. (2015). Zeeman Doppler Imaging of a Cool Star Using Line Profiles in All Four Stokes Parameters for the First Time. *18th Cambridge Workshop on Cool Stars, Stellar Systems, and the Sun*, *18*, 913–918. https://doi.org/10.48550/arXiv.1408.4035

Rosen, S. R., Webb, N. A., Watson, M. G., Ballet, J., Barret, D., Braito, V., Carrera, F. J., Ceballos, M. T., Coriat, M., Della Ceca, R., Denkinson, G., Esquej, P., Farrell, S. A., Freyberg, M., Grisé, F., Guillout, P., Heil, L., Koliopanos, F., Law-Green, D., … Zolotukhin, I. (2016). The XMM-Newton serendipitous survey. VII. The third XMM-Newton serendipitous source catalogue., *590*, Article A1, A1. https://doi.org/10.1051/0004-6361/201526416

Sanz-Forcada, J., Micela, G., Ribas, I., Pollock, A. M. T., Eiroa, C., Velasco, A., Solano, E., & García-Álvarez, D. (2011). Estimation of the XUV radiation onto close planets and their evaporation., *532*, Article A6, A6. https://doi.org/10.1051/0004-6361/201116594

Schatzman, E. (1962). A theory of the role of magnetic activity during star formation. *Annales d'Astrophysique*, *25*, 18.

Schmitt, J. H. M. M., & Liefke, C. (2004). NEXXUS: A comprehensive ROSAT survey of coronal X-ray emission among nearby solar-like stars., *417*, 651–665. https://doi.org/10.1051/0004-6361:20030495

Skumanich, A. (1972). Time Scales for Ca II Emission Decay, Rotational Braking, and Lithium Depletion., *171*, 565. https://doi.org/10.1086/151310

Smith, R. K., Brickhouse, N. S., Liedahl, D. A., & Raymond, J. C. (2001). Collisional Plasma Models with APEC/APED: Emission-Line Diagnostics of Hydrogen-like and Helium-like Ions., *556*(2), L91–L95. https://doi.org/10.1086/322992

Stelzer, B., Damasso, M., Scholz, A., & Matt, S. P. (2016). A path towards understanding the rotation-activity relation of M dwarfs with K2 mission, X-ray and UV data., *463*(2), 1844–1864. https://doi.org/10.1093/mnras/stw1936

Stix, M. (1976). Differential rotation and the solar dynamo., *47*(2), 243–254.

Strassmeier, K. G., Carroll, T. A., & Ilyin, I. V. (2023). Zeeman Doppler imaging of ξ Boo A and B., *674*, Article A118, A118. https://doi.org/10.1051/0004-6361/202245664

Vidotto, A. A., Gregory, S. G., Jardine, M., Donati, J. F., Petit, P., Morin, J., Folsom, C. P., Bouvier, J., Cameron, A. C., Hussain, G., Marsden, S., Waite, I. A., Fares, R., Jeffers, S., & do Nascimento,

J. D. (2014). Stellar magnetism: empirical trends with age and rotation., *441*(3), 2361–2374. https://doi.org/10.1093/mnras/stu728

Vilhu, O. (1984). The nature of magnetic activity in lower main sequence stars., *133*, 117–126.

Vilhu, O., & Walter, F. M. (1987). Chromospheric-Coronal Activity at Saturated Levels., *321*, 958. https://doi.org/10.1086/165689

Webb, N. A., Coriat, M., Traulsen, I., Ballet, J., Motch, C., Carrera, F. J., Koliopanos, F., Authier, J., de la Calle, I., Ceballos, M. T., Colomo, E., Chuard, D., Freyberg, M., Garcia, T., Kolehmainen, M., Lamer, G., Lin, D., Maggi, P., Michel, L., … Zakardjian, A. (2020). The XMM-Newton serendipitous survey. IX. The fourth XMM-Newton serendipitous source catalogue., *641*, Article A136, A136. https://doi.org/10.1051/0004-6361/201937353

Weisskopf, M. C., Tananbaum, H. D., Van Speybroeck, L. P., & O'Dell, S. L. (2000, July). Chandra X-ray Observatory (CXO): overview. In J. E. Truemper & B. Aschenbach (Eds.), *X-ray optics, instruments, and missions iii* (pp. 2–16, Vol. 4012). https://doi.org/10.1117/12.391545

Wilson, O. C. (1966). Stellar Convection Zones, Chromospheres, and Rotation., *144*, 695. https://doi.org/10.1086/148649

Wright, N. J., Drake, J. J., Mamajek, E. E., & Henry, G. W. (2011). The Stellar-activity-Rotation Relationship and the Evolution of Stellar Dynamos., *743*(1), Article 48, 48. https://doi.org/10.1088/0004-637X/743/1/48

Wright, N. J., Newton, E. R., Williams, P. K. G., Drake, J. J., & Yadav, R. K. (2018). The stellar rotation-activity relationship in fully convective M dwarfs., *479*(2), 2351–2360. https://doi.org/10.1093/mnras/sty1670

APPENDIX A

Acknowledgement

All of my achievements would not have been possible without the support of my parents. They had enough faith in their Mass Communication and journalism-trained son to be able to study Astrophysics! That speaks volumes about their support.

I would also like to express my gratitude to Dr. Nikoleta Ilić for her constant support and supervision during my work on this thesis. Without her constant support, this thesis may not have come to fruition. I am also grateful to Prof. Dr. Katja Poppenhäger for allowing me to work with her as a Master's student and for providing me with resources at the AIP. This opportunity helped me not only learn science by doing but also gave me an environment to connect with other astrophysicists in the group. Additionally, I would also like to thank both Prof. Dr. Poppenhäger and Dr. Ilić for inviting me to collaborate on the NLT 41135/36 paper. I would also like to thank my colleague Dr. Eliana Maritza Amazo-Gómez for the discussions and Joana Wokittel for her help in reviewing the thesis.

This thesis employs a list of Chandra datasets, obtained by the Chandra X-ray Observatory, contained in[Chandra Data Collection (CDC) 154](https://doi.org/10.25574/cdc.154). This work also has made use of data from the European Space Agency (ESA) mission *Gaia* (https://www.cosmos.esa.int/gaia), processed by the *Gaia* Data Processing and Analysis Consortium (DPAC, https://www.cosmos.esa.int/web/gaia/dpac/consortium). Funding for the DPAC has been provided by national institutions, in particular, the institutions participating in the *Gaia* Multilateral Agreement. This research has also made use of data obtained from the Chandra Data Archive and software provided by the CXC in the application packages CIAO and Sherpa. This research has also made use of data obtained from the 4XMM XMM-Newton serendipitous source catalogue compiled by the 10 institutes of the XMM-Newton Survey Science Centre selected by ESA.

The Chandra pipeline also made use of open-source Python packages like Numpy, Astropy , SciPy and Pandas.

APPENDIX B

Analysis caveats

Here we describe the observation IDs and the particular systems that were rejected.

4994 had stars that were observed on the edge of the CCD.

5547 had stars that were observed on the edge of the CCD

7541 had occulting extraction regions for HD317101A and HD317101B.

20167 had HD152751 observed on the edge of the ccd with some photons spilling outside due to extreme elongation. Meanwhile evolved coordinates for the other component 'Wolf 629' place it outside the CCD.

21188 did not have visually identifiable binaries. The evolved extraction regions overlapped making the binaries not resolvable even for the faint pipeline.

1880, 22344 and 22876 were observations conducted using the HRC-S using the LETG grating. There were 2 systems in all of these observations. G272 61B and G272 61A and the binary GAIA DR2 5140692368567897472 and GAIA DR2 5140692368567915136. The data analysis flagged the GAIA stars but not the G272 stars. We believe that because these binary stars had very high proper motion they were removed from the binary catalogue. Since these observations were specifically planned for the G272 stars, the spectrographs were aligned with them. We therefore decided to only process only G272 stars. Meanwhile, the GAIA pairs were off-axis of the spectrograph and not visually visible.

V* BX Tri A: The binary catalogue categorises V* BX Tri A and LSPM J0220+3319 as a binary. However, in Simbad V* BX Tri has been classified as a binary system consisting of components A and B. Therefore we believe that these are a triple system or an error in classification. We calculate the luminosity of V* BX Tri system as $138 \pm 1.9769 \times 10^{+27}$ erg/s and LSPM J0220 +3319 as $3.849 \times 10^{+27}$ erg/s. This gives us $|\Delta \log_{10} L_X| = 1.55$ which stands out of the limit we calculate in our study as < 1

APPENDIX C

Background subtraction vs direct signal

We plot these to check for significant background noise in our ccd as per the recommendation in ciao-4.14 user manual.

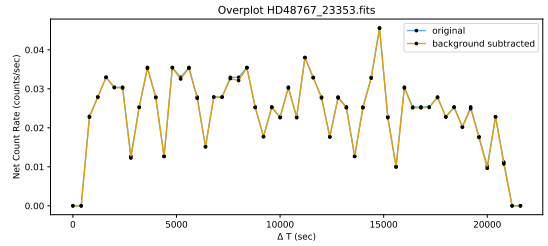

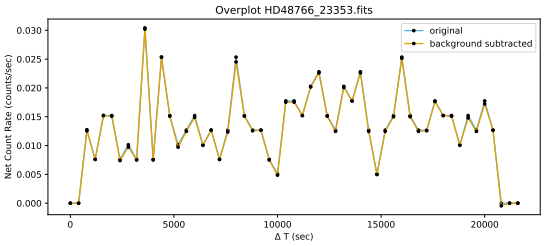

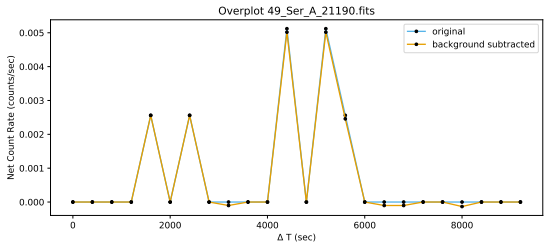

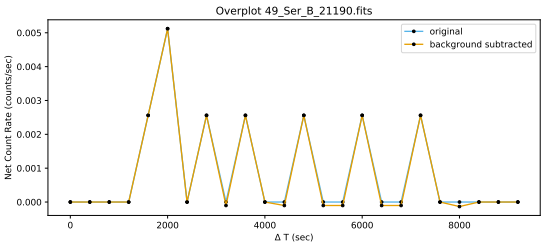

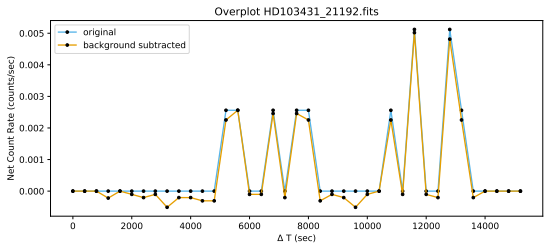

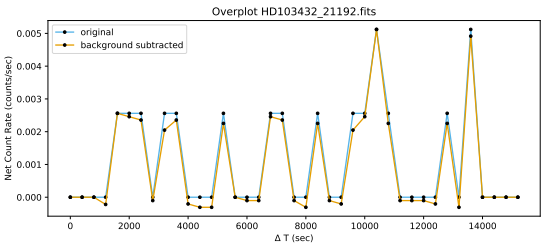

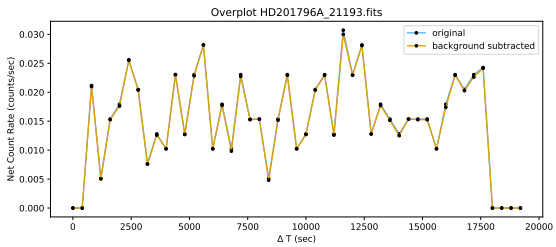

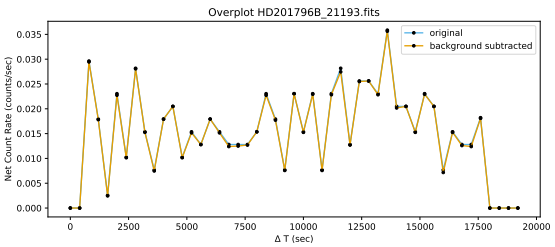

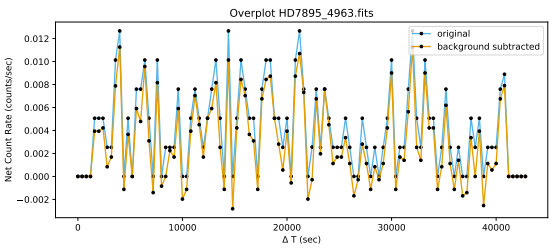

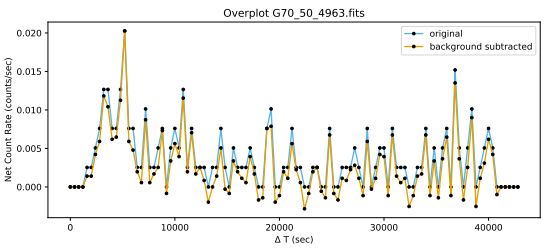

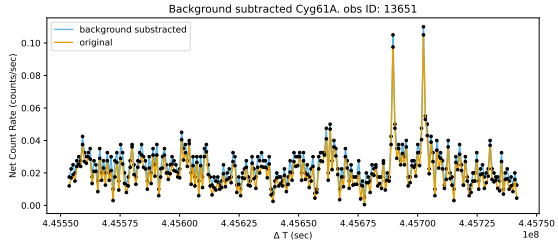
Background subtracted Cyg61A. obs ID: 13651
background substracted
original
Net Count Rate (counts/sec)
Δ T (sec)
1e8

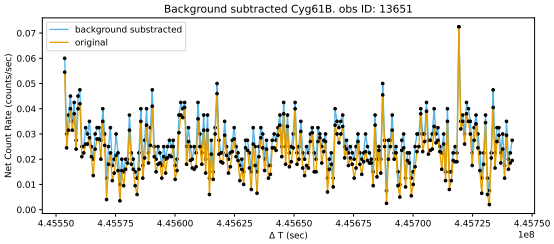
Background subtracted Cyg61B. obs ID: 13651
background substracted
original
Net Count Rate (counts/sec)
Δ T (sec)
1e8

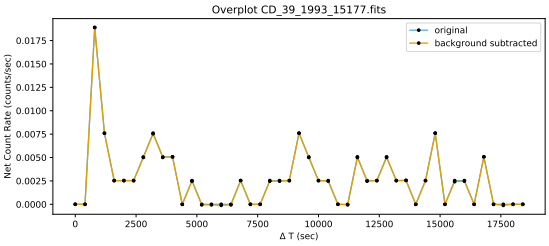
Overplot CD_39_1993_15177.fits
original
background subtracted
Net Count Rate (counts/sec)
Δ T (sec)

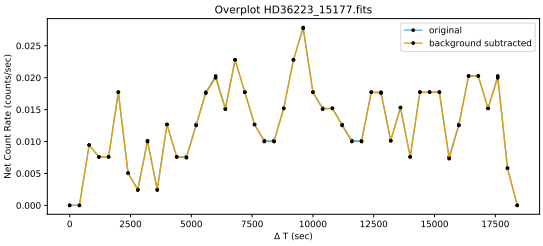
Overplot HD36223_15177.fits
original
background subtracted
Net Count Rate (counts/sec)
Δ T (sec)

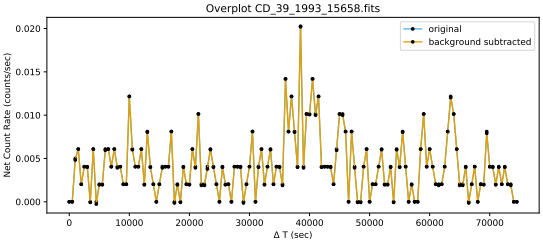
Overplot CD_39_1993_15658.fits
original
background subtracted
Net Count Rate (counts/sec)
Δ T (sec)

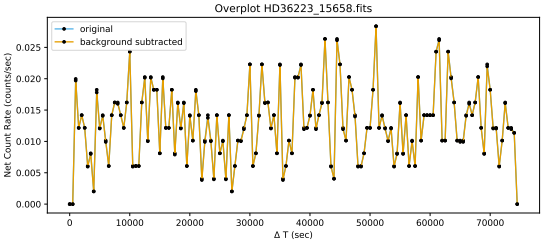
Overplot HD36223_15658.fits
original
background subtracted
Net Count Rate (counts/sec)
Δ T (sec)

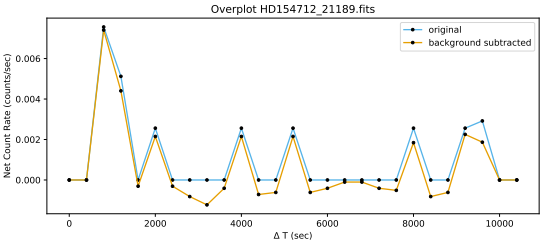
Overplot HD154712_21189.fits
original
background subtracted
Net Count Rate (counts/sec)
Δ T (sec)

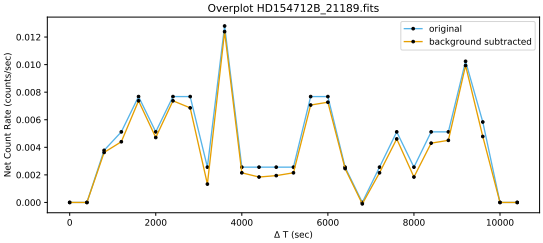
Overplot HD154712B_21189.fits
original
background subtracted
Net Count Rate (counts/sec)
Δ T (sec)

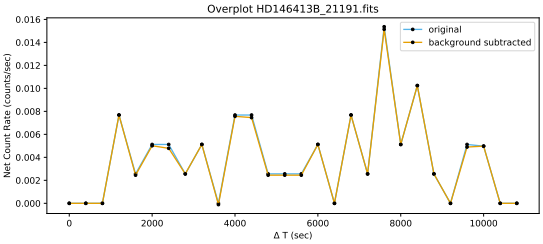
Overplot HD146413B_21191.fits
original
background subtracted
Net Count Rate (counts/sec)
Δ T (sec)

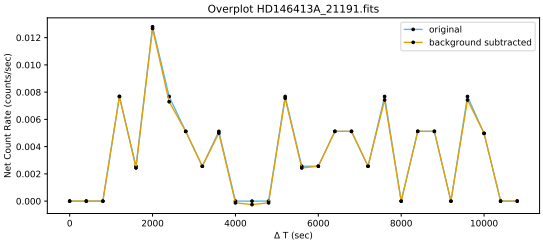
Overplot HD146413A_21191.fits
original
background subtracted
Net Count Rate (counts/sec)
Δ T (sec)

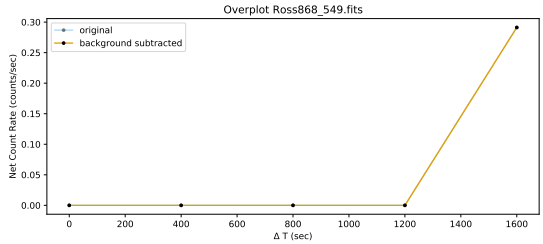
Overplot Ross868_549.fits
original
background subtracted
Net Count Rate (counts/sec)
Δ T (sec)

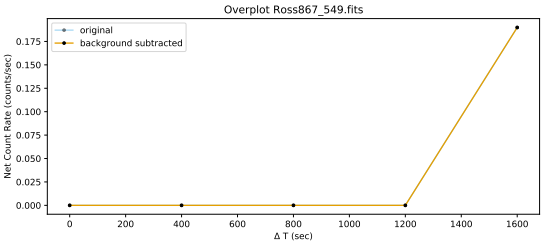
Overplot Ross867_549.fits
original
background subtracted
Net Count Rate (counts/sec)
Δ T (sec)

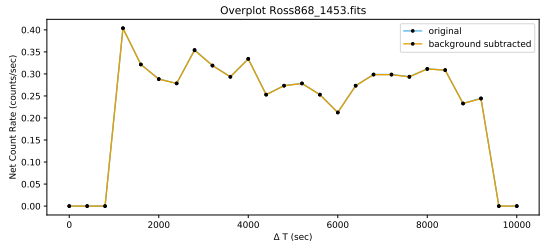
Overplot Ross868_1453.fits
original
background subtracted
Net Count Rate (counts/sec)
Δ T (sec)

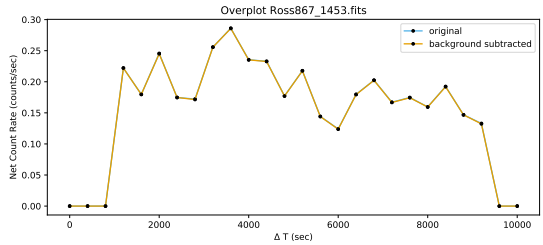
Overplot Ross867_1453.fits
original
background subtracted
Net Count Rate (counts/sec)
Δ T (sec)

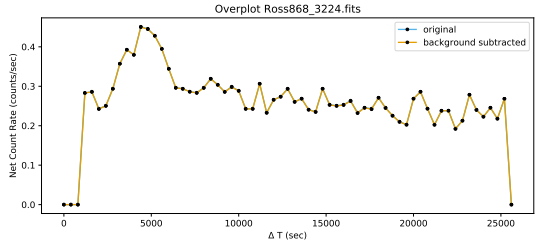
Overplot Ross868_3224.fits
original
background subtracted
Net Count Rate (counts/sec)
Δ T (sec)

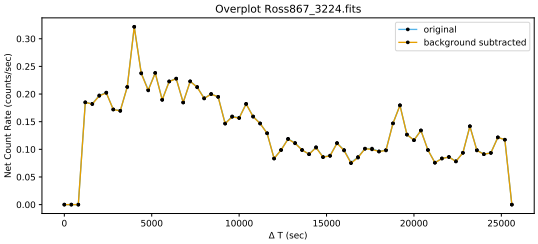
Overplot Ross867_3224.fits
original
background subtracted
Net Count Rate (counts/sec)
Δ T (sec)

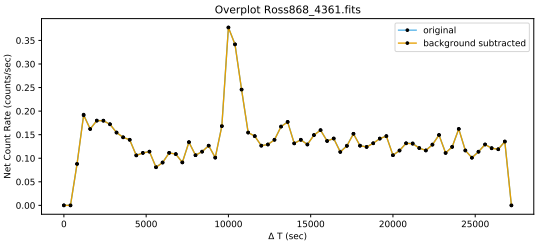
Overplot Ross868_4361.fits
original
background subtracted
Net Count Rate (counts/sec)
Δ T (sec)

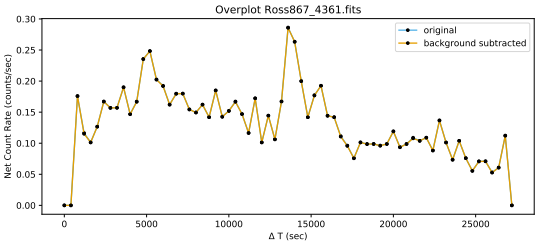
Overplot Ross867_4361.fits
original
background subtracted
Net Count Rate (counts/sec)
Δ T (sec)

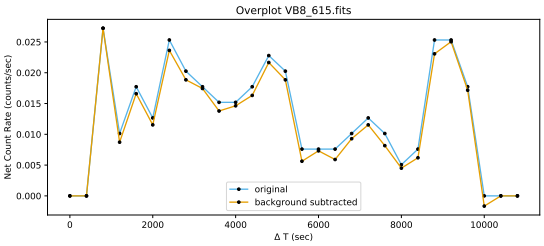
Overplot VB8_615.fits
original
background subtracted
Net Count Rate (counts/sec)
Δ T (sec)

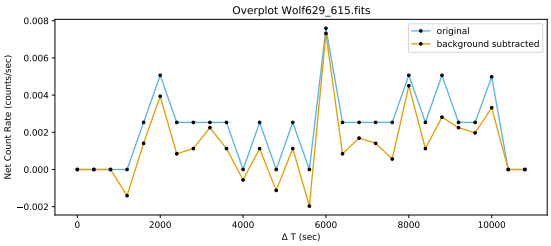
Overplot Wolf629_615.fits
original
background subtracted
Net Count Rate (counts/sec)
Δ T (sec)

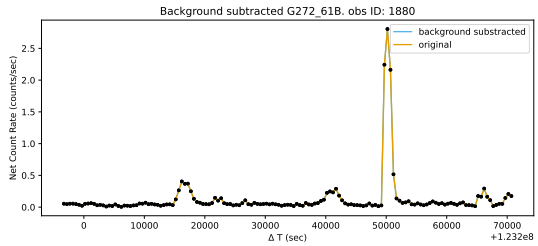
Background subtracted G272_61B. obs ID: 1880
background substracted
original
Net Count Rate (counts/sec)
Δ T (sec)
+1.232e8

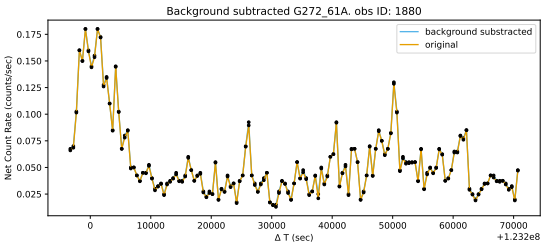
Background subtracted G272_61A. obs ID: 1880
background substracted
original
Net Count Rate (counts/sec)
Δ T (sec)
+1.232e8

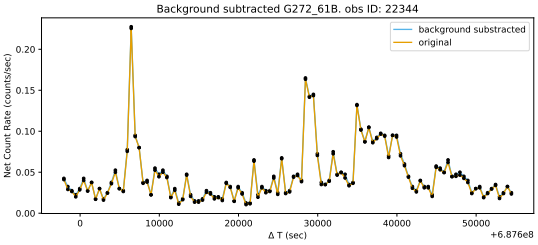
Background subtracted G272_61B. obs ID: 22344
background substracted
original
Net Count Rate (counts/sec)
Δ T (sec)
+6.876e8

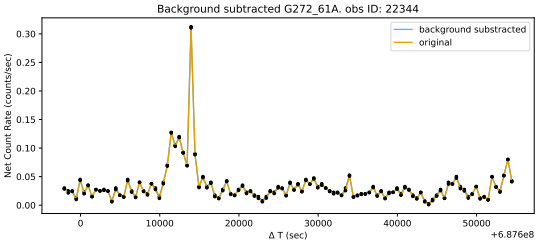
Background subtracted G272_61A. obs ID: 22344
background substracted
original
Net Count Rate (counts/sec)
Δ T (sec)
+6.876e8

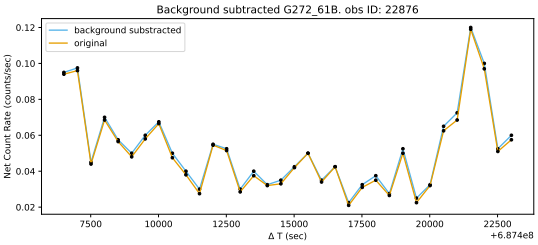
Background subtracted G272_61B. obs ID: 22876
background substracted
original
Net Count Rate (counts/sec)
Δ T (sec)
+6.874e8

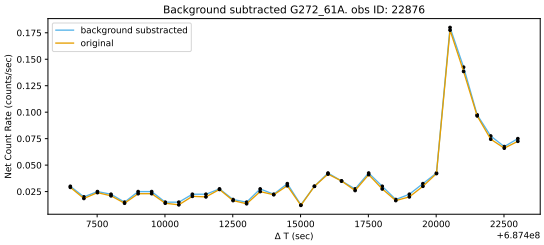
Background subtracted G272_61A. obs ID: 22876
background substracted
original
Net Count Rate (counts/sec)
Δ T (sec)
+6.874e8

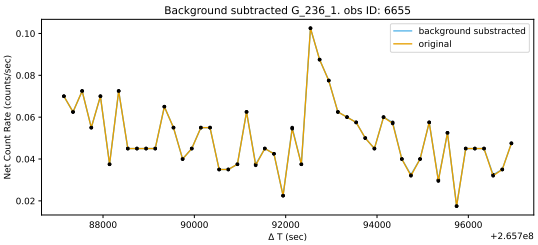
Background subtracted G_236_1. obs ID: 6655
background substracted
original
Net Count Rate (counts/sec)
Δ T (sec)
+2.657e8

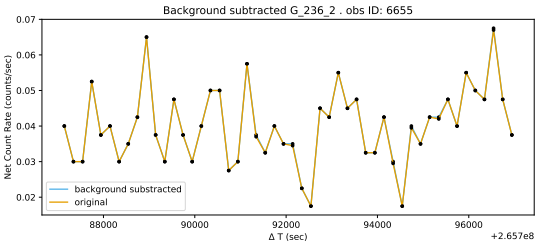
Background subtracted G_236_2 . obs ID: 6655
background substracted
original
Net Count Rate (counts/sec)
Δ T (sec)
+2.657e8

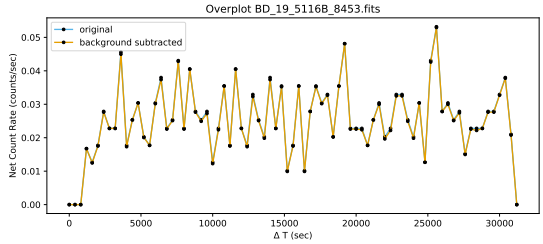
Overplot BD_19_5116B_8453.fits
original
background subtracted
Net Count Rate (counts/sec)
Δ T (sec)

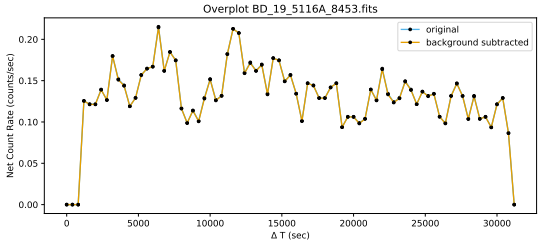
Overplot BD_19_5116A_8453.fits
original
background subtracted
Net Count Rate (counts/sec)
Δ T (sec)

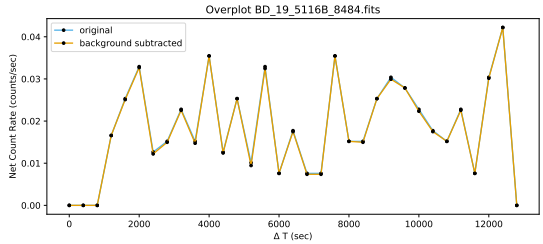
Overplot BD_19_5116B_8484.fits
original
background subtracted
Net Count Rate (counts/sec)
Δ T (sec)

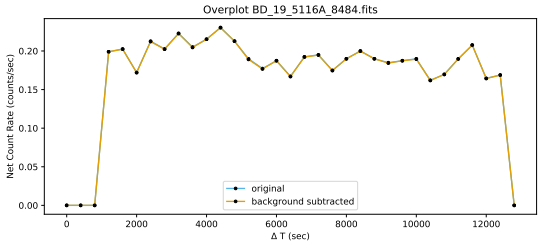
Overplot BD_19_5116A_8484.fits
original
background subtracted
Net Count Rate (counts/sec)
Δ T (sec)

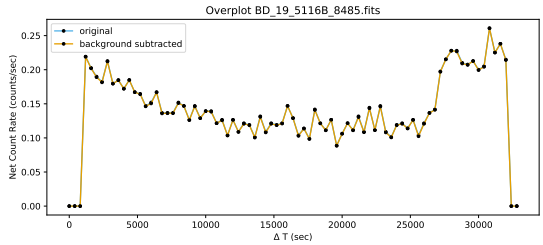
Overplot BD_19_5116B_8485.fits
original
background subtracted
Net Count Rate (counts/sec)
Δ T (sec)

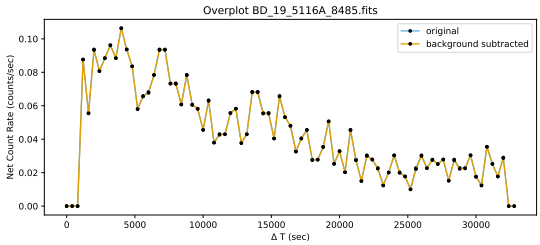
Overplot BD_19_5116A_8485.fits
original
background subtracted
Net Count Rate (counts/sec)
Δ T (sec)

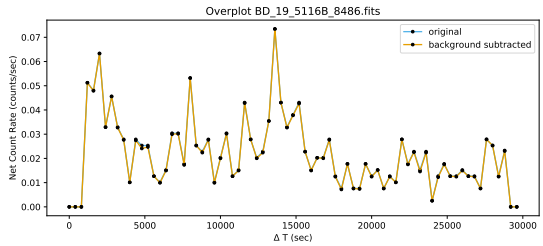
Overplot BD_19_5116B_8486.fits
original
background subtracted
Net Count Rate (counts/sec)
Δ T (sec)

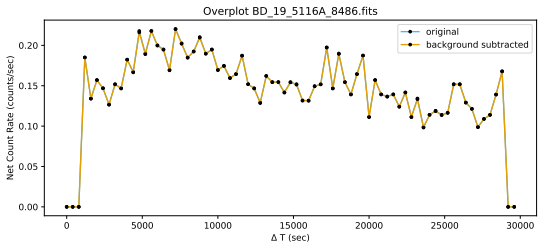
Overplot BD_19_5116A_8486.fits
original
background subtracted
Net Count Rate (counts/sec)
Δ T (sec)

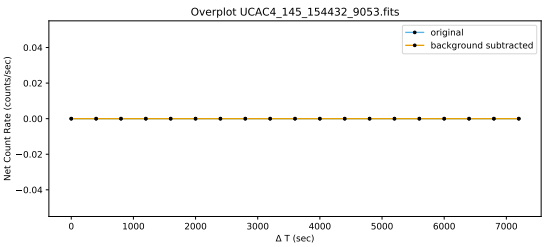
Overplot UCAC4_145_154432_9053.fits
original
background subtracted
Net Count Rate (counts/sec)
Δ T (sec)

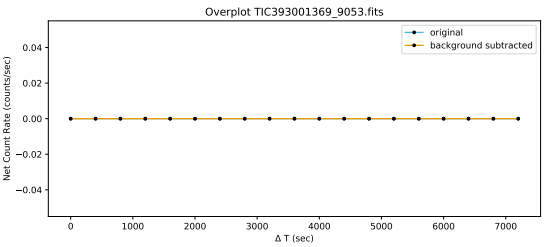
Overplot TIC393001369_9053.fits
original
background subtracted
Net Count Rate (counts/sec)
Δ T (sec)

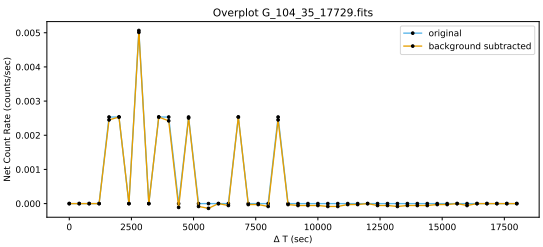
Overplot G_104_35_17729.fits
original
background subtracted
Net Count Rate (counts/sec)
Δ T (sec)

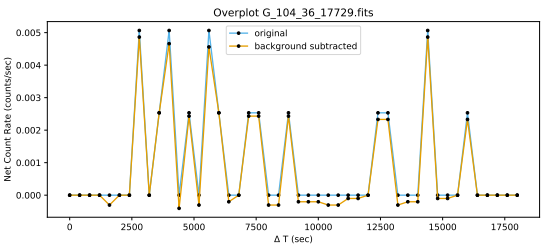
Overplot G_104_36_17729.fits
original
background subtracted
Net Count Rate (counts/sec)
Δ T (sec)

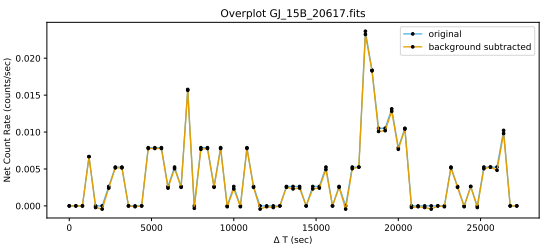
Overplot GJ_15B_20617.fits
original
background subtracted
Net Count Rate (counts/sec)
Δ T (sec)

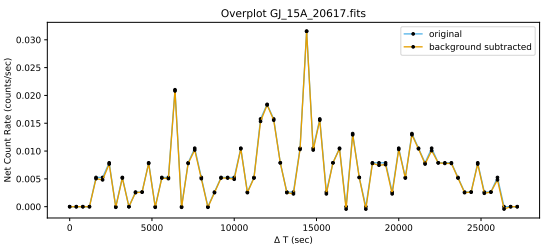
Overplot GJ_15A_20617.fits
original
background subtracted
Net Count Rate (counts/sec)
Δ T (sec)

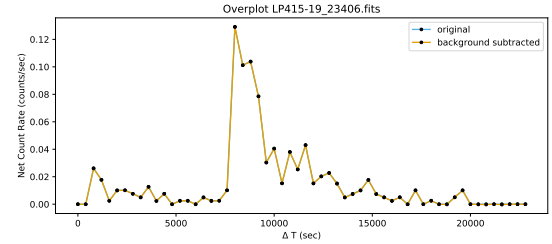
Overplot LP415-19_23406.fits
original
background subtracted
Net Count Rate (counts/sec)
Δ T (sec)

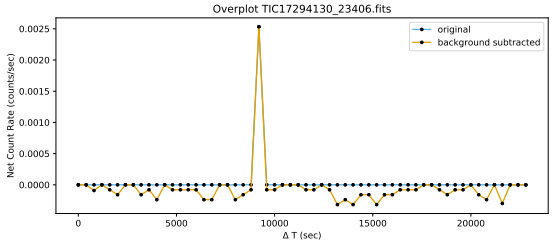
Overplot TIC17294130_23406.fits
original
background subtracted
Net Count Rate (counts/sec)
Δ T (sec)

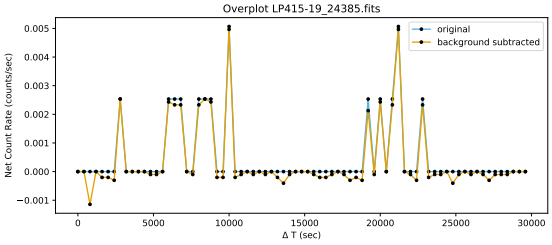
Overplot LP415-19_24385.fits
original
background subtracted
Net Count Rate (counts/sec)
Δ T (sec)

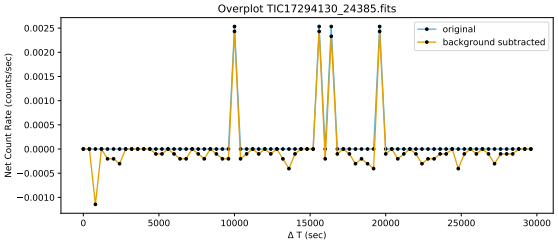
Overplot TIC17294130_24385.fits
original
background subtracted
Net Count Rate (counts/sec)
Δ T (sec)

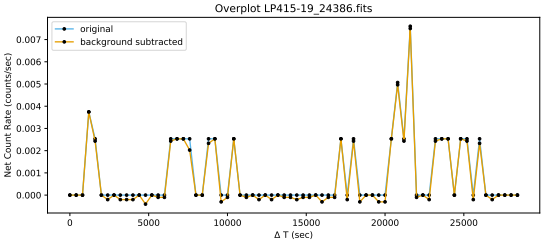
Overplot LP415-19_24386.fits
original
background subtracted
Net Count Rate (counts/sec)
Δ T (sec)

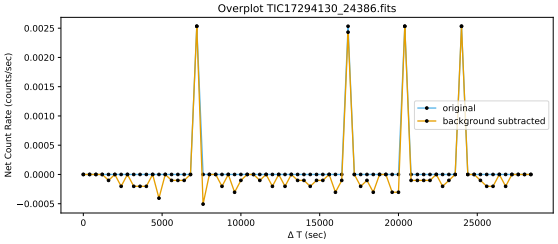
Overplot TIC17294130_24386.fits
original
background subtracted
Net Count Rate (counts/sec)
Δ T (sec)

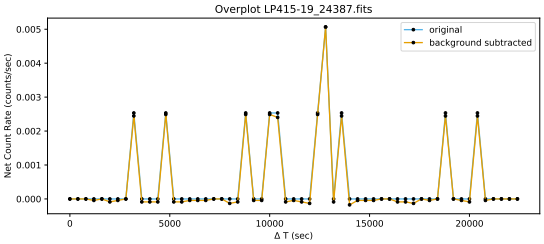
Overplot LP415-19_24387.fits
original
background subtracted
Net Count Rate (counts/sec)
Δ T (sec)

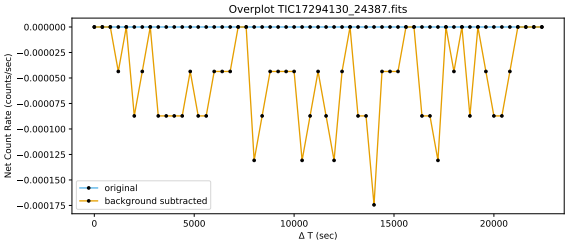
Overplot TIC17294130_24387.fits
original
background subtracted
Net Count Rate (counts/sec)
Δ T (sec)

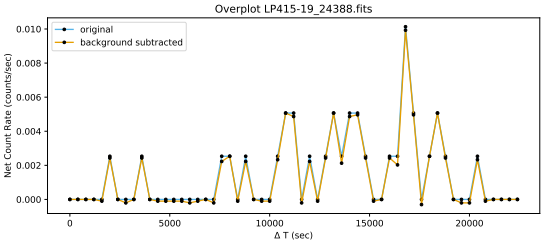
Overplot LP415-19_24388.fits
original
background subtracted
Net Count Rate (counts/sec)
Δ T (sec)

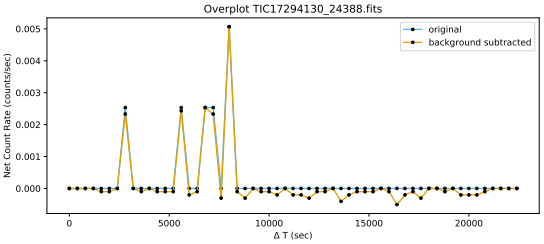
Overplot TIC17294130_24388.fits
original
background subtracted
Net Count Rate (counts/sec)
Δ T (sec)

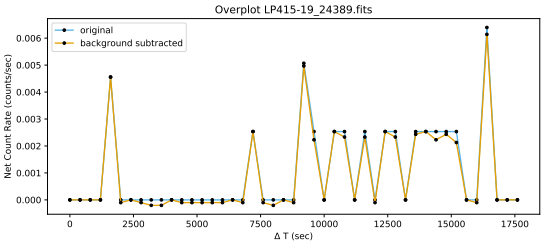
Overplot LP415-19_24389.fits
original
background subtracted
Net Count Rate (counts/sec)
Δ T (sec)

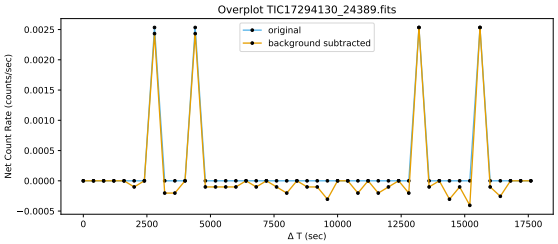
Overplot TIC17294130_24389.fits
original
background subtracted
Net Count Rate (counts/sec)
Δ T (sec)

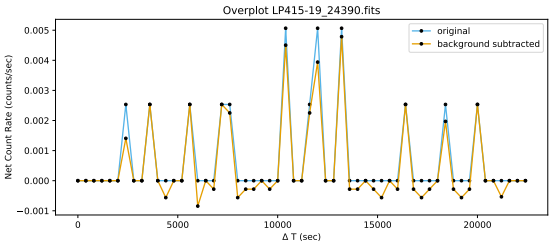
Overplot LP415-19_24390.fits
original
background subtracted
Net Count Rate (counts/sec)
Δ T (sec)

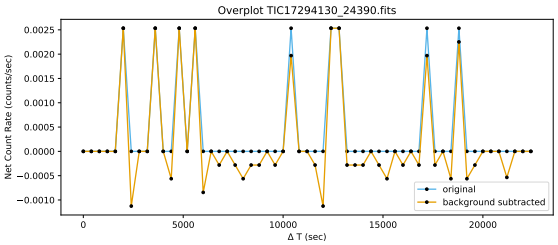
Overplot TIC17294130_24390.fits
original
background subtracted
Net Count Rate (counts/sec)
Δ T (sec)

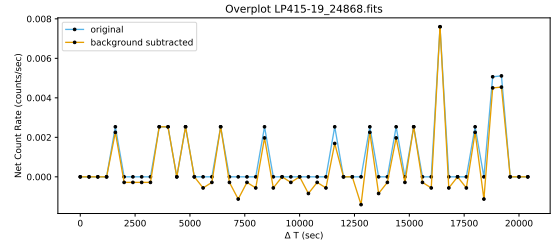
Overplot LP415-19_24868.fits
original
background subtracted
Net Count Rate (counts/sec)
Δ T (sec)

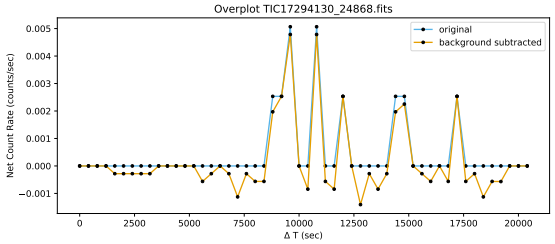
Overplot TIC17294130_24868.fits
original
background subtracted
Net Count Rate (counts/sec)
Δ T (sec)

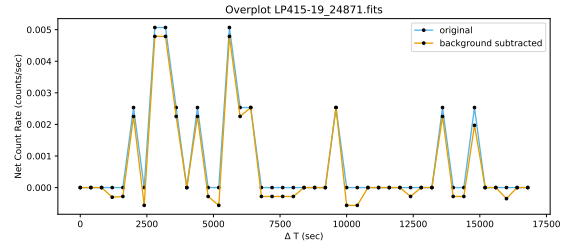
Overplot LP415-19_24871.fits
original
background subtracted
Net Count Rate (counts/sec)
Δ T (sec)

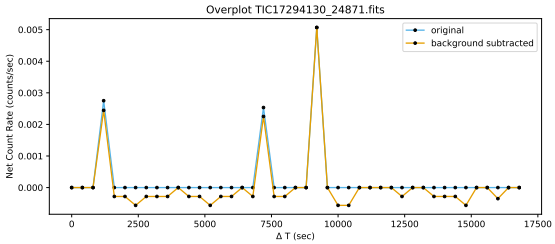
Overplot TIC17294130_24871.fits
original
background subtracted
Net Count Rate (counts/sec)
Δ T (sec)

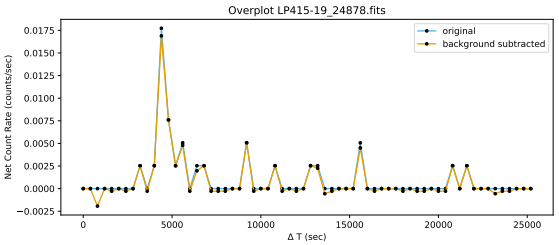
Overplot LP415-19_24878.fits
original
background subtracted
Net Count Rate (counts/sec)
Δ T (sec)

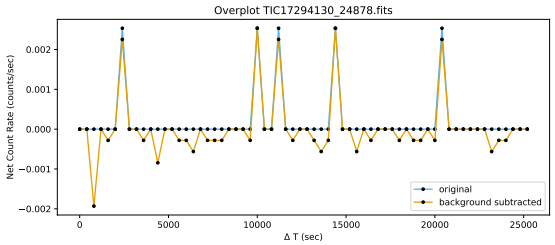
Overplot TIC17294130_24878.fits
original
background subtracted
Net Count Rate (counts/sec)
Δ T (sec)

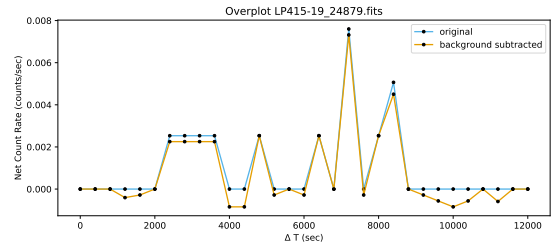
Overplot LP415-19_24879.fits
original
background subtracted
Net Count Rate (counts/sec)
Δ T (sec)

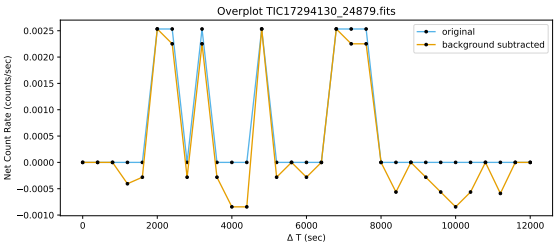
Overplot TIC17294130_24879.fits
original
background subtracted
Net Count Rate (counts/sec)
Δ T (sec)

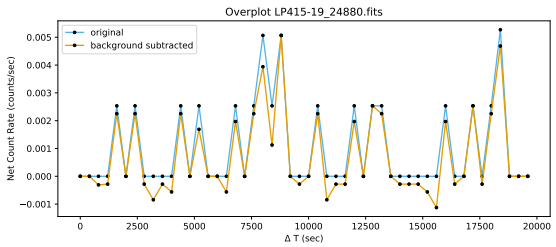
Overplot LP415-19_24880.fits
original
background subtracted
Net Count Rate (counts/sec)
Δ T (sec)

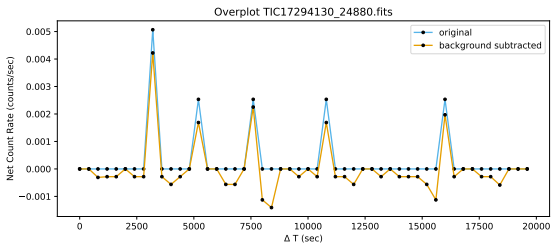
Overplot TIC17294130_24880.fits
original
background subtracted
Net Count Rate (counts/sec)
Δ T (sec)

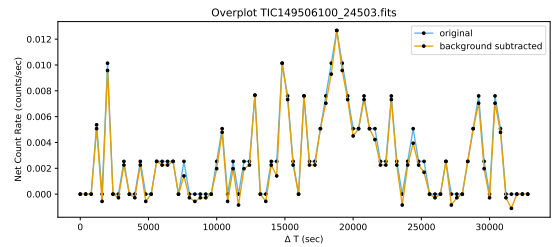
Overplot TIC149506100_24503.fits
original
background subtracted
Net Count Rate (counts/sec)
Δ T (sec)

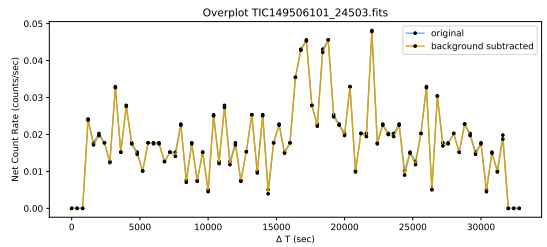
Overplot TIC149506101_24503.fits
original
background subtracted
Net Count Rate (counts/sec)
Δ T (sec)

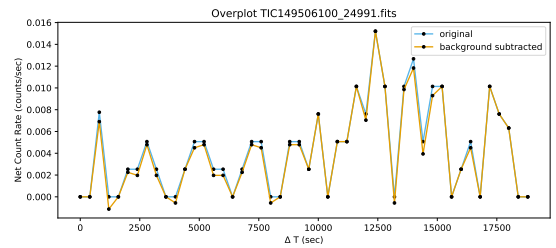
Overplot TIC149506100_24991.fits
original
background subtracted
Net Count Rate (counts/sec)
Δ T (sec)

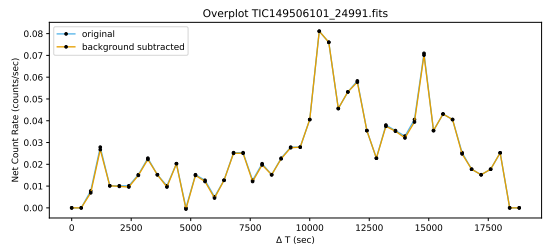
Overplot TIC149506101_24991.fits
original
background subtracted
Net Count Rate (counts/sec)
Δ T (sec)

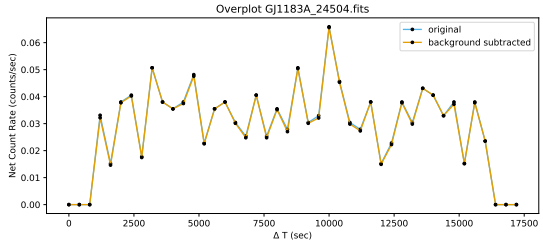
Overplot GJ1183A_24504.fits
original
background subtracted
Net Count Rate (counts/sec)
Δ T (sec)

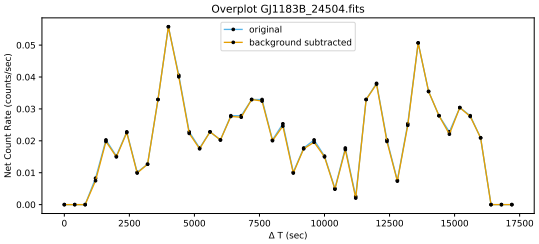
Overplot GJ1183B_24504.fits
original
background subtracted
Net Count Rate (counts/sec)
Δ T (sec)

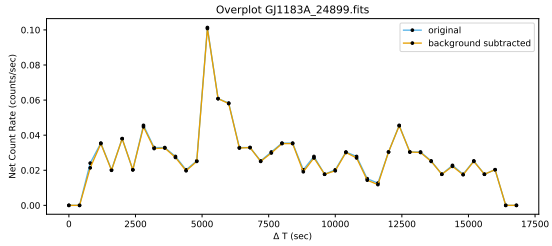
Overplot GJ1183A_24899.fits
original
background subtracted
Net Count Rate (counts/sec)
Δ T (sec)

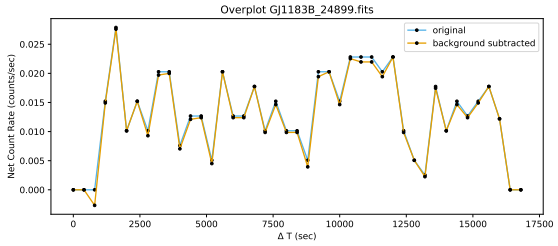
Overplot GJ1183B_24899.fits
original
background subtracted
Net Count Rate (counts/sec)
Δ T (sec)

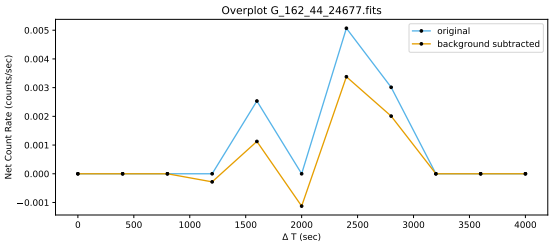
Overplot G_162_44_24677.fits
original
background subtracted
Net Count Rate (counts/sec)
Δ T (sec)

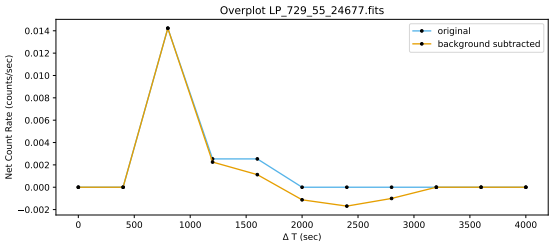
Overplot LP_729_55_24677.fits
original
background subtracted
Net Count Rate (counts/sec)
Δ T (sec)

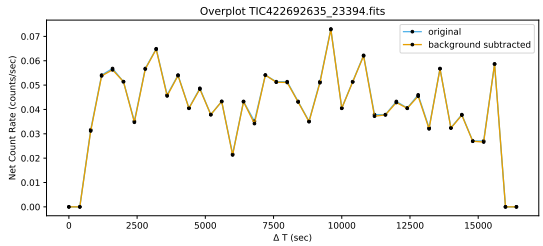
Overplot TIC422692635_23394.fits
original
background subtracted
Net Count Rate (counts/sec)
Δ T (sec)

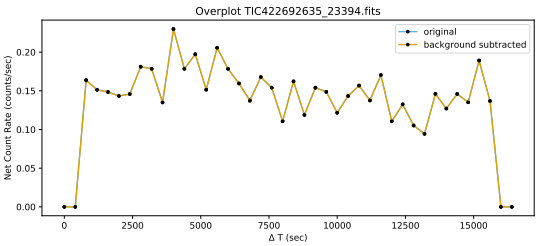
Overplot TIC422692635_23394.fits
original
background subtracted
Net Count Rate (counts/sec)
Δ T (sec)

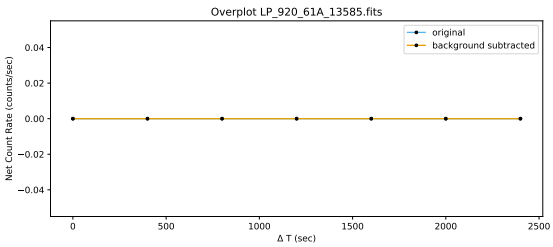
Overplot LP_920_61A_13585.fits
original
background subtracted
Net Count Rate (counts/sec)
Δ T (sec)

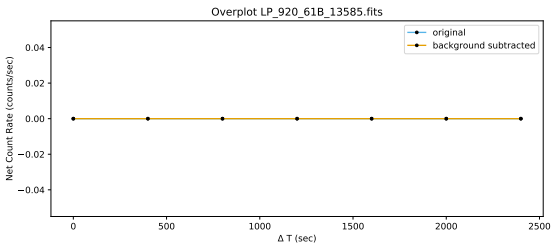
Overplot LP_920_61B_13585.fits
original
background subtracted
Net Count Rate (counts/sec)
Δ T (sec)

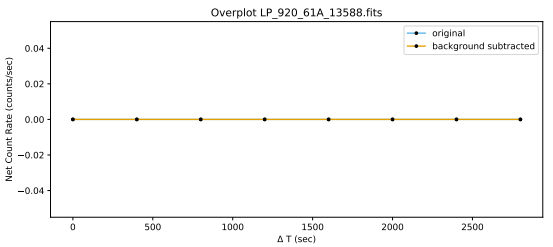
Overplot LP_920_61A_13588.fits
original
background subtracted
Net Count Rate (counts/sec)
Δ T (sec)

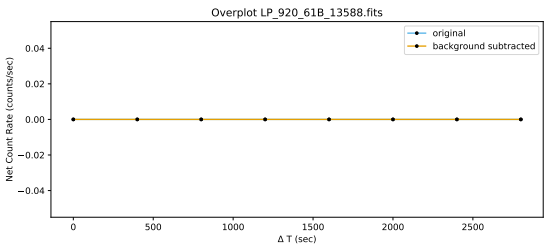
Overplot LP_920_61B_13588.fits
original
background subtracted
Net Count Rate (counts/sec)
Δ T (sec)

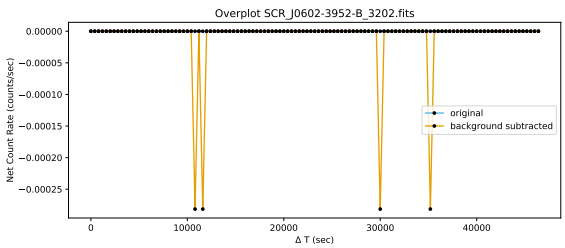
Overplot SCR_J0602-3952-B_3202.fits
original
background subtracted
Net Count Rate (counts/sec)
Δ T (sec)

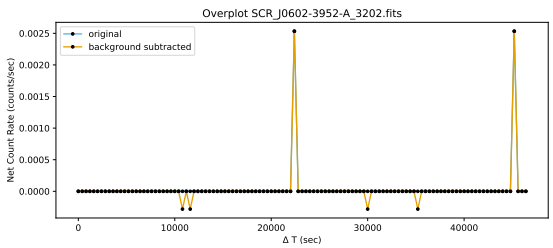
Overplot SCR_J0602-3952-A_3202.fits
original
background subtracted
Net Count Rate (counts/sec)
Δ T (sec)

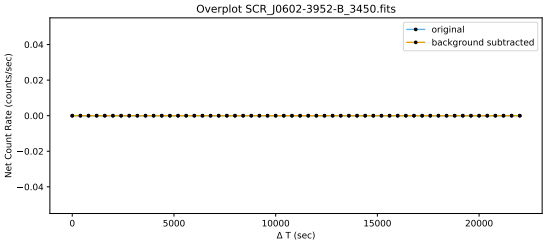
Overplot SCR_J0602-3952-B_3450.fits
original
background subtracted
Net Count Rate (counts/sec)
0.04
0.02
0.00
−0.02
−0.04
0
5000
10000
15000
20000
Δ T (sec)

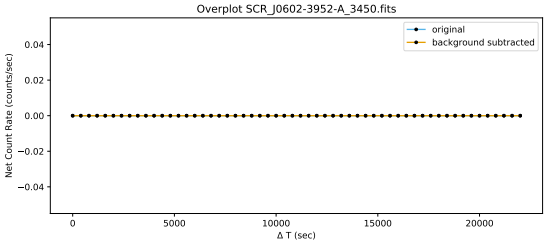
Overplot SCR_J0602-3952-A_3450.fits
original
background subtracted
Net Count Rate (counts/sec)
0.04
0.02
0.00
−0.02
−0.04
0
5000
10000
15000
20000
Δ T (sec)

APPENDIX D

Flare removal

These flares were removed from the counts as flares can skew the HR of the star to hotter temperatures.

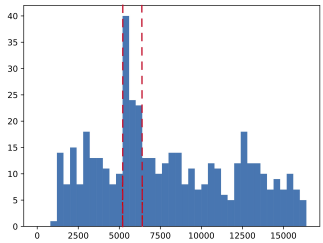

(a) GJ 1183A | obs ID: 24899

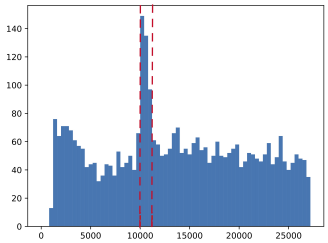

(b) Ross 868 | obs ID: 4361

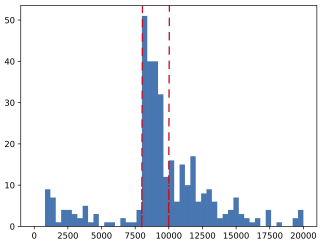

(c) LP 415-19 | obs ID: 23406

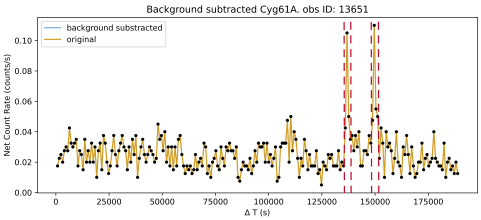

(a) Cyg 61 A | obs ID: 13651

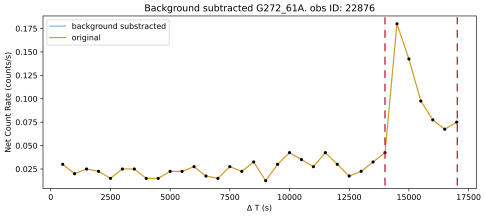

(b) G 272-61A | obs ID: 22876

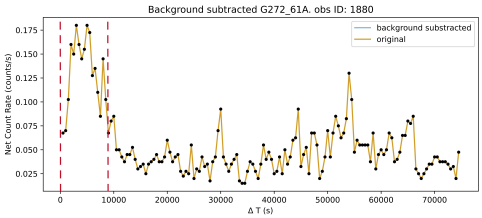

(a) G 272-61A | obs ID: 1880

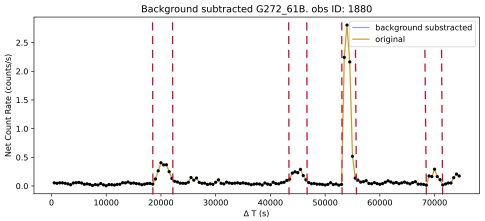

(b) G 272-61B | obs ID: 1880

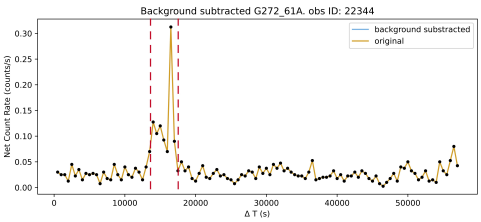

(a) G 272-61A | obs ID: 22344

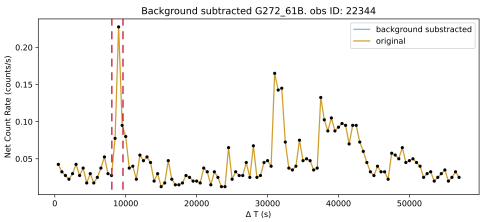

(b) G 272-61B | obs ID: 22344